

Using of Microencapsulated Phase Change Material Suspension to Enhance the Performance of Microchannel Heat Exchanger

Mushtaq I. Hasan Ahmad J. Shkarah Muhanned S. Ali Abdul Muhsin A. Rageb

Mech. Eng. Dept.

College of Engineering
Thi-Qar University

Mech. Eng. Dept.

College of Engineering
Thi-Qar University

Mech. Eng. Dept.

College of Engineering
Thi-Qar University

Mech. Eng. Dept.

College of Engineering
Basrah University

Abstract

The aim of this paper is to improve thermal performance of a counter flow microchannel heat exchanger (CFMCHE) by using microencapsulated phase change material slurry (MEPCM suspension) as a cooling fluid instead of pure fluid. The MEPCM suspension used in this paper consists of microcapsules constructed from n-octadecane as a phase change material (PCM) and the shell material is Polymethylmethacrylat, these capsules are suspended in water in a concentration of (0 – 20) %.

From the results, using of MEPCM suspensions as a cooling fluid leads to modify thermal performance of a CFMCHE by increasing its effectiveness but it also leads to increase the pressure drop. From heat transfer (thermal performance) point of view it is better to use this type of fluid to increase cooling efficiency of a CFMCHE, but due to extra increase in pressure drop it leads to reduce the overall performance compared with pure fluids. Therefore its application depends on the conditions at which this heat exchanger is used.

استخدام معلق المواد متغيرة الطور لتحسين أداء المبادل الحراري المايكروي

المستخلص

الهدف من هذا البحث هو لتحسين الأداء الحراري للمبادل الحراري المتعاكس المايكروي باستخدام معلق مكون من مواد متغيرة الطور كمائع تبريد بدلا من استخدام مائع نقي. المعلق المستخدم في هذا البحث مكون من مائع أساس هو الماء وكبسولات مايكروية مكونة من مادة n-octadecane كمادة متغيرة الطور وقشرة من مادة Polymethylmethacrylat. هذه الكبسولات مخلوطة بالماء بتركيز (0 – 20 %).

من النتائج التي تم الحصول عليها تبين أن استخدام معلق المواد متغيرة الطور كموائع تبريد يؤدي إلى تحسين الأداء الحراري للمبادل الحراري المتعاكس المايكروني من خلال زيادة فعاليته لكنه بنفس الوقت يؤدي إلى زيادة هبوط الضغط. من وجهة نظر الأداء الحراري فإنه يستحسن استخدام هذا النوع من الموائع لزيادة كفاءة التبريد لكن نتيجة للزيادة الكبيرة في هبوط الضغط فإنه يؤدي إلى تقليل الأداء الكلي للمبادل مقارنة مع الموائع النقية. لذلك فإن استخدام هذه الموائع يعتمد على الظروف التي يستخدم فيها هذا المبادل.

1. Introduction

Microchannel heat exchangers are of interest because they can remove large amount of heat over a small volume. This ability makes it well suited for highly specific applications that require compact high heat energy removal solutions such as, biomedical processes, metrology, telecommunications, cooling of high heat flux high density microelectronics, automotive industries, nuclear reactor barriers, fuel processing, aerospace and chemical industries.

Cooling fluids play an important role in all cooling applications, and its thermo physical properties considered as key parameters that affect its cooling abilities. All the observed literature used pure fluids (liquids and gases) as cooling fluids in a CFMCHE.

Using microencapsulated phase change material (MEPCM) suspensions has attracted more and more interest due to their capabilities of enhancing convective heat transfer and thermal storage performance. This heat transfer enhancement results from the latent heat absorption by the PCM in the suspended MEPCM particles during the melting process.

A phase change material PCM is a substance with a high latent heat of fusion which in melting and solidification is capable to absorb and release large amounts of heat. MEPCM offers an opportunity to reduce weight and volume in thermal management systems by utilizing the latent heat of the PCM. In this approach to thermal management, the large latent heat of PCM is coupled with the high heat transfer capabilities of microchannels to achieve a high thermal performance of CFMCHE.

Microchannel heat sink was first proposed by **Tuckerman and Pease (1981) [1]** for electronic cooling. They built a water cooled integral heat sink with microscopic flow channels, and demonstrated that extremely high power density with a heat flux as high as 790 W/cm^2 could be dissipated .

Following the work of Tuckerman and Pease, many researchers have been conducted for microchannels and microchannel heat sinks. **Klein et al (2005) [2]** studied experimentally the effects of surfactants solution on heat transfer of a single phase and boiling flows in

microchannel heat sinks. The surfactant used is Alkyl Poly Glycosides (APG). The results were compared with the heat transfer in water flow under similar conditions. For single phase flow, no significant difference was observed between heat transfer in water and surfactant solutions at various mass concentrations. For boiling flow of surfactant solutions, the optimal value of mass flux was found in which the heat transfer enhancement reached its maximum. The experiment has also revealed that at low mass fluxes, an optimal mass concentration of APG additives may be found for which a two phase flow heat transfer significantly increases. These findings lead to the conclusion that the use of surfactants should be considered as a method for improving two phase boiling flow heat transfer.

Yu et al (2006) [3] experimentally investigated the laminar flow characteristics of suspensions with microencapsulated phase change materials (MEPCM) in water flowing through rectangular cooper minichannels ($D_h < 3 \text{ mm}$) with the aim to develop methods for a more efficient cooling technology for high power electronics. The paper presented the first results of the experimental investigation on the laminar flow frictional characteristics of MEPCM- water suspension with various mass concentrations flowing in rectangular minichannels with ($D_h = 2.71 \text{ mm}$). The mass concentration of the suspension ranged from 0 - 20 %. The experiments were performed to explore the effect of MEPCM mass concentration on the friction factor and pressure drop in the minichannels. The Reynolds number range was from 200 to 2000. From the results, the laminar friction factor of the suspensions increased with increasing the MEPCM concentrations. Compared with the friction factor of water, a slight increase was found for low concentrations of 5 %. However, when the concentration was 10 % or higher, the increase in the friction factor becomes much more distinctive.

Yu et al (2007) [4] investigated experimentally the convective heat transfer characteristics of water based suspensions of (MEPCM) flowing through rectangular cooper minichannels ($D_h = 2.71 \text{ mm}$). MEPCM particles with an average size of $4.97 \mu\text{m}$ were used to form suspensions with mass concentrations ranging from 0 to 20 %. The 5 % suspension always showed a better cooling performance than water resulting in lower wall temperature and enhanced heat transfer coefficients within the range of mass flow rates. The suspensions with higher mass concentrations, however, were more effective only at low mass flow rates. At higher mass flow rates they showed a less effective cooling performance than water.

Farid et al (2007) [5] used the principle of using a suspension of microencapsules in liquid as a heat transfer fluid to improve the performance of microchannel heat sink. The microcapsules contain phase change materials which melt and solidify at a specified range of

temperature. These microcapsules improve the fluid effective specific heat capacity and thermal conductivity due to latent heat effect and micro mixing respectively. The increase in the pumping required to pump the viscous slurry will over shed the benefit in the cooling if the PCM melting range and concentration are not set properly. Hence additional investigation using this technology is required to further develop our knowledge and understanding around this topic .

Lee et al (2007) [6] used a new type of fluids called nanofluid which is a suspension consists of base fluid with some additives of metallic or non metallic solid particles in nano size as a cooling fluid. The nanofluid used in this research was water based nanofluid containing small concentrations of Al_2O_3 . The high thermal conductivity of nano particles is shown to enhance the single phase heat transfer coefficient especially for laminar flow. Higher heat transfer coefficients were achieved mostly in the entrance region of microchannels. However, the enhancement was weaker in the fully developed region, providing that the nano particles have an appreciable effect on the thermal boundary layer development.

Mushtaq et al (2009) [7] used the nanofluids as cooling fluids in a counter flow microchannel heat exchanger. They found that, using of these types of fluids instead of pure fluids lead to increase the thermal performance of this heat exchanger by increasing its effectiveness and the rate of heat transfer without extra increase in the pressure drop across heat exchanger associated with using the nanofluids. Also they found that using of nanofluids lead to increase the overall performance of a counter flow microchannel heat exchanger compared with using pure fluids.

Mushtaq et al (2009) [8] investigated numerically the effect of channels geometry (the size and shape of channels) on the performance of counter flow microchannel heat exchanger and used liquid water as a cooling fluid. They found that with decreasing the size of channels both the effectiveness of heat exchanger and pressure drop were increased and they claimed that the decision of increasing or decreasing the size of channels depends on the application in which this heat exchanger is used. Also they found that the circle is the best shape for the channels of this type of heat exchangers since it gives higher overall performance (including both the hydrodynamic and thermal performance).

It should be pointed out that most of the previous researches done in heat transfer or flow characteristics of MEPCM suspensions focused on flow in macro – channels ($D_h > 5$ mm), mostly in circular tubes [4]. Also these suspensions were not used as cooling fluids in counter flow microchannel heat exchangers up to now as to the knowledge of the authors.

2. Mathematical model

The physical model of the problem shown in Figure. (1) represents the counter flow MCHE which consists of square channels with hot and cold fluids. The difficulties in this model are the flow is developing and heat transfer is conjugated where the 3D energy equation must be solved for the two fluids and solid wall simultaneously. Solving complete heat exchanger numerically needs huge CPU time and is complicated. Therefore, and due to the geometrical and thermal symmetry between channel's rows, individual heat exchange unit which consists of two channels (hot and cold) and separating wall will be considered as shown in Figure.2 to represent the complete CFMCHE and give an adequate indication about its thermal performance [7], [8].

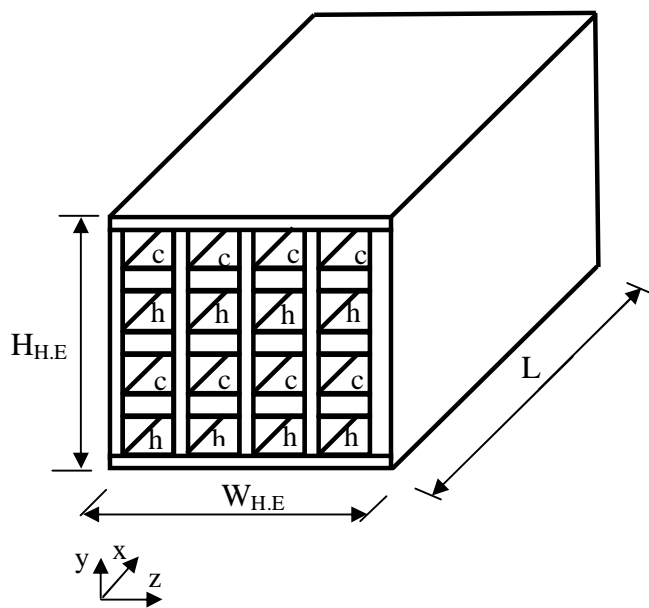
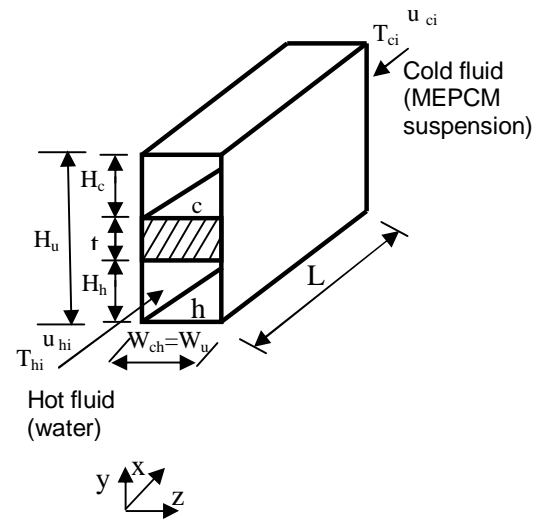


Figure (1). A schematic model of the counter flow MCHE.



Figure(2). A schematic of heat exchange unit .

3. Governing equations

The governing equations used for suspension is the same for pure fluid, the continuity, Navier- stokes and energy equations used with modified fluid properties.

The continuity equation:

$$\frac{\partial u_j}{\partial x} + \frac{\partial v_j}{\partial y} + \frac{\partial w_j}{\partial z} = 0 \quad (1)$$

Momentum equations:

$$u_j \frac{\partial u_j}{\partial x} + v_j \frac{\partial u_j}{\partial y} + w_j \frac{\partial u_j}{\partial z} = -\frac{1}{r_j} \frac{\partial P}{\partial x} + \frac{m_j}{r_j} \left(\frac{\partial^2 u_j}{\partial x^2} + \frac{\partial^2 u_j}{\partial y^2} + \frac{\partial^2 u_j}{\partial z^2} \right) \quad (2)$$

$$u_j \frac{\partial v_j}{\partial x} + v_j \frac{\partial v_j}{\partial y} + w_j \frac{\partial v_j}{\partial z} = -\frac{1}{r_j} \frac{\partial P}{\partial y} + \frac{m_j}{r_j} \left(\frac{\partial^2 v_j}{\partial x^2} + \frac{\partial^2 v_j}{\partial y^2} + \frac{\partial^2 v_j}{\partial z^2} \right) \quad (3)$$

$$u_j \frac{\partial w_j}{\partial x} + v_j \frac{\partial w_j}{\partial y} + w_j \frac{\partial w_j}{\partial z} = -\frac{1}{r_j} \frac{\partial P}{\partial z} + \frac{m_j}{r_j} \left(\frac{\partial^2 w_j}{\partial x^2} + \frac{\partial^2 w_j}{\partial y^2} + \frac{\partial^2 w_j}{\partial z^2} \right) \quad (4)$$

Where $j=h$ and c for hot and cold fluids respectively.

The energy equation based on enthalpy is [5].

$$\nabla [\vec{V} (r_f H_e)] = \nabla (k_f \nabla T_f) \quad (5)$$

Or

$$r_f \left[u \frac{\partial H_e}{\partial x} + v \frac{\partial H_e}{\partial y} + w \frac{\partial H_e}{\partial z} \right] = k_f \left[\frac{\partial^2 T_f}{\partial x^2} + \frac{\partial^2 T_f}{\partial y^2} + \frac{\partial^2 T_f}{\partial z^2} \right] \quad (6)$$

The enthalpy of the suspension (H_e) is described by equation (7) and computed as the sum of the sensible heat (h_e) and the latent heat (ΔH) of the PCM.

$$H_e = h_e + \Delta H \quad (7)$$

The sensible heat is described by equation (8), where h_{ref} is the reference enthalpy at T_{ref} [9].

$$h_e = h_{ref} + \int_{T_{ref}}^T C_{p_f} dT \quad (8)$$

The latent heat of the slurry (ΔH) is described by equation (9) as a function of the latent heat of the PCM (L), MEPCM mass fraction (f) and the melted mass fraction (β).

The melted mass fraction (β) is defined as the mass ratio of melted PCM to the total mass of PCM in the slurry. The PCM starts to melt at $T_{solidus}$ and completely melts at $T_{liquidus}$ where the liquid fraction can vary from zero at $T_{solidus}$ to one at $T_{liquidus}$. Equation (10), which is known as the lever rule, describes the melted mass fraction (β).

$$\Delta H = \beta f L \quad (9)$$

Where:

$$\begin{aligned} \beta &= 0 & \text{if} & & T_f < T_{solidus} \\ \beta &= 1 & \text{if} & & T_f > T_{liquidus} \\ \beta &= \frac{T_f - T_{solidus}}{T_{liquidus} - T_{solidus}} & \text{if} & & T_{solidus} < T_f < T_{liquidus} \end{aligned} \quad (10)$$

The energy equation for the heat exchanger solid walls:

$$k_s \nabla^2 T_s = 0 \quad (11)$$

4. Model boundary conditions

The MEPCM – water slurry, which contains micro size particles, enters the channels at a specified temperature and velocity and its temperature increases as it moves through the channels and reaches the melting temperature of PCM. When the PCM melts inside the capsules, the melted PCM remains contained in the capsules and will not mix with the carrier fluid. In other words, there is no mass transfer between the capsules and the carrier fluid. The carrier fluid exhibits lower temperature change when the PCM melts.

The boundary conditions used are:

For lower channels (Hot fluid) (water) ($0 \leq y \leq H_h$)

| Location | B.C. | Comments |
|-----------------|---|--|
| At $x = 0$ | $u_h = u_{hi}$, $v_h = w_h = 0$, $T_h = T_{hi}$ | Hot fluid inflow |
| At $x = L$ | $\frac{\partial u_h}{\partial x} = v_h = w_h = 0$, $\frac{\partial T_h}{\partial x} = 0$ | Hot fluid outflow (fully developed flow, end of channel) |
| At $z = 0$ | $u_h = v_h = w_h = 0$, $\frac{\partial T_h}{\partial z} = 0$ | No-slip, adiabatic wall |
| At $z = W_{ch}$ | $u_h = v_h = w_h = 0$, $\frac{\partial T_h}{\partial z} = 0$ | No-slip, adiabatic wall |
| At $y = 0$ | $u_h = v_h = w_h = 0$, $\frac{\partial T_h}{\partial y} = 0$ | No-slip, adiabatic wall |
| At $y = H_h$ | $u_h=v_h=w_h=0$, $-k_h \frac{\partial T_h}{\partial y} = -k_s \frac{\partial T_s}{\partial y}$, $T_h = T_s$ | Fluid -solid interface (no-slip, conjugate heat transfer) |

For upper channel (cold fluid) (PCM suspension) ($H_h+t \leq y \leq H_h+t+H_c$)

| Location | B.C. | Comments |
|-----------------|---|---|
| At $x = 0$ | $\frac{\partial u_c}{\partial x} = v_c = w_c = 0$, $\frac{\partial T_c}{\partial x} = 0$ | Cold fluid outflow (fully developed flow, end of channel) |
| At $x = L$ | $u_c = u_{ci}$, $v_c = w_c = 0$, $T_c = T_{ci}$ | Cold fluid inflow |
| At $z = 0$ | $u_c = v_c = w_c = 0$, $\frac{\partial T_c}{\partial z} = 0$ | No-slip, adiabatic wall |
| At $z = W_{ch}$ | $u_c = v_c = w_c = 0$, $\frac{\partial T_c}{\partial z} = 0$ | No-slip, adiabatic wall |
| At $y = H_h+t$ | $u_c = v_c = w_c = 0$, | Fluid-solid interface |

| | | |
|------------------------|--|------------------------------------|
| | $-k_c \frac{\partial T_c}{\partial y} = -k_s \frac{\partial T_s}{\partial y}, T_c = T_s$ | (no-slip, conjugate heat transfer) |
| At $y = H_h + t + H_c$ | $u_c = v_c = w_c = 0, \frac{\partial T_c}{\partial y} = 0$ | no-slip, adiabatic wall |

For solid wall separating two channels ($H_h \leq y \leq H_h + t$)

| Location | B.C. | Comments |
|------------------|--|-------------------------|
| At $x = 0$ | $\frac{\partial T_s}{\partial x} = 0$ | Adiabatic wall |
| At $x = L$ | $\frac{\partial T_s}{\partial x} = 0$ | Adiabatic wall |
| At $z = 0$ | $\frac{\partial T_s}{\partial z} = 0$ | Adiabatic wall |
| At $z = W_{ch}$ | $\frac{\partial T_s}{\partial z} = 0$ | Adiabatic wall |
| At $y = H_h$ | $-k_h \frac{\partial T_h}{\partial y} = -k_s \frac{\partial T_s}{\partial y}, T_h = T_s$ | Fluid - solid interface |
| At $y = H_h + t$ | $-k_c \frac{\partial T_c}{\partial y} = -k_s \frac{\partial T_s}{\partial y}, T_c = T_s$ | Fluid - solid interface |

The above equations with their boundary conditions were solved by using CFD software FLUENT 6.3 and the distributions of velocity, pressure and temperature were calculated, from which the pressure drop and effectiveness are calculated.

Heat exchanger effectiveness is the ratio of the actual heat transfer to the maximum possible heat that can be transferred:

$$e = \frac{q}{q_{\max}} \quad (12)$$

Where

$$q_{\max} = C_{\min} (T_{hi} - T_{ci})$$

$$\text{And } q = C_h (T_{hi} - T_{ho}) = C_c (T_{co} - T_{ci})$$

$$\text{Where } C_h = \dot{m} C_{p_h} \quad \text{and} \quad C_c = \dot{m} C_{p_c}$$

Total pressure drop across the heat exchange unit is:

$$\Delta P_t = \Delta P_h + \Delta P_c = (P_{hi} - P_{ho}) + (P_{ci} - P_{co}) \quad (13)$$

To calculate the overall performance of a heat exchanger taking into consideration both the thermal and hydrodynamic performance a parameter called performance index used which is the ratio of effectiveness to the total pressure drop [8]:

$$h = \frac{e}{\Delta P_t} \quad (14)$$

5. Properties of microcapsules

In general, MEPCM particles are composed of polymers as the wall material surrounds a core of PCM. The polymer wall is sufficiently flexible to accommodate volume changes that accompanied by solid / liquid phase change.

As shown in Figure (3) a single MEPCM particle consists of two parts: the outer polymer shell and the inner phase change material. The investigated MEPCM particles have an average diameter of 5 μm . The core material is n – octadecane which has a melting temperature of about 28 $^{\circ}\text{C}$, and the shell material is polymethylmethacrylat (PMMA) [4], [10], and [11].

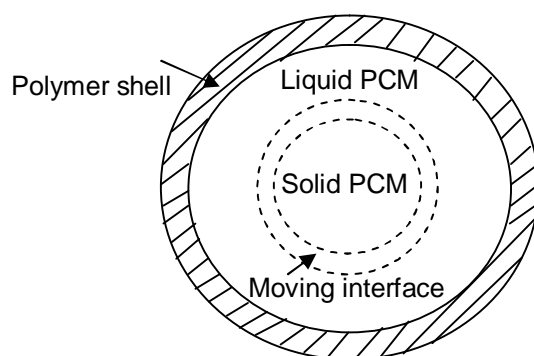


Figure (3). Sketch of a single MEPCM particle.

The core material (PCM) in a single MEPCM particle is about 70 % by volume. The selection of the suspending fluid was governed by a more important factor, its compatibility with n – octadecane and the microcapsule wall. Water was chosen as the suspending fluid because it is easy to handle and has no effect on the PCM or the microcapsule wall.

Since the thermo physical properties of the n – octadecane and the wall material are different, the properties of the microencapsules must be calculated by considering the properties of the individual components. The density and specific heat of the microencapsules were calculated by using mass and energy balance respectively, where the density of n – octadecane was taken as the mean of its solid and liquid densities [12].

$$r_{PCM} = \frac{10}{7} \left(\frac{d_c}{d_{PCM}} \right)^3 r_c \quad (15)$$

$$Cp_{PCM} = \frac{(7 Cp_c + 3 Cp_{wall}) r_c r_{wall}}{(3 r_c + 7 r_{wall}) r_{PCM}} \quad (16)$$

The thermal conductivity of the microcapsules was calculated by using the composite sphere approach. The thickness of microcapsule wall determines the heat transfer resistance of the wall material, while the heat transfer resistance of the core material was evaluated considering the model for a solid sphere in an infinite medium. Thus the thermal conductivity of the microencapsules given by:

$$\frac{1}{k_{PCM} d_{PCM}} = \frac{1}{k_c d_c} + \frac{d_{PCM} - d_c}{k_{wall} d_{PCM} d_c} \quad (17)$$

Where:

PCM : Particle (capsule = core + wall).

c : core material (phase change material).

Wall : polymer wall of the capsule.

d : diameter.

6. Properties of suspension

The bulk properties of suspension are a combination of the properties of the suspending fluid (water) and the microcapsules. Using a mass and energy balance, the density and specific heat are calculated [4], [12].

$$r_f = c r_{PCM} + (1 - c) r_w \quad (18)$$

$$Cp_f = f Cp_{PCM} + (1 - f) Cp_w \quad (19)$$

To calculate the viscosity of the suspension, the following relation was used:

$$m_f = m_w (1 - c - 1.16 c^2)^{-2.5} \quad (20)$$

This relation is valid for concentration up to 20 % and channel – to – particle diameter ratio of 20 – 100 and mean particle diameters of 0.3 – 400 μm [12].

The bulk thermal conductivity of suspension was calculated from the relation:

$$k_f = \frac{2k_w + k_{PCM} + 2c(k_{PCM} - k_w)}{2 + \frac{k_{PCM}}{k_w} - c(\frac{k_{PCM}}{k_w} - 1)} \quad (21)$$

$$f = \frac{c r_{PCM}}{(r_w + c(r_{PCM} - r_w))} \quad (22)$$

Table (1) gives the values of properties of the microcapsules and the MEPCM – water suspension calculated using the above equations.

Table(1). Physical properties of suspension components and suspension.

| fluid | Density (Kg / m ³) | Cp (J / Kg.K) | k (W / m. K) | μ (Kg / m.s) |
|----------------------------------|------------------------------------|--------------------|-------------------|-----------------------|
| water | 981.3 | 4189 | 0.643 | 0.000598 |
| n – octadecane (MEPCM core) | solid=850 liquid=780 | 2000 | 0.18 | - |
| PMMA (MEPCM wall) | 1190 | 1470 | 0.21 | - |
| MEPCM particles | 867.2 | 1899 | 0.1643 | - |
| 2 % suspension | 978 | 4148 | 0.6303 | 0.000629 |
| 5 % suspension | 975.59 | 4087.3 | 0.611 | 0.000685 |
| 10 % suspension | 969.89 | 3984.2 | 0.581 | 0.000803 |
| 15 % suspension | 964.18 | 3882.1 | 0.5519 | 0.00097 |
| 20 % suspension | 958.48 | 3774.7 | 0.523 | 0.00121 |

MEPCM volume fractions used in this paper were (2 %, 5 %, 10 %, 15 % and 20 %). Rao [3] used c up to 20 % and mentioned that when c becomes greater than 15 % the suspension behaves as a non Newtonian fluid. While Bernard [13] mentioned that the suspension up to $c = 30$ % becomes a non Newtonian fluid. Farid [5] mentioned that the suspension flow is considered to be Newtonian as long as the MEPCM particles are less than

25 %. Therefore the volume fraction used in this paper is up to 20 % to ensure that the suspension flow is a Newtonian flow.

7. Numerical model

A finite volume method (FVM) is used to convert governing equations to algebraic equations accomplished using an "upwind" scheme. The SIMPLE algorithm is used to enforce mass conservation, and to obtain the pressure field. The segregated solver is used to solve the governing integral equations for the conservation of mass, momentum and energy. CFD package FLUENT 6.3 is used to calculate the distribution of velocity, pressure and temperature in a CFMCHE. A mesh was generated by discretizing the computational domain (two channels and separating wall). Mesh independent was studied by using four mesh sizes of hexahedral element and the results for effectiveness and central velocity in fully developed region for different meshes used are listed in table 2 for $Re=50$.

Table (2) shows that the solution becomes independent of grid size and from third configuration further increase in the grids will not have a significant effect on the solution and results of such arrangement are acceptable. Therefore and for more accuracy the grid size of $(25 \times 25 \times 110)$ and $(25 \times 15 \times 110)$ is used.

Table (2). Mesh independent study.

| mesh size | $V_{f,d}$ (m /s) | Effectiveness % |
|--|------------------|-----------------|
| (16 x 16 x 90) and (16 x 8 x 90) in z, y, x directions for channels and separating wall respectively | 0.6401 | 42.82 |
| (20 x 20 x 100) and (20 x 10 x 100) in z, y, x directions for channels and wall respectively | 0.6481 | 42.41 |
| (20 x 20 x 110) and (20 x 10 x 110) in z, y, x directions for channels and wall respectively | 0.6493 | 42.26 |
| (25 x 25 x 110) and (25 x 15 x 110) in z, y, x directions for channels and wall respectively | 0.6495 | 42.21 |

The convergence criteria to control the solution for momentum and energy equations were set to be less than 10^{-6} .

8. Results and discussion

Simulations were conducted first with pure water, and then repeated with MEPCM – water slurry with volume percentages of 2 %, 5 %, 10 %, 15 %, and 20 %. Noting that the T_{solidus} for n- octadecane is 24°C (297 K) and it's $T_{\text{liquidus}} = 29^{\circ}\text{C}$ (302 K) also its latent heat $L = 245000$ (J /Kg).

To check the accuracy of present numerical model, verification was made by comparing the numerical results of present model with the numerical results of reference [5]. The numerical model presented in [5] is a microchannel heat sink has a width of 5.1 mm, height of 1.5 mm and length of 10 mm. It consists of 25 equally spaced rectangular microchannels each one with 100 μm width, 500 μm height, 10 mm length and 166.6 μm hydraulic diameter. Channels are separated by a 100 μm wall thickness of Aluminum. Due to computational difficulties of modeling the whole heat sink with 25 channels and due to symmetry in geometry of channels, the numerical model used in [5] includes only a half of individual channel with its surrounding of the heat sink metal.

Thermal boundary condition is a constant heat flux of 100 W/ cm^2 acting at the bottom wall of heat sink. The inlet velocity is 1 m/s and inlet temperature of 300 K, the PCM used with melting range of 300 - 305 K.

Figure (4) represents a distribution of bulk temperature of MEPCM-water suspension along microchannel for results of present model and numerical results of [5]. From this figure it can be seen that, the agreement between results of present model and results of [5] is accepted since the mean error for all points is 2.1 %. From these results it can be concluded that, the present model can be safely used to simulate a CFMCHE with MEPCM-water slurry as a cooling fluid.

Figure (5) shows the distribution of bulk temperature of suspension along heat exchanger for 0 % (pure water), 5 %, 10 % and 15 % of MEPCM volume concentrations at $V_i = 0.25$ m/s. From this figure one can see that the bulk temperature of suspension decreased with the increase of the volume fraction due to increase in the latent heat of melting results from adding more mount of PCM. Since the amount of heat absorbed from hot fluid in case of using MEPCM - suspension consists of sensible and latent heat. Therefore increasing volume

fraction of PCM in the suspension leads to increase the latent heat part and as a result the bulk temperature decreased.

Variation of effectiveness of heat exchanger with volume fraction for MEPCM-water suspension at $V_i = 0.25$ m/s is shown in Figure (6). From this figure one can see that, the effectiveness of the heat exchanger increased with the increase of the volume fraction of MEPCM in the suspension compared with its value for pure water. Despite the decrease in thermal conductivity of suspension with increased volume fraction, the effectiveness increases due to releasing the latent heat of melting of PCM in the suspension, which is responsible for absorbing extra heat from the hot fluid. Since the heat is transferred as a sensible and latent heat in such applications.

The percentage of modification in the effectiveness of a CFMCHE results from using MEPCM-water suspension as a cooling fluid compared with pure water is 15.83 % for volume fraction 20 % and inlet velocity 0.25 m/s.

The effectiveness of a CFMCHE can be increased more than this value by increasing the volume fraction in the suspension more than 20 % but there is a limitation on the increase of volume fraction, since increasing volume fraction more than certain level leads to change the fluid into non-Newtonian fluid therefore the volume fraction used in this paper is up to 20 % [3], [5] and [12].

Figure(7) shows the variation of pressure drop with volume fraction of MEPCM-water suspension at $V_i = 0.25$ m/s. From this figure the pressure drop increases with increasing volume fraction due to the increase in the viscosity. It's clear from this figure that, there is a large increase in pressure drop associated with using this type of fluids for cooling in a CFMCHE, since the percentage increase in pressure drop for MEPCM suspension compared with that for pure water is 50.49 % for 20 % volume fraction and 0.25 m/s inlet velocity. The increase in pressure drop results from using MEPCM-water suspension considered as one of the main disadvantages of using such fluids in this application.

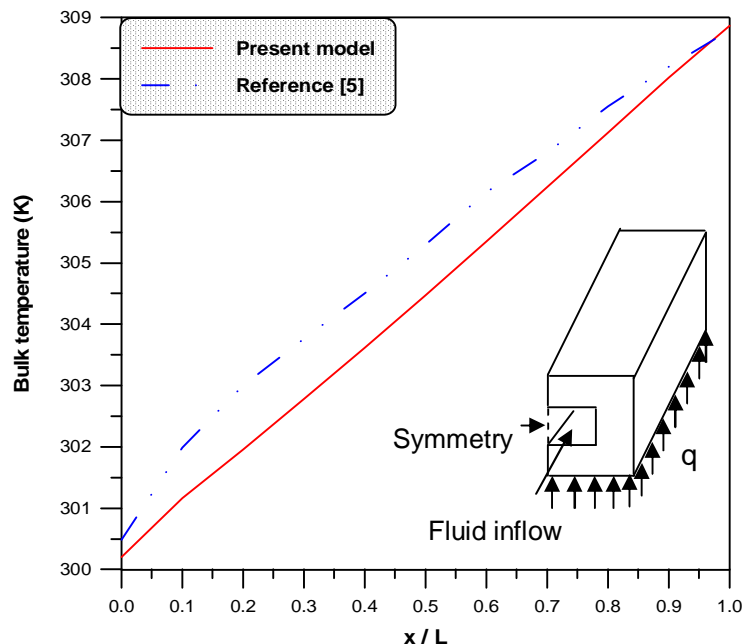
As can be seen from Figures (6) and (7) with using of MEPCM-water slurry as a cooling fluid in a CFMCHE, both effectiveness and pressure drop increased, therefore it is important to find out its effect on the overall performance of this heat exchanger.

The overall performance of a CFMCHE can be represented by a performance index which gives an indication about the overall performance.

Variation of performance index with volume fraction for MEPCM-water suspension at inlet velocity 0.25 m/s is illustrated in Figure (8). From this figure it can be seen that the

performance index for MEPCM suspension decreased with increasing volume fraction compared with that for pure water. Due to that, the increase in pressure drop is higher than the increased effectiveness by adding more amount of PCM. The value of performance index for all ranges of volume fraction used for MEPCM suspension is lower than that for pure water due to extra increase in pressure drop in suspension.

Figure (9) indicates the variation of effectiveness for 0 % (pure water), 5 %, 10 % and 15 % MEPCM volume concentrations with inlet velocity. From this figure the effectiveness decreased with the increase the velocity of flow, also the modification occurred in effectiveness due to adding of more PCM decreased with the increase in flow velocity because some of PCM in slurry did not have enough time to complete its melting inside channels which lead to decrease the latent heat of melting and reduce the cooling performance. This can be proven from Figure (10) which represents the variation of bulk temperature of suspension with inlet velocity for $c = 5\%$. From this figure it can be seen that, the bulk temperature decreases with the increase in the velocity and it reaches (300.9) K at $v_i = (3)$ m/s i.e. the temperature of suspension decreased lower than T_{solidus} . This means that, melting cannot be completed at this velocity.



Figure(4). Distribution of bulk temperature along channel as a comparison between present model and results of reference [5].

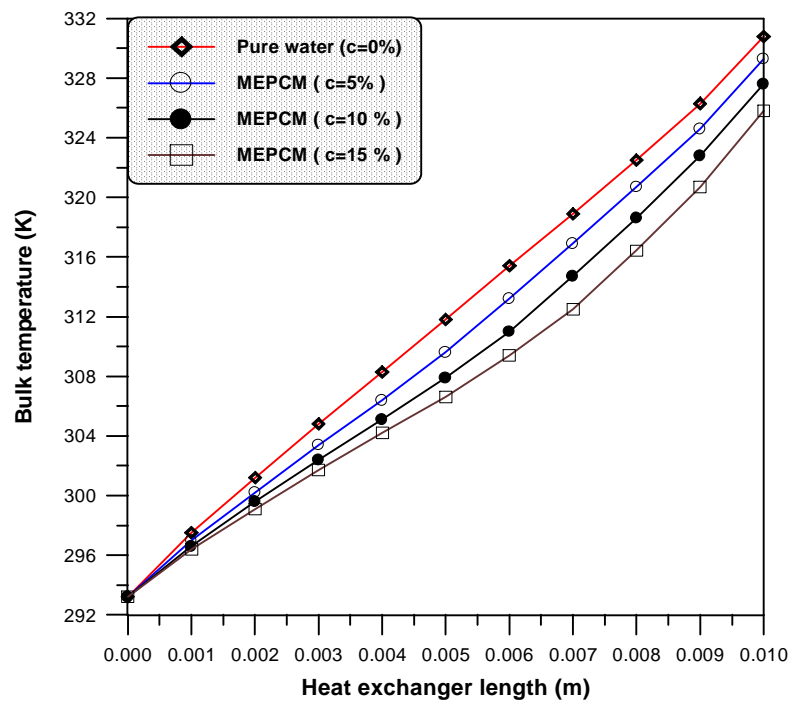
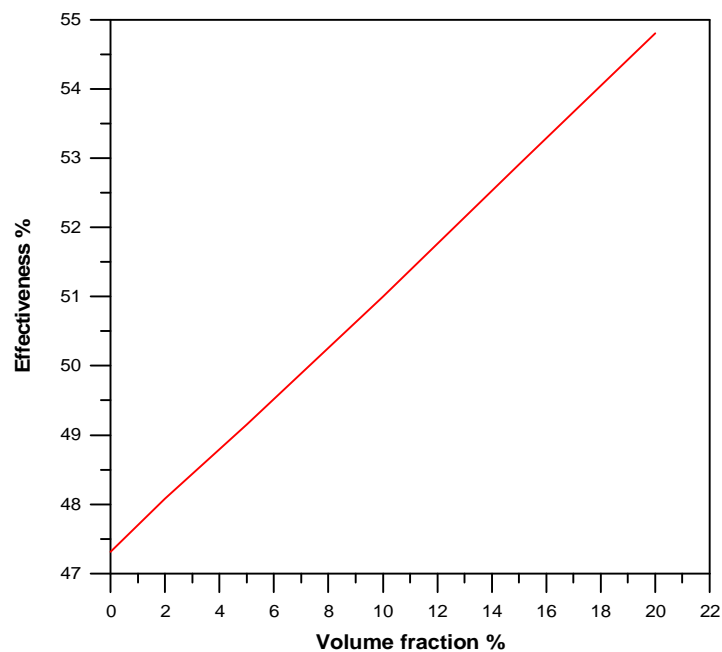
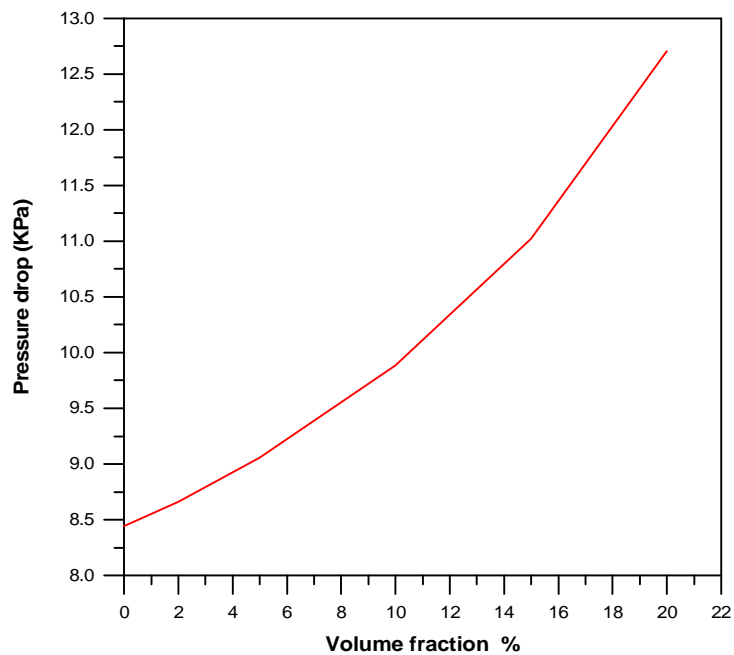


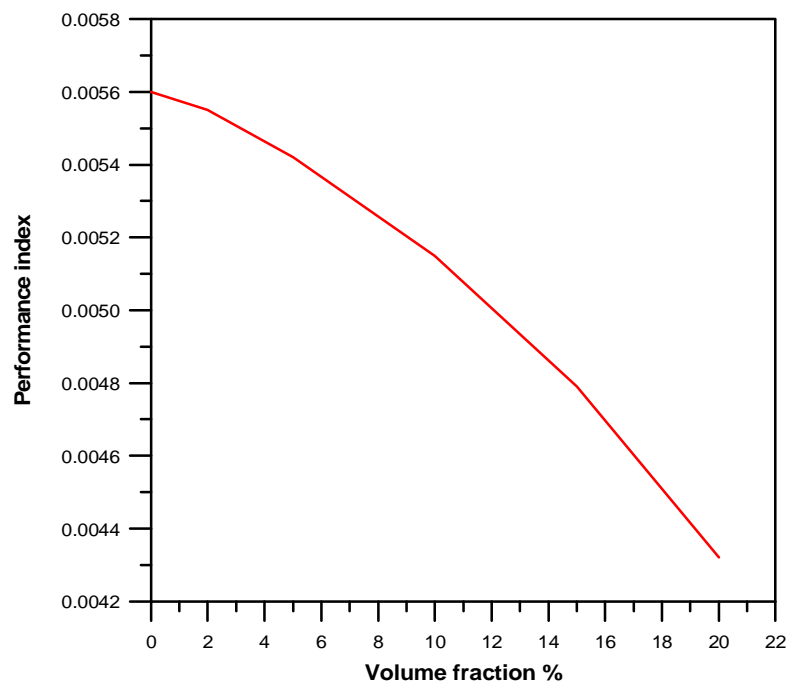
Figure (5). Distribution of bulk temperature of MEPCM suspension for different values of volume fractions ($V_i=0.25$ m/s).



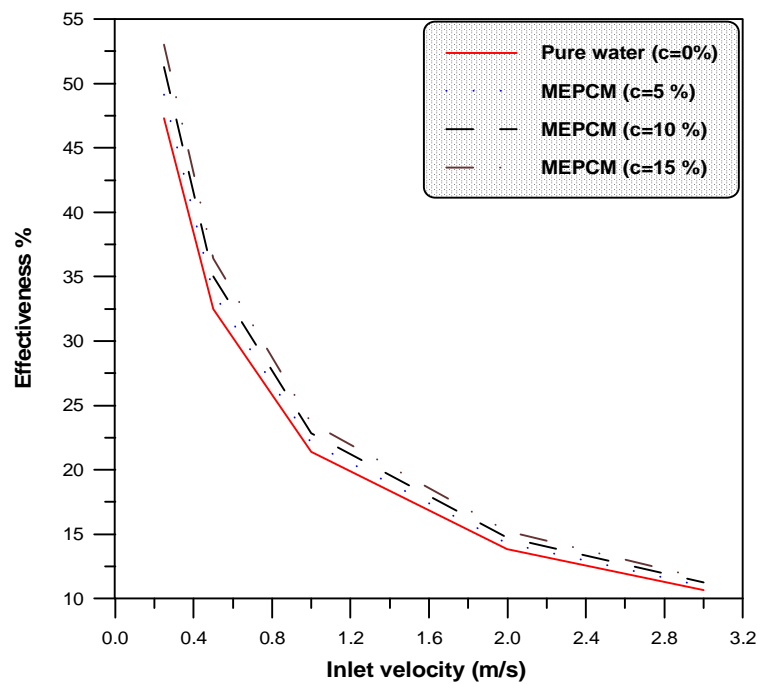
Figure(6). Variation of effectiveness with MEPCM volume fractions at $V_i = 0.25$ m/s.



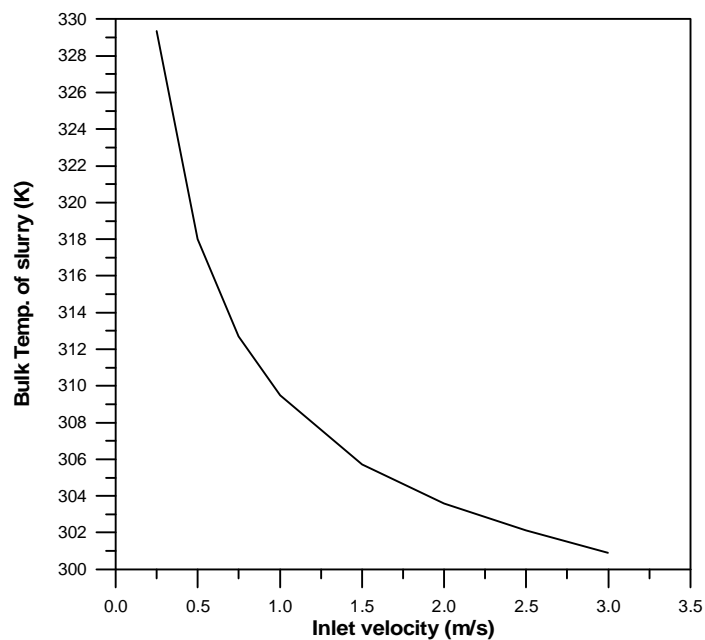
Figure(7). Variation of pressure drop with MEPCM volume fraction at $V_i = 0.25$ m/s.



Figure(8). Variation of performance index with MEPCM volume fraction at $V_i = 0.25$ m/s.



Figure(9). Variation of effectiveness with inlet velocity for different values of volume fraction.



Figure(10). Variation of suspension bulk temperature with inlet velocity for c = 5 %.

9. Conclusions

In this paper the MEPCM-water suspension was used as a cooling fluid instead of pure water in CFMCHE to modify its thermal performance. From the results the following conclusions can be drawn:

- 1- Using this type of suspension leads to modify the thermal performance of a CFMCHE by increasing its effectiveness.
- 2- The use of MEPCM-water suspension leads to increase the pressure drop across the CFMCHE to large values. And as a result it leads to decrease the overall performance of this heat exchanger.
- 3- From thermal performance point of view, the use of MEPCM suspension is desirable since it leads to increase the effectiveness. And from the hydrodynamic performance point of view using this type of suspension leads to extra increase in pressure drop and decrease the performance index. Therefore, using this type of suspension depends on the application in which a CFMCHE is used. For land base applications such as medical laboratories it is preferable to use the suspension to increase thermal performance. While in space applications the extra increase in pressure drop overcome the benefits of heat transfer enhancement.
- 4- It is better to use the MEPCM – suspension at low velocity to get the benefits of melting of PCM and releasing the latent heat.

10. References

- [1] Tuckerman, D.B. and Pease, R.F, 1981, "High Performance Heat Sinking For VLSI ", IEEE Electron. Dev. Lett. EDL-2, pp. 126-129.
- [2] Klein D., Hetsroni G., Mosyak A., 2005, " Heat Transfer Characteristics of Water and APG Surfactant Solution in a Micro-Channel Heat Sink ", Int. Journal of Multiphase flow, Vol. 31, pp. 393 - 415.
- [3] Rao Yu , Frank D., Peter S., Lin G., 2006, " Flow Frictional Characteristics of Microencapsulated Phase Change Material Suspensions Flowing Through Rectangular Minichannels ", Science in China Series E : Technological Sciences, Vol. 49, No. 4, pp. 445 - 456.
- [4] Rao Yu, Frank D., Peter S., 2007, "Convective Heat Transfer Characteristics of Microencapsulated Phase Change Material Suspensions in Minichannels", Springer, Heat Mass Transfer Vol. 44, pp. 175 - 186.
- [5] Mohammed Farid, Michael S., Rami S., S. Al Hallaj, 2007, " Miniaturized Refrigeration System With Advanced PCM Micro Encapsulation Technology ", 5th International Conference on Nanochannels , Microchannels and Minichannels, ASME ICNMM, Puebla, Mexico, June 18 - 20.

- [6] Jaeseon Lee, Issam Mudawar, 2007, " Assessment of the Effectiveness of Nanofluids for Single - Phase and Two - Phase Heat Transfer in Micro-Channels ", Int. Journal of Heat and Mass Transfer, Vol. 50, pp. 452 - 463.
- [7] Mushtaq I. Hasan, Mahmood Yaghoubi, Abdul Muhsen A. Rageb, 2009, " Improving Thermal Performance of a Counter Flow Microchannel Heat Exchanger by Using Nanofluid", Fourth International Conference on Thermal Engineering: Theory and Applications, January 12 – 14, Abu Dhabi, UAE.
- [8] Mushtaq I. H., A. A. Rageb, M. Yaghoubi, Homayon H., 2009, " Influence of Channel Geometry on the Performance of Counter Flow Microchannel Heat Exchanger", Int. Journal of thermal sciences, Vol. 48, 1607–1618.
- [9] Michael J. Moran, Howard N. Shapiro, 2006, "Fundamentals of Engineering Thermodynamics ", Fifth edition, SI Unites, John wiley and Sons, INC.
- [10] Yasushi Yamagishi, Hiromi T., Alexander T. P., Naoyuki K., 1999, "Characteristics of Microencapsulated PCM Slurry as a Heat -Transfer Fluid", AIChE Journal, Vol. 45, No. 4.
- [11] Hao Y. L., Tao Y. X., 2004, " A Numerical Model For Phase - Change Suspension Flow in Microchannels ", Taylor and Francis, Numerical heat transfer, Part A Vol. 46, pp. 55-77.
- [12] Manish Goel, Roy S. K., Sengupta S., 1994, " Laminar Forced Convection Heat Transfer In Microcapsulated Phase Change Material Suspensions ", Int. Journal of Heat and Mass Transfer, Vol. 37, No. 4, pp. 593 - 604.
- [13] Willard Bernard Jackson, 2002, "Heat Transfer Augmentation Via Microencapsulated Phase Change Material", Master thesis, Mechanical and Aerospace Engineering, Graduate faculty of North Carolina State University.

11. Nomenclature

| | |
|----------------|---|
| A | Cross-sectional area (m ²) |
| c | Volume fraction |
| C _p | Specific heat capacity (J / kg K) |
| D _h | Hydraulic diameter (m) |
| H | Channel height (m) |
| h | Convection heat transfer coefficient (W/m ² K) |
| He | Enthalpy of suspension (W) |
| he | Sensible heat (W) |
| k | Thermal conductivity (W/m K) |
| L | Heat exchanger length (m) |
| P | Total pressure (Pa) |
| q | Heat transfer rate (W) |
| t | Separating wall thickness (m) |
| T | Temperature (K) |
| u | Fluid x-component velocity (m/s) |

| | |
|------------|-----------------------------------|
| v | Fluid y-component velocity (m/s) |
| W_{ch} | Channel width (m) |
| w | Fluid z- component velocity (m/s) |
| x | Axial coordinate |
| y | Vertical coordinate |
| z | Horizontal coordinate |
| ΔH | Latent heat (W) |
| ΔP | Pressure drop (Pa) |
| \dot{m} | Mass flow rate (Kg/s) |

Greek letters

| | |
|---------------|---------------------------------------|
| ρ | Density (Kg/m ³) |
| μ | Dynamic Viscosity (m ² /s) |
| ε | Heat exchanger effectiveness |
| f | Mass fraction |
| β | Melted fraction |
| η | Performance index (1/Pa) |

Subscripts

| | |
|------|--------------------|
| c | Cold |
| ch | Channel |
| f | Suspension |
| h | Hot |
| i | Inlet |
| Max. | Maximum |
| o | Outlet |
| p | Particle |
| ref. | Reference |
| s | Solid |
| t | total |
| u | Heat exchange unit |
| w | Water |

Construction of Central Receiver -Type Field of Solar Power Plant Model

Rafid Ma'allak Hannun

Elect. Eng.Dept.
College of Engineering
Thi-Qar University

Ayad K.Khulkhal

Elect. Eng.Dept.
College of Engineering
Thi-Qar University

Mushtaq I. Hasan

Mech. Eng.Dept.
College of Engineering
Thi-Qar University

Abstract

The use of central receiver (or Power-Tower type) of heliostat as concentrators on absorber plate (target), used practically as boiler, proved convenient and favorable both in performance and cost.

In this work a model of solar thermal power plant field was designed, analyzed, fabricated and studied in details using central receiver type. The model is constructed on flat, smooth, rigid and strong plywood board used as a base for the model fixed on an inclined base at an angle of 20°. The field area was set on quarter circle to arrange the heliostats; and at the centre of a circle the tower is carrying a copper plate target was fixed. Two sets of heliostat field [(540) and (1097) mirror] were tested experimentally.

Experimental data and results obtained showed that the use of solar energy in power generation is a very promising application. The temperatures achieved for target were in the range of steam boilers operation temperatures (268- 578)C°.

The number of heliostat has a major effect on the target temperature; the power concentration factor and the overall efficiency of the system.

بناء نموذج محطة حرارية شمسية من نوع المستلم المركزي

المستخلص

إن استخدام محطات توليد الطاقة الكهربائية من نوع المستلم المركزي أو ما يسمى برج القدرة الذي يركز الأشعة بواسطة المرايا المتحركة على السطح الماص (الهدف) والذي يستخدم عملياً كمرجل قد اثبت ملائمته وأفضليته من جانبي الكفاءة والكلفة.

في هذا البحث تم تصميم وتحليل و تصنيع ودراسة نموذج حقل محطة حرارية شمسية لتوليد الكهرباء باستخدام المستلم المركزي. تم تصنيع النموذج على صفيحة خشبية ملساء صلبة وقوية كقاعدة لأجزاء النموذج مائلة بزاوية 20 درجة عن الأفق. تم تثبيت حقل المرايا على شكل ربع دائرة ، تثبت صفيحة نحاسية ماصة للحرارة في مركز هذه الدائرة. وأجري اختبار العمل على حقلين يتكونان من 540 مرآة و 1097 مرآة.

أثبتت نتائج البحث ان استخدام الطاقة الشمسية في توليد الطاقة الكهربائية هي من التطبيقات الواعدة، حيث كانت مديات درجات حرارة الهدف تتراوح بين (268-578) درجة مئوية وهي ضمن مديات توليد البخار لمراحل محطات التوليد. وكان لعدد المرايا تأثير أساسي على درجة حرارة الهدف ومعامل تركيز القدرة والكفاءة الكلية للمنظومة.

1. Introduction

Efforts to design devices for supplying renewable energy through use of the sun's ray began at least 1774[1], when the French chemist Lavoisier and the English scientist Joseph Priestley discovered oxygen. Also during the same year an impressive picture of Lavoisier was published in which he stands on a platform near the focus of a large glass lens and is carrying out other experiments with focused sunlight.

Joe [2] investigated an absorbing cavity or collector of solar energy mounted on a tower which is assumed to be erected over horizontal terrain, located about the base of the tower are many relatively small mirrors of predetermined size..These results are combined with a simple cost model to obtain a lower bound on the minimum cost per unit of redirected energy as a function of the unit mirror cost.

Sobin *et.al* [3] discussed the application of the compact steam generator technology to the design and fabrication of central receivers for solar energy powered electrical power plants. They discussed receiver design for tower – mounted applications where size and weight are important, they found the heat flux rates necessary for central solar receivers are nearly identical to the design heat fluxes for the compact steam generator, fabrication of the central receiver is discussed as well as design details and applicable materials.

Aparisi *et.al*.[4] examined the calculation of the radiation densities on the surfaces of flat and cylindrical receivers of tower- type solar power stations (SPS). They found, this calculation method is characterized by an accuracy of 20%, and in individual unfavorable cases the error may reach 30 -40%, and the results obtained using these methods were used as the basis for designing one of the variants of a cylindrical steam generator of an SPS with electric capacity about 60 MW.

Zakhidov and Ismanzhanov [5] investigated the effect of atmospheric dust particles on the reflectance of solar – installation mirrors with front and rear reflection, investigated as a function of particle time, speed, dimensions and angle of attack. They found that the atmospheric dust borne in the air and transported by the mountain – valley circulation winds characteristic of Central Asia present no danger to mirrors,

strong winds with driven dust (dust storms) cause damage to the surfaces of mirrors, especially those using front reflection, so, it is undesirable to locate solar installations in areas with frequent jet winds and loose soil (sand).

Zakhidov [6] discussed the principles of modeling in the design of solar power station mirror concentrating systems (MCS) and analyzed the various model types: substantial, structural, functional and mixed.

Teplyakov and Aparisi [7] presented a paper with the experimental solar electric station (SES-5) in light of the USSR's energy program. The paper included:

(1) Purpose of SES-5. (2) Structure of SES-5. (3) The operating principle. (4) Distinctive features. (5) Basic characteristics (Electrical output (nominal) = 5MW, Area of mirror surface = 40000 m², Dimensions of a single heliostat = 5×5m, Number of heliostat = 1600, Area of the receiving surface = 154 m², Pressure of saturated steam = 25 bar, temperature of steam = 250 C°, Annual electric power production = 5-7 million kWh).

Saiylov and Nazarov [8] determined the slope of a heliostat's primary axis which makes it possible to track the sun's apparent movement with a constant angular rate of rotation around the axis and a zero rotation around the secondary axis during the working day.

Fricker [9] investigated some 30 MW-demonstration solar power stations by using heliostat field and central receiver type. He deduced that all the systems investigated are feasible, the sodium system can probably be excluded for further investigations. He explained that the air system appears to provide the simplest, lowest risk operation; it has also by far the smallest electricity generation costs. The lower values can be attained by increasing the size of the plant into the 100MW range.

Mancini *et.al* [10, 11, 12] presented an annual review of search and development. They found that solar thermal power technologies are in different stages of development. Trough technology is commercially available today, with 355 MW currently operating in the Mojave Desert in California. Power towers are in the demonstration phase, with the 10 MW Solar Two pilot plant located in Barstow, CA, currently undergoing at least two years of testing and power production. Dish /engine technology has been demonstrated. Buck *et.al*. [13] investigated with Solar- hybrid gas turbine-based power tower systems (REFOS). They presented design and manufacturing of central receiver.

Terrado [14] investigated the economics and the finance of solar thermal power plant, he took the case study, SEGS plant in California, he explained that California in the 1980's

represented an optimum location for the development of the world 's first commercial solar thermal electric system ,high radiation an on-peak rate for electricity in summer afternoons , and tax incentives for investment in renewable energy combined initially with high fossil fuel prices, were the pre conditions for the creation of nine solar electricity generating plants (SEGS)with a total of 355 MW_e capacity.

Henry Price [15] presented paper of concentrating solar power systems (analysis & implications).It explains some of principles with market assessment important and integrated analysis tools which are essential.

Steinhagen and Trieb [16] explained the principles and development of concentrated solar-thermal power and outline its considerable potential for alleviating the constant pressure on our existing resources. They explained various types of single & dual-purpose plants have been analyzed and tested in the field. In addition, experience has been gained from the first commercial installations in use worldwide since the beginning of the 1980. Solar thermal power plants will provide a significant contribution to an efficient, economical and environmentally benign energy supply.

Fluri and Von Backstrom [17] analyzed the performance of the power conversion unit of large solar chimney power plant and compared three configurations from efficiency and energy yield point. The efficiency was 80% and increased with decreasing the diffuser area.

Rolim *et.al.* [18] developed an analytic model for a solar thermal electric generating system with parabolic trough collectors which were installed in Mojave Desert. They concluded that a large maximum of the overall cycle efficiency was found for evaporation temperatures around 320 °C with good agreement of results when comparing this model with experimental data with an attractive tool for simulation and design of solar power stations.

This paper is concerned with the study and design of a system which will concentrate direct sunlight in order to produce high temperature for the target (such as a boiler in thermal power plants). This system is made up of field of mirrors and a tower which is made for the first time in Iraq. The model includes the following items:

- (1) Parts of model, and the materials which are used in manufacturing.
- (2) Method of work and measurements.
- (3) Study of the effect of atmospheric air.
- (4) The model construction was assumed at solar noon time.

2. Theoretical analysis

In this design, the square shape area of mirror is $(2 \times 2) \text{ cm}^2$. The distance to be 2cm taken between two adjacent arcs because the places of heliostat with shape of zig- zag, and for one arc, one place of heliostat between two adjacent heliostats was neglected. Therefore, the distances between them became 2cm.

To calculate the number of heliostats in each arc by using the equation (2) (the first radius of arc of heliostats 34 cm was used to decrease the area of field for experimental use only):

$$\text{length of arc } L_a = \frac{2pR}{4} \quad (1)$$

$$\text{length of first arc} = \frac{2p * 34}{4} = 53.4 \text{ cm}$$

$$\text{Number of mirrors } N = \frac{L_a}{2L_m} + 1 \quad (2)$$

$$\text{Number of heliostats in first arc } N_i = \frac{53.4}{2 \times 2} + 1 = 14.35 \cong 14 \text{ mirror}$$

-After calculating the number of heliostats, their positions were drawn on paper. The number of heliostat for adjacent arcs are equalized or increased by one and decreased by one. One arc was created to isolate the arcs group among them to increase the number of heliostat at increasing the radius of arc and avoid the shading. At manufacturing the model the first radius of arc become 34cm to decrease the area of field and the problems of trend. The field is arranged as shown in Table (1) which explains the mirrors field arrangement calculations for two models. The first column shows the arc number begins near the tower of central receiver with arc number (1), the second column gives the radius of arc which contains the positions of mirrors. Also, the third column shows the length of arc (one quarter of circle). The forth column shows the number of mirrors in each radius. The arcs numbers (5, 11, 17, 23, 30, and 37) were used to increase the mirrors number between two adjacent arcs and to avoid the shading.

The field of heliostats was applied to the dimensions of Table (1) in figure (1) as top view of the model rig.

For designing a solar power plant, the temperature at which it will operate must be known normally in the range of $(500\text{C}^\circ - 600\text{C}^\circ)$ approximately for steam power plant and in many other power plants.[21]

Therefore, for our model, a target of copper plate of dimensions (3.5*3.5*0.15) cm , the energy which is reflected from the mirrors of the solar field , is absorbed by the target , therefore, the following analysis for the heat balance of the target applies.

-Ambient air temperature =20 C°=293K

Sky temperature $T_s=0.552 T_\infty^{1.5}$

$$\therefore T_s = 0.552 * (273 + 20)^{1.5} = 276.85 K = 3.85 C^\circ \approx 4 C^\circ$$

$$\begin{aligned} q_r &= SA(T_p^4 - T_s^4) \\ &= 5.67 \times 10^{-8} * (3.5 \times 3.5 \times 10^{-4}) (873^4 - 277^4) \\ &= 39.93 \text{ W} \end{aligned} \quad (3)$$

$$\begin{aligned} h_\infty &= c(T_p - T_\infty)^{\frac{1}{4}} \\ &= 1.77(600 - 20)^{\frac{1}{4}} \\ &= 8.686 \text{ W} / m^2 . C^\circ \end{aligned} \quad (4)$$

This coefficient is for zero wind velocity. For wind speed is higher than 5 m/s , $h_\infty=20 \text{ W} / m^2 . C^\circ$. Then ,

$$\begin{aligned} \therefore q_c &= h_\infty A(T_p - T_\infty) \\ &= 20 * (3.5 \times 3.5 \times 10^{-4}) (600 - 20) \\ &= 14.21 \text{ W} \end{aligned} \quad (5)$$

$$\begin{aligned} \therefore q_{total} &= q_r + q_c \\ \therefore q_{total} &= 39.93 + 14.21 \\ &= 54.14 \text{ W} \end{aligned} \quad (6)$$

Assuming [23],[24]:

(1) The reflection coefficient of mirror $h_p = 0.75$ (for commercially available).

(2) The guidance efficiency for heliostats $h_e = 0.8$.

(3)The optical efficiency of heliostat $h_{eo} = 0.9$.

(4)The average solar flux through one year $I_b = 700 \text{ W} / m^2$

(5)The field angle is 90° when $\theta=135^\circ$ to 180° , and $(-135^\circ$ to $180^\circ)$

(6)The power factor or cosine factor ($\cos i$, or η_{co}) ,(due to the fact that the perpendicular to the heliostat is not the same as the incident ray vector), approximately equal to (0.8) taken from the previous experiments.

(7)The absorptance of sunlight by target plate is 0.9

-As in the analysis presented by [22], it was found that:

Dimension of mirror \cong dimension of target plate $\times \cos 22.5$

$$= 3.5 \times \cos 22.5 = 3.23 \text{ cm}$$

-When the angle 22.5° is the inclination angle of the target plate from the reflected radiation from rim mirror of the field, it is half the angle of rim mirror from the horizontal plane.

-Another hint, there is declination of the solar rays with a value of 16 second of degree, measured between solar disc edge ray and center ray.

-There are some difficulties in the trend of mirrors practically. Therefore, the dimension of mirror is (2×2) cm was chosen, for the above reasons and also to lessen the dimensions of model.

Table (1). Field of mirrors arrangement calculations for two models. First model for arc number 1 – 27

| Arc No. | Arc radius cm | Length of arc cm | Mirror No. | Arc No. | Arc radius cm | Length of arc cm | M No. | Arc No. | Arc radius cm | Length of Arc cm | M No. |
|---------|---------------|------------------|------------|---------|---------------|------------------|-------|---------|---------------|------------------|-------|
| 1 | 34 | 53.4 | 14 | 15 | 62 | 97.4 | 22 | 29 | 90 | 141.4 | 31 |
| 2 | 36 | 56.5 | 15 | 16 | 64 | 100.5 | 21 | 30 | 92 | 144.5 | 25 |
| 3 | 38 | 59.7 | 14 | 17 | 66 | 103.7 | 7 | 31 | 94 | 147.7 | 38 |
| 4 | 40 | 62.8 | 15 | 18 | 68 | 106.8 | 27 | 32 | 96 | 150.8 | 37 |
| 5 | 42 | 66 | 6 | 19 | 70 | 110 | 26 | 33 | 98 | 153.9 | 38 |
| 6 | 44 | 69.1 | 17 | 20 | 72 | 113.1 | 27 | 34 | 100 | 157.1 | 37 |
| 7 | 46 | 72.3 | 17 | 21 | 74 | 116.2 | 26 | 35 | 102 | 160.2 | 38 |
| 8 | 48 | 75.4 | 17 | 22 | 76 | 119.4 | 27 | 36 | 104 | 163.4 | 37 |
| 9 | 50 | 78.5 | 17 | 23 | 78 | 122.5 | 12 | 37 | 106 | 166.5 | 30 |
| 10 | 52 | 81.7 | 17 | 24 | 80 | 125.7 | 31 | 38 | 108 | 169.6 | 43 |
| 11 | 54 | 84.8 | 8 | 25 | 82 | 128.8 | 31 | 39 | 110 | 172.8 | 43 |
| 12 | 56 | 88 | 21 | 26 | 84 | 132 | 31 | 40 | 112 | 175.9 | 43 |
| 13 | 58 | 91.1 | 22 | 27 | 86 | 135.1 | 31 | 41 | 114 | 179 | 43 |
| 14 | 60 | 94.2 | 21 | 28 | 88 | 138.2 | 31 | 42 | 116 | 182.2 | 43 |

Then the power calculated here is compared with the theoretical power equation which was analyzed by [22] ,i.e.

$$q = h_1 a I_b N A_m \cos i$$

$$54.14 = 0.75 \times 0.8 \times 0.9 \times 0.9 \times 700 \times N \times (2 \times 2 \times 10^{-4}) * 0.8$$

$$N = 497.3 \cong 498 \text{ mirror}$$

But the designer must add twice a multiple number of mirrors [23],[24] to secure power plant working for all conditions such as rain, fog, wind and dust...etc(at the absence of direct solar ray),by using special devices for storage.

Therefore the study used 540 mirrors in the first model because of problems of trend and manufacturing .Then using (1097) mirrors in the fabrication of the second model.

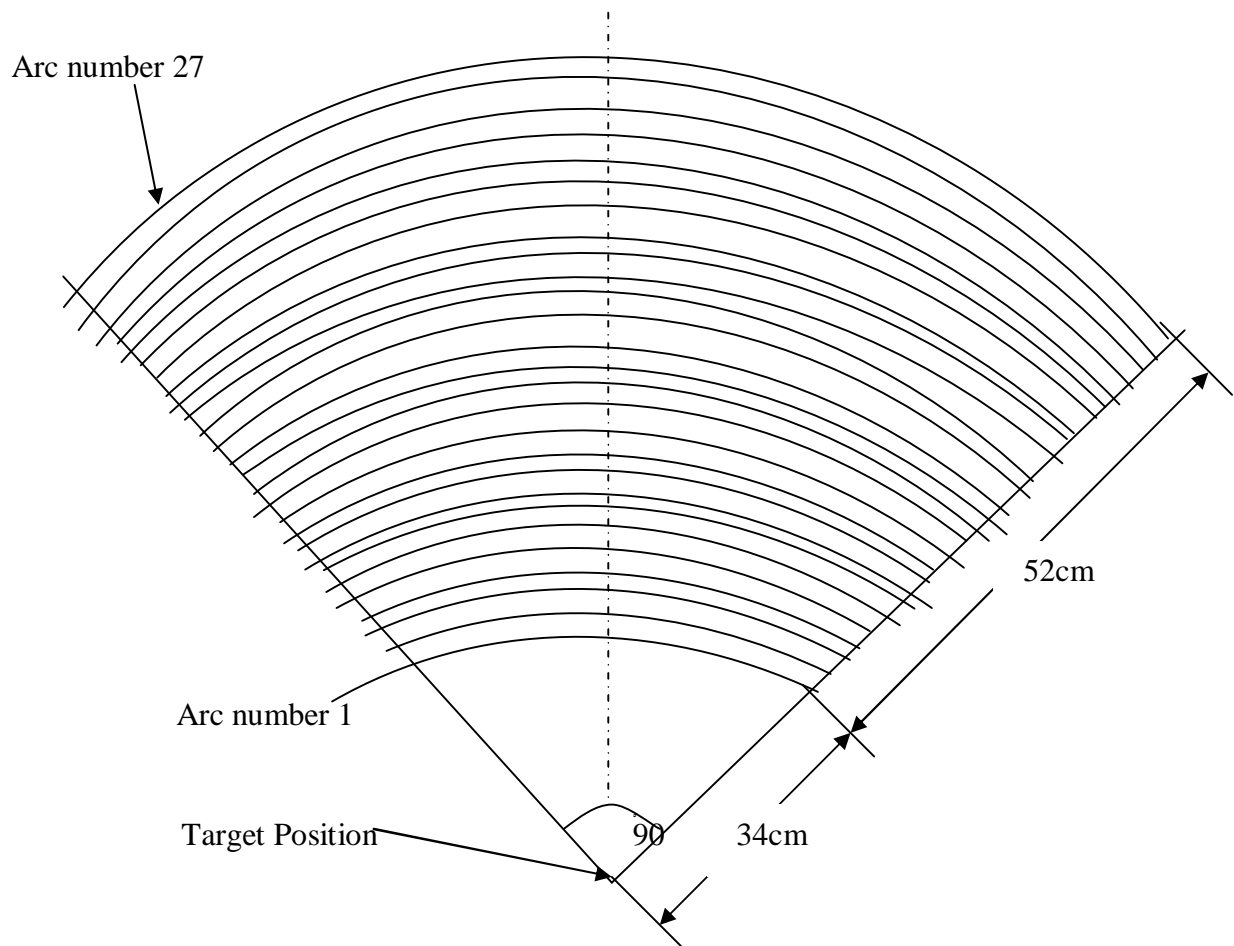


Figure (1). Heliostats Field.

3. Manufacturing of field of solar power plant

3.1. The Base of model

(1) Dimensions

Before the start of manufacturing the model base plate, its dimensions must be specified from the following measurements for the first model:

-width=the radius of outer arc of heliostat+ Factor (1)

$$=86+14=100 \text{ cm}$$

-length =The radius of outer arc of heliostat $\times \sin 45^\circ \times 2$ +Factor (2)

$$=86 \times \sin 45^\circ \times 2 + 28.4 = 150 \text{ cm}$$

The plan of arcs radii must be done and the positions of blocking the heliostats on graph paper as in Figure (1) were applied on the model. (Factor (1) and Factor (2) mean the distance between two adjacent mirrors to avoid the shading which assumed to be the total length or width of plate as integer value).

(2) Choice of plate

A base plate must be chosen with special specifications such as:

- a- Water resist: to resist the effect of rain at winter season.
- b- Temperature resist: to resist the change of temperature at different seasons without changing of its properties.
- c- Rigid wood with low flexibility to bear the heliostat and target tower and accessories without changing the trend and direction of heliostat and target.
- d- Smooth surface.

(3) Manufacturing of plate

The wood plate with dimensions (150×100) cm, is supported by a wood piece of angle 20° to the horizontal to decrease the distance between the heliostats and the absorber.

Then, engineering drawing on wooden base is achieved with the following manner:-

- (a) Limiting the position of tower at the lower edge of plate, after graphing the two perpendicular axes (West-East and South-North), the tower is fixed at the center point.
- (b) Drawing the arcs of heliostat by using a pencil and limited by rim lines of field of angle 90° .

- (c) Pointing the places of blocking the heliostats on the arcs by obvious mesh points of pencil lines.
- (d) Drilling the pointed places above with diameter of 3mm by using handle driller with drill depth of 5-7mm approximately.

3.2. Target and tower

Target plate is manufactured from pure copper plate with dimensions of (3.5×3.5) cm with thickness of 1.5mm and coated with black, non shine and non gloss paint. The choice of pure copper was get because of its high melting point, high conductivity for heat ($K=385 \text{ W/m}^\circ\text{C}$) which leads to high response to heat change, specific heat ($C_p=383 \text{ J/kg.K}$), and density ($\rho=8795 \text{ kg/m}^3$), melting point temperature is (1356 K) but the melting point of Aluminum is (933 K)[19]. When the copper coated with black paint, the absorptance α becomes 0.91 and the emittance ϵ (0.2-0.05) [20].

The net height of vertical target tower is 50cm measured from the upper plate to the surface of wood plate (the height of tower was chosen as 50cm to ensure no shading and to be higher than the maximum height of field).

The target plate is supported tightly at the upper of tower using connecting steel flexible rod with diameter of 1mm and isolating the target plate and the tower steel by using glass wool and wood insulation to insure no direct contact between them and heat transfer between the target plate and the tower steel to be insignificant.

The target plate surface is facing the mirrors in the field of mirrors.

3.3. Manufacturing of heliostat

The heliostat in this model composed from two main components, the mirror and bearer (supporting rod).

The reflecting mirror selected from small glass thickness cover to decrease the distortion of sunlight and the absorption of the solar energy spectrum when the glass includes a portion of Fe_2O_3 compositions, which appears as greenish appearance. Therefore, (water white) appearance of mirror which is pure were chosen. So, mirror type 2mm thickness with dimensions (2×2) cm.

The supporting rod of heliostat is manufactured from 1mm thickness steel flexible rod (which used to connection of steel rods in concrete casting) because of its resistance to corrosion (oxidization). The length of rod is about 5cm, curved from one side as elbow bend

to help at adhesion of mirror tightly, the other side is also curved with smaller elbow bend to utilize in supporting the heliostat on the base plate.

3.4 .Trend method and measurement

The trend of the model must be accurate when starting the work. It is achieved by using a known length rod placed near the model, fit perpendicular by using the bulb device which used in building work for measuring the levels, put the rod at different time , before, after and at the solar noon. Then, the direction of shading of rod at solar noon, points the South –North axis, and then the model trended to this direction.

The trend of heliostats made the model at solar noon all time by changing the angle of model. It starts at solar noon, limiting the shade of tower to be perpendicular and limiting the length of shade to remain at these features all time of trend and measurements, and then the direction of mirrors was moved smoothly to see the shine of mirror accurately on the target area, and repeat this process for all mirrors. It was continued to change the angle of wooden plate at all time (each five minutes approximately) to secure remaining the model at solar noon with monitoring the shade of tower (length and angle).

After the end of trend process, replacing the movable heliostat was done and then supports it with the same procedure.

So, the measurement process was started, in this paper it is able to measure the temperature of front surface of target plate by using a digital clamp thermometer type K, by welding the ball of the end of compensating wires to the target plate surface at the center to measure the temperature. This process was repeated at every hour start to remain the model at solar noon by trending the field to different slope perpendicular to sun direction (azimuth angle is 90°).

The solar noon was used in designing this model because:

- (1) This time is known at every day.
- (2) Simplicity in procedure.
- (3) Avoiding the shading or masking effects.

4. Discussion

(1) A sample of experimental results for target temperature during the day are presented in Table (2) and Figure (3) for the period 28-12-2008 to 20-3-2009 for the first model and the period 17-4-2009 to 21-5-2009 for the second model. Data accumulated for 41 experiments.

As shown in Figure (4), the trend for the target temperature change is nearly the same for both models. The band width for the temperature of the first model is (103-211)C° at 8 AM and (162 – 258) C° at 12 AM , while for the second model is (292 – 411) C° at 8 AM and (375 – 578) C° at 12 AM . These results are in a good agreement with the published results for experimental solar electric station [7]. It is worth mentioning that target temperature reaches its value at the specific measuring hour within 3 minutes from the start of the experimental measurements. Figure (3) shows the variation in the band width for the two models (i.e $\Delta T_1=108\text{ C}^\circ$, $\Delta T_2=119\text{ C}^\circ$ at morning and $\Delta T_1=96\text{ C}^\circ$, $\Delta T_2=203\text{ C}^\circ$, at noon) is mainly due to the change in atmospheric temperature during the tests (winter for the first model and late spring, early summer for the second model). Figure (3) shows the trend of measured data for the two models (Target temperatures variation during the hours of experiments) .The trend is nearly the same, however, variation in the second model is nearly twice that of the first model, and the highest temperature reached in both models was at noon .The scatter of the data is shown in Figure (4). The maximum temperature measured at noon for the first model was (258C°), while the minimum was (122 C°).

For the second model, the minimum temperature recorded at 8a.m was (292C°), this indicates clearly that the second model starting temperature at 8am is much higher than the maximum temperature recorded for the first model. Also the overall temperature range recorded for the second model is in the normal range of steam operating temperature. At the same time the recorded data shows that the lowest temperature recorded for the second model at 5pm was (268 C°), this gives as operational temperatures for a period of nine hours.

(2) Figure(5) shows the average target temperature for the two models during the days of measurements, although , the hourly average was calculated as the arithmetic average of readings at that hour , the shape of two curves resembles the behavior of temperature change during the day of the two models.

(3) Daily Efficiency = $\frac{\sum Actual\ q}{\sum Measured\ q} \times 100\%$ for the two models (18.9% for first model) and (31.7% for the second model).

(4) The average measured power calculated approximately (through one day) , (through nine hours) for second model reaching the target is :

$$\Sigma(\text{measured } q) = 1292.1 \text{ W/day}$$

while the actual power, calculated according to the model is:

$$\Sigma(\text{actual } q) = 368.2 \text{ W/day}$$

therefore, the total average daily efficiency is:

$$h_{\text{day}} = \frac{\sum q_{\text{actual}}}{\sum q_{\text{measured}}} \times 100\%$$

$$= \frac{368.2}{1292.1} \times 100\% = 28.5\%$$

But for the first model; the average measured power is (407.6/day) , the actual power is (71.36W/day), the total daily efficiency is (17.5%).

(5) From the actual and measured power were illustrated in the same values calculated in (4) above , the losses of system can be determined by using $\text{System Losses} = q_{(\text{measured})} - q_{(\text{actual})}$

$$\text{Percentage Losses} = \frac{\text{system losses}}{q_{(\text{measured})}} \times 100\%$$

(average losses = 336.24 W for first model, and average losses= 923.9 W for second model).

The percentage losses were calculated by applying the above equations to be (82.5%) for first model and it was (71.5%) for second model.

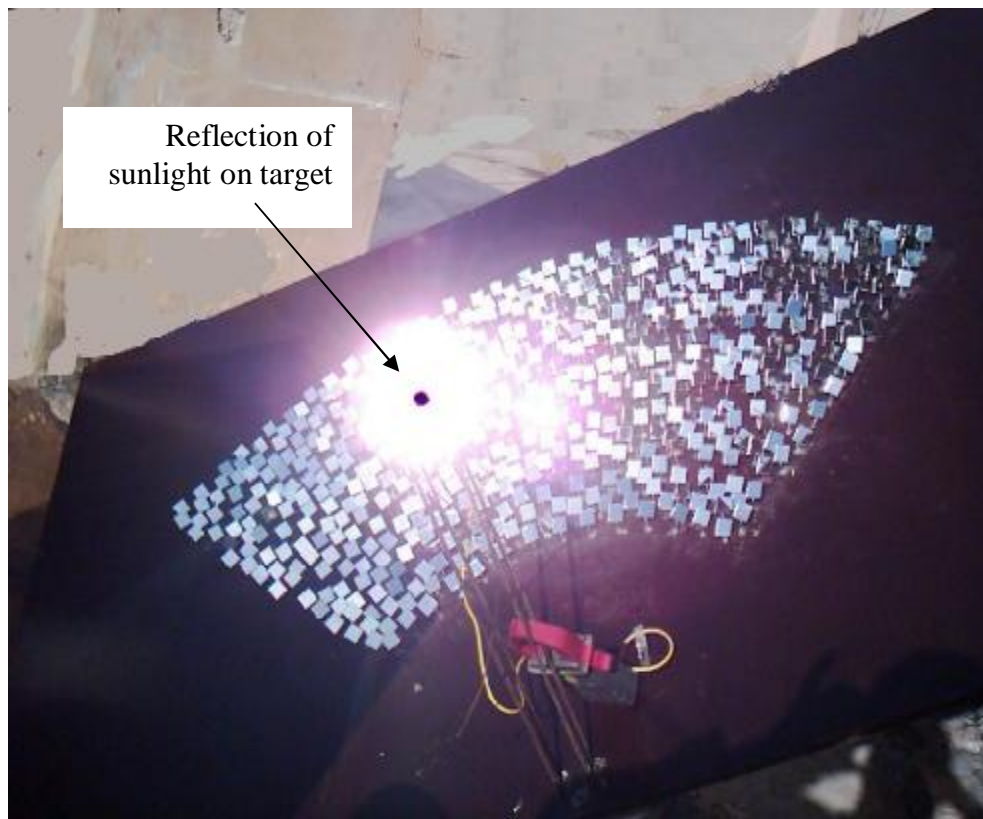
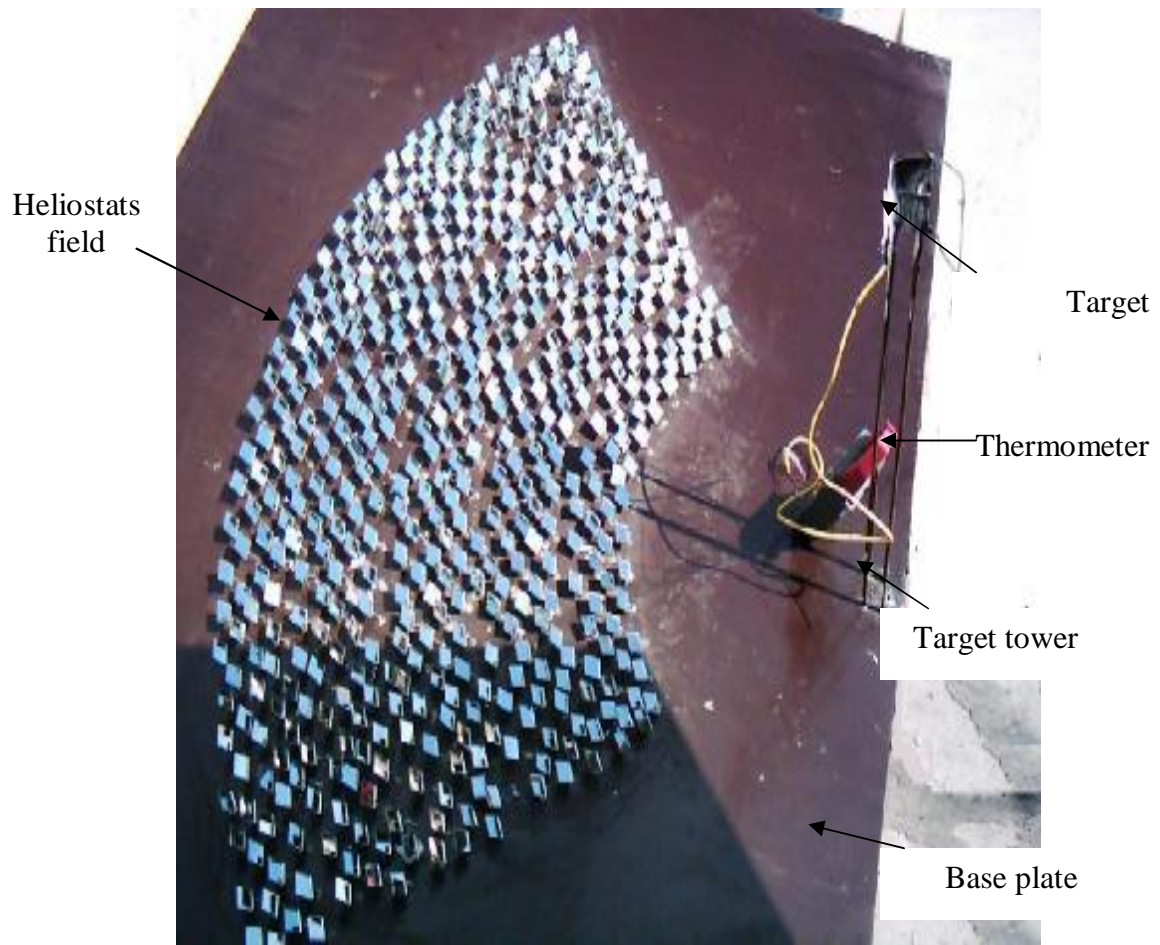
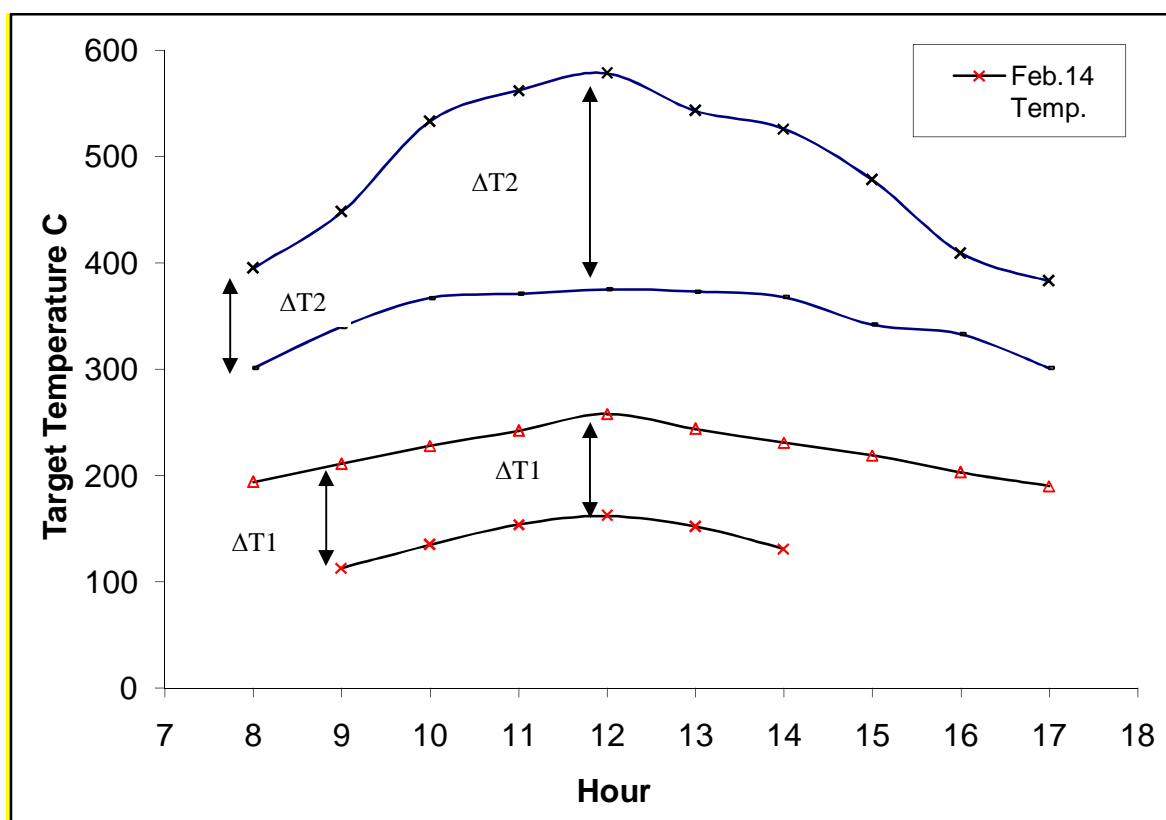


Figure (2). Shows two photographs for the first model.

Table (2). Temperature readings in °C for the first model.

| Daily time (hour) | 12-Jan | 13-Jan | 15-Jan | 20-Jan | 19-Mar | 20-Mar | 29-Dec |
|-------------------|--------|--------|--------|--------|--------|--------|--------|
| 8 | | | | | 174 | 194 | |
| 9 | | | | | 191 | 211 | 65 |
| 10 | 155 | 163 | 145 | 175 | 206 | 228 | 95 |
| 11 | 175 | 198 | 191 | 225 | 215 | 242 | 145 |
| 12 | 189 | 276 | 242 | 231 | 228 | 258 | 199.8 |
| 13 | 181 | 206 | 175 | 203 | 214 | 244 | 186 |
| 14 | 145 | 150 | fog | 154 | 201 | 231 | 145 |
| 15 | | | | | 191 | 219 | |
| 16 | | | | | 173 | 203 | |
| 17 | | | | | 161 | 190 | |

**Figure (3). Target temperature difference (ΔT_1 for first model measured at 20-3 & 14-2-2009 & ΔT_2 for second model measured at 9-5 & 17-4-2009).**

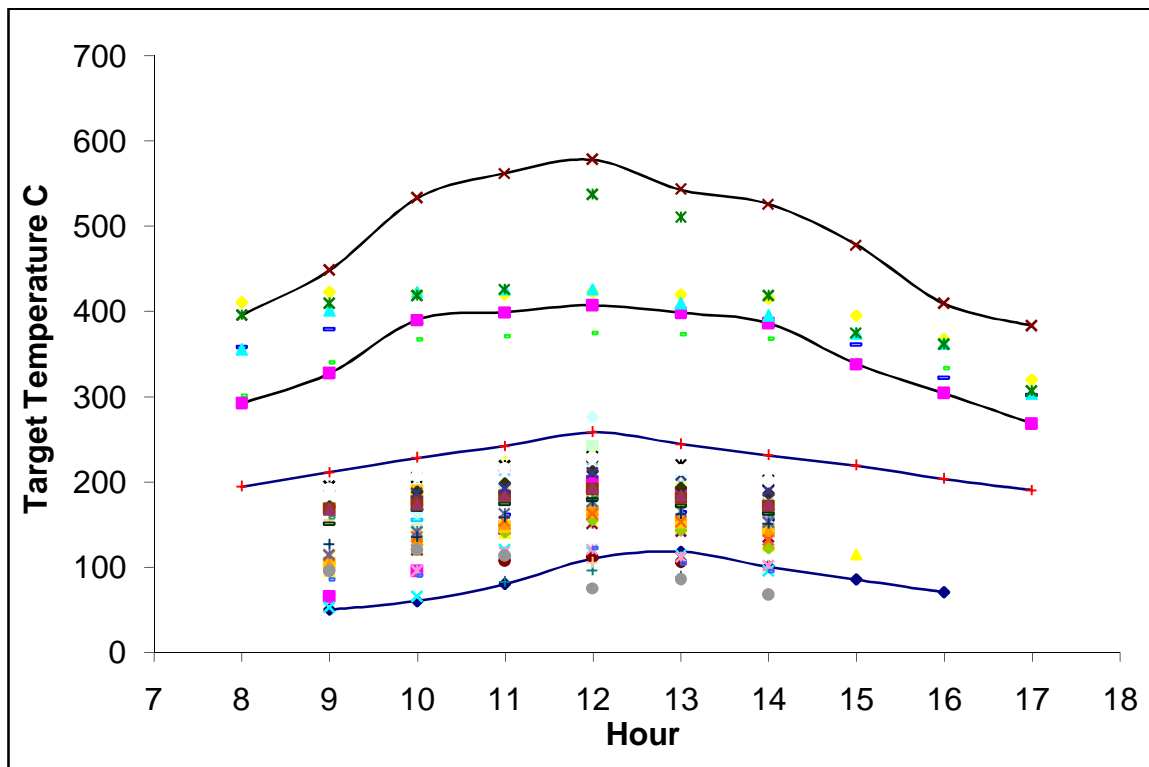


Figure (4). Target measured temperature of two models(the upper for second model & beneath for first model)through the period 28-12-2008 to 21-5-2009.

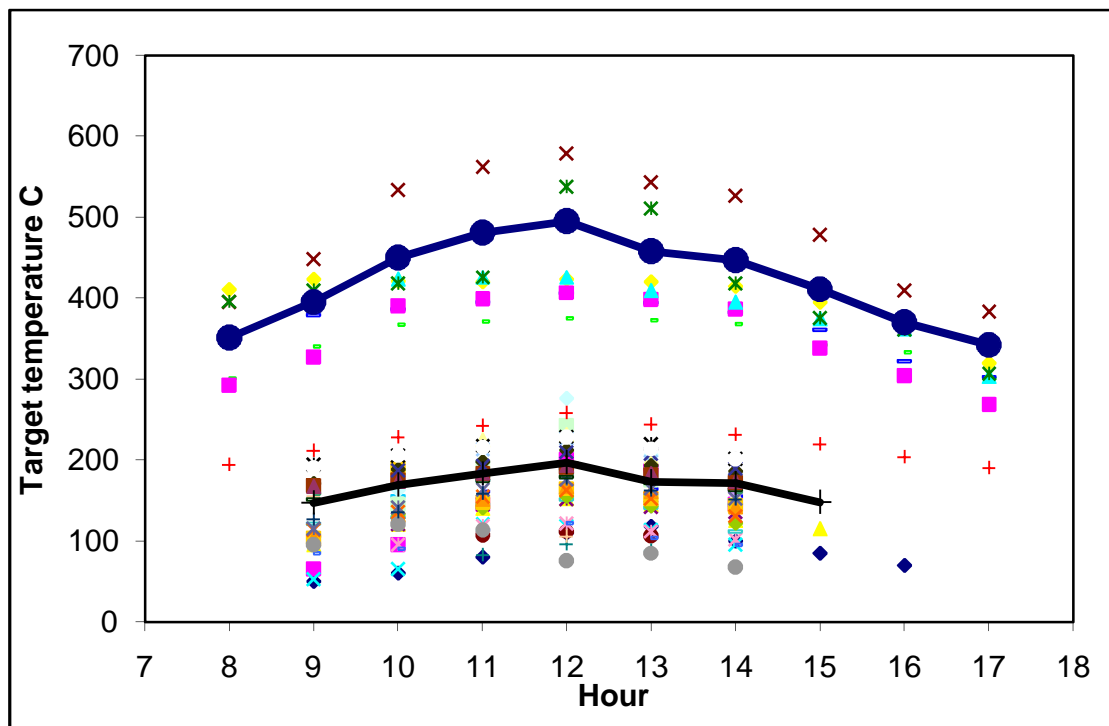


Figure (5). Average target temperature calculated for two models (upper curve for second model and beneath for first model, the other points are temperature measurements of 41 test day).

5. Conclusions

There are some notes in designing and constructing the model:

- (1) The measurements of temperature suffered from the effects of weather conditions, speed of wind, temperature of sky and air, dust, fogetc.
- (2) When the wind is slow, plate temperature increases and the solar power absorbed by target is observed.
- (3) When the weather is pure and no dust and fog the solar power absorbed is high.
- (4) When the ambient temperature is low then sky temperature is low, therefore, that leads to decrease the power absorbed.
- (5) Increasing the insulation layer thickness under the absorber plate will increase the absorbed power absorbed because of decreasing the losses.
- (6) At the measurement and trend of model in the direction to follow the sun, the angle of incidence and altitude angle change, therefore, the trend changes.
- (7) The study assumed that the altitude angle is constant for all day design in measurement.
- (8) The designer lost the utilization of solar power from about 6 mirrors because of target shading.

6. References

- [1] Aringhoff R., Brakmann G. and Teske S., 2003, "Solar Thermal Power ",Greenpeace International Report, Ed. By Aubrey C., Netherlands.
- [2] Joe D.Hankins, 1974, "Cost Optimal Deployment of Mirrors Associated with a High Temperature Solar Energy System" ,Solar Energy, 19: 73-78.
- [3] Sobin A. ,Wagner W., Easton C.R., 1974 ,"Central Collector Solar Energy Receivers ",Solar Energy, 18: 21-30.
- [4] Aparisi R.R., Teplyakov D.L. and Khantsis B.G., 1980, "Simplified Method for Calculating Radiation Density On the Surface of Tower – Type Solar Power Station Receivers", Geliotekhnika, 16(5) :29- 37.
- [5] Zakhidov R.A. ,and Ismanzhanov A., 1980 ,"Investigation of Abrasive of Atmospheric Particles on the Reflectance of Mirrors", Geliotekhnika, 16(6) :43-47.
- [6] Zakhidov R.A.,1980, "Modeling in the Design of Mirror – Type Solar Power System Concentrators", Geliotekhnika, 16(4): 27-32.

- [7] Teplyakov D.I. and Aparisi R.R., 1985, "The SES-5 Experimental Solar Electric Station in Light of the USSR'S Energy Program" *Geliotekhnika*,21(5):28-32.
- [8] Saiylov N.S. and Nazarov Sh.A., 1987, "Choice of Slope of a Heliostat's Primary Axis ", *Geliotekhnika*,23(3):32-36.
- [9] Hans W. Fricker, 1989, "30-MW-Demonstration Solar Power Station-An Investigation", Sulzer Technical Review, Swiss.
- [10] Status Report on Solar Thermal Power Plants, 1996, Pilkington Solar International : Report ISBN3-9804901-0-6.
- [11] Holl , R.J.,1989, "Status of Solar –Thermal Electric Technology", Electric Power Research Institute :December, Report GS- 6573.
- [12] Mancini ,T.,Kolb G. J. and Prairie M., 1997, "Solar Thermal Power" Advances in Solar Energy :An Annual Review of Research and Development ,Volume 11 , edited by Karl W. Boer ,American Solar Energy Society , Boulder Co , ISBN0-89553-254-9.
- [13] Reiner Buck , Thomas Brauning , Thorsten Denk , Peter Schwarzbözl ,Markus Pfander , Felix Tellez , 2001" Solar- Hybrid Gas Turbine –Based Power Tower Systems (REFOS)" , edited by ASME , Proceedings of Solar Forum ,Washington.
- [14] Terrado E., 2002, "Economics and Financing of Solar Thermal Power" Ed. IEA Solar PACES, USA.
- [15] Henry Price, 2002, "Concentrating Solar Power Systems Analysis and Implications" ,edited by Sun lab and NREL(Non-Renewable Energy Load),USA.
- [16] Hans Müller – Steinhagen ,Farnz Trieb, 2003, "Concentrating Solar Power – A Review of the Technology "Institute of Technical Thermodynamics , and Aerospace Centre , Germany.
- [17] Fluri T.P. and Von Backstrom, 2008, "Performance Analysis of the Power Conversion Unit of a Solar Chimney Power Plant", *Solar Energy*, Vol.82, pp. 999-1008.
- [18] Rolim M.M., Fraidenraich N. and Tiba C., 2009, "Analytic Modeling of a Solar Power Plant with Parabolic Linear Collectors", *Solar Energy*, Vol.83, pp.126-133.
- [19] Holman J.P., 1976, "Heat Transfer ", ©McGRAW-Hill KOGAKUSHA. LTD ,Tokyo.
- [20] Agnihotri O.P. and Gupta B.K., 1981, "Solar Selective Surfaces ", Wiley – Inter science Publication , New York, :58-115.
- [21] Rai G.D., 1987,"Solar Energy Utilization", Copyright by Khanna Publishers, Delhi , :295-309.
- [22] Hannun R.M., 2005, " Modeling of Solar Thermal Power Plant" , MSc.thesis, University of Technology, Mechanical Engineering Department, Baghdad.

- [23] Aparisi R.R. , 1980, "Method of Calculating Shading of Heliostats in Tower – Type Solar Power Plants" ,Geliotekhnika, 16(2): 22- 27.
- [24] Manual Romero , Maria J. Marcos , Rafael Osuna , Valerio Ferna'ndez, 2000, "Design and Implementation Plan of A 10MW Solar Tower Power Plant Based on Volumetric –Air Technology in Seville(Spain)"proceedings of the Solar 2000 , Solar Power Life – Share the Energy ,Madison ,ASME.

7. Nomenclature

| <u>symbol</u> | <u>Definition</u> | <u>Unit</u> |
|---------------|---|-----------------|
| A' | Absorber area | m^2 |
| A_m | Mirror area | m^2 |
| C_p | Specific heat of plate with constant pressure | J/Kg.K |
| h_∞ | convection heat transfer coefficient | $W/m^2.C^\circ$ |
| i | Solar incidence angle | Degree |
| N | Number of mirrors | - |
| q | Power | Watt |
| q_c | convective heat | Watt |
| q_e | electrical power | Watt |
| q_r | radiated heat | Watt |
| q_s | storage heat | Watt |
| t | Time | Second |
| T | Temperature | C° |
| T_p | Plate temperature | C° |
| T_s | Sky temperature | C° |
| T_∞ | Ambient air temperature | C° |
| α | Absorptance of target plate | - |
| ε | Emissivity of target plate | - |
| η | Efficiency of system | % |
| σ | Stefan- Boltzmann constant | $W/m^2.K^4$ |

Reduction of Peak to Average Power Ratio in OFDM System Using Discrete Cosine Transform Technique

Ahmed K. Abed

Electrical & Electronic Department

College of Engineering

Thi-Qar University

Abstract

Orthogonal frequency division multiplexing (OFDM) is a form of multi-carrier modulation technique with high spectral efficiency, robustness to channel fading and immunity to impulse interference. Recently, it is being used for both wireless and wired high data rate communications. Despite of its many advantages, OFDM has a main drawback, namely high Peak to Average Power Ratio (PAPR). High PAPR causes saturation in power amplifiers, and leads to inter-modulation products among the sub carriers and disturbing out of band energy. Therefore, it is desirable to reduce the PAPR. In this paper we used Inverse Discrete Cosine Transform (IDCT) technique in the transmitter side to reduce PAPR problem. The use of this technique in the output of Inverse Fast Fourier Transform (IFFT) stage gave good results toward reduction PAPR. The receiver side includes Discrete Cosine Transform to achieve correct detection. Computer simulation tests have been applied on IEEE 802.11a standard as OFDM practical system with the proposed method. The results exhibit the ability of such techniques to reduce the PAPR with no major effect on the system performance as compared with the conventional OFDM technique.

Keywords: OFDM, Peak to Average Power Ratio (PAPR), IEEE 802.11a, Rayleigh Fading channel, Discrete Cosine Transform, Additive White Gaussian Noise (AWGN).

المستخلص

يُعد الإرسال المتعدد بتقسيم التردد المتعامد OFDM تقنية عالية الكفاءة باستغلال الطيف الترددي لهيئة التضمين متعدد الحامل و مقاوم إلى خفوت القناة والحصانة من التداخل. حديثاً، استخدم نظام OFDM للإرسال اللاسلكي وللاتصالات السلكية الرقمية ذات معدل الإرسال العالي. على الرغم من المحاسن الكثيرة للنظام، OFDM يمتلك عيب رئيسي هو ارتفاع نسبة أعلى إلى معدل القدرة PAPR. ارتفاع PAPR يجعل المكبرات تعمل بمنطقة التشبع، مما يؤدي إلى التداخل بين النواقل الفرعية في النطاق الترددي و الإرسال الغير المرغوب به خارج النطاق المحدد. لذلك أصبح من

المرغوب به تقليل ارتفاع نسبة أعلى إلى معدل القدرة PAPR. في هذا البحث استخدمنا تقنية معكوس تحويل الجيب تمام المجزئة IDCT في جهة الإرسال لتقليل مشكلة PAPR في نظام OFDM. ان استخدام هذه التقنية من بعد إخراج معكوس تحويل فورير السريعة أعطت نتائج جيدة باتجاه تقليل PAPR. جهة الاستقبال تضمنت استخدام تحويل الجيب تمام المجزئة DCT للكشف الصحيح للبيانات. تمت محاكاة النظام المقترح ضمن نظام IEEE 802.11a كنظام معتمد عمليا باستخدام الحاسوب. النتائج أظهرت قدرة النظام المقترح لتقليل ارتفاع PAPR بدون حدوث أي تأثير رئيسي على أداء النظام المقترح بالمقارنة مع نظام OFDM التقليدي.

1. Introduction

Orthogonal Frequency Division Multiplexing (OFDM) is a multicarrier transmission technique which is widely adopted in different communication applications. OFDM prevents Inter Symbol Interference (ISI) by inserting a guard interval and mitigates the frequency selectivity of a multi-path channel by using a simple equalizer. This simplifies the design of the receiver and leads to inexpensive hardware implementations. OFDM has been employed in diverse wired and wireless applications. For instance, in digital audio and video broadcasting[1], digital subscriber lines using discrete multi-tone [2], the wireless LAN systems such as, IEEE802.11, HIPERLAN and MMAC[3], wireless broadband service[4] and also is a strong candidate for next generation cellular systems[5]. OFDM systems have the inherent problem of high Peak to Average Power Ratio(PAPR). Peak power level of an OFDM signal is much higher than the average power due to addition of large number of subcarriers in phase. A large PAPR brings disadvantages like an increased complexity of the Analog – to – Digital (A/D) and Digital – to – Analog (D/A) converters and a reduced efficiency of the RF power amplifier. There have been two sorts of approaches to deal with PAPR of OFDM, one includes amplitude clipping [6], clipping and filtering [7], coding [8], active constellation extension (ACE) [9]; and the other one, which can be regarded as multiple signal representation technique, contains partial transmit sequence (PTS) [10], selected mapping (SLM) [11], erasure pattern selection (EPS) [12] and interleaving [13]. The latter type is also called probabilistic method, and attracts most of the attention. The character of this kind of methods is not to eliminate PAPR completely, but to reduce the probability of its occurrence.

In this paper, we proposed a technique to reduce PAPR in OFDM system using Inverse Discrete Cosine Transform IDCT scheme. The kernel concept of the proposed scheme is based on the ability of IDCT transform to rearrange the energy of signal in closed levels in time domain ,and the signal completely de-correlated in transform domain [14]. At the same

time, the proposed scheme greatly reduce the Peak to Average Power Ratio and the system as character of low complexity hardware and without transmitted side information.

2. Fundamentals of OFDM system

An OFDM symbol consists of N subcarriers by the frequency spacing of Δf . Thus, the total bandwidth B will be divided into N equally spaced subcarriers and all the subcarriers are orthogonal to each other within a time interval of length $T=1/\Delta f$. Each subcarrier can be modulated independently with the complex modulation symbol $X_{m,n}$, where m is a time index and n is a subcarrier index. Then within the time interval T the following signal of the m -th OFDM block period can be described by equation [15]:

$$x_m(t) = \frac{1}{\sqrt{N}} \sum_{n=0}^{N-1} X_{m,n} g_n(t - mT) \quad (1)$$

Where, $g_n(t)$ is:

$$g_n(t) = \begin{cases} \exp(j2\pi n \Delta f t), & 0 \leq t \leq T \\ 0 & \text{elsewhere} \end{cases}$$

The total continuous time signal $x(t)$ consisting of all the OFDM blocks is given by:

$$x(t) = \frac{1}{\sqrt{N}} \sum_{m=0}^{\infty} \sum_{n=0}^{N-1} X_{m,n} g_n(t - mT) \quad (2)$$

Consider a single OFDM symbol, since $m=0$ and $X_{m,n}$ can be replaced by X_n . Then, the OFDM signal can be described as follows:

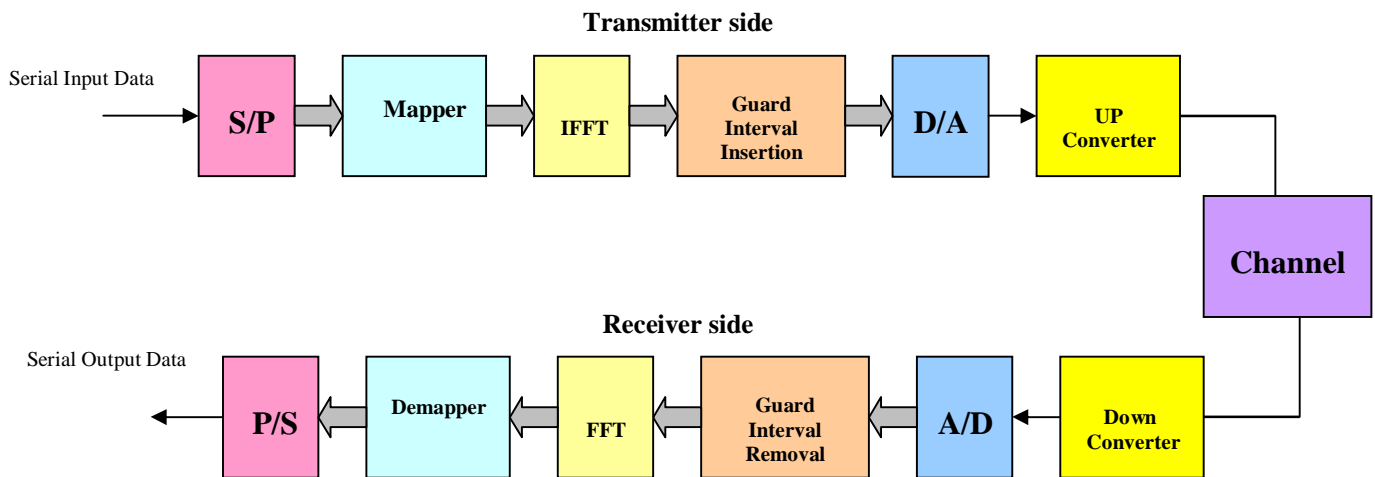
$$x(t) = \frac{1}{\sqrt{N}} \sum_{n=0}^{N-1} X_n e^{j2\pi n \Delta f t} \quad (3)$$

If the bandwidth of the OFDM signal is $B=N \times \Delta f$ and the signal $x(t)$ is sampled by the sampling time of $\Delta t=1/B=1/(N\Delta f)$, then the OFDM signal in discrete time form can be written as:

$$x_k = \frac{1}{\sqrt{N}} \sum_{n=0}^{N-1} X_n e^{j2\pi kn/N} \quad k=0, 1, 2, \dots, N-1 \quad (4)$$

where, n denotes the index in frequency domain and X_n is the complex symbol in frequency domain. Furthermore, equation (4) can be expressed using the IFFT [16].

Figure (1). shows a typical system block diagram of an Basic OFDM system. The serial input data stream is converted to N parallel subchannels and mapping with a selected modulation scheme, resulting in N subchannels containing information in complex number form.



Figure(1). Block diagram of the basic OFDM system.

These complex values are then sent to the N channel IFFT. The parallel signals are converted back to a serial sequence by using a P/S device. A guard interval is inserted to reduce the effect of ISI caused by multipath propagation. Finally, the signal is converted to analogue signal and converted back up to a form suitable for transmission. At the receiver, a reverse procedure is used to demodulate the OFDM signal.

3. PAPR in OFDM system

Consider an OFDM with N sub carriers. Each OFDM block(OFDM symol), $x(t)$, $0 \leq t \leq T$, consists of N complex base band data $x_0, x_1, x_2, \dots, x_{N-1}$ carried on the N subcarriers respectively for a symbol period of T . According to eq.(4), the peak instantaneous power is:

$$P_{\max} = \max_{t \in [0, T]} |x(t)|^2 \quad (5)$$

An OFDM symbol sequence can be represented by $x(t)$, $x(t+T)$, $\dots, x(t+mT)$, \dots

The average power of OFDM symbol sequence as following:

$$P_{\text{av}}(x_0, x_1, x_2, \dots, x_{n-1}) = \frac{1}{N} \sum_{k=0}^{N-1} E[|x_k|^2] \quad (6)$$

Where $E[|x_k|^2]$ is the expected value of $|x_k|^2$. The PAPR of the OFDM symbol $x(t)$ is:

$$\text{PAPR} = \frac{P_{\max}}{P_{\text{av}}(x_0, x_1, \dots, x_{N-1})} = \frac{\max_{t \in [0, T]} |x(t)|^2}{\frac{1}{N} \sum_{k=0}^{N-1} E[|x_k|^2]} \quad (7)$$

If the power of input signal is standard; i. e. the $E[|x_k|^2] = 1$; then :

$$\max_{t \in [0, T]} |x(t)|^2 = \max_{t \in [0, T]} \left| \frac{1}{\sqrt{N}} \sum_{k=0}^{N-1} X_k e^{\frac{j2\pi k t}{N}} \right|^2 \leq N \quad (8)$$

As a result, the PAPR value is not larger than the number N of sub carriers, e.g. the peak power value of OFDM signals is N times larger than its average power. So, the maximum of PAPR equals to N . With the increase in the number N of sub channels, the maximum of PAPR increases linearly. This makes high demands on the linear range of the front-end amplifier in sending side.

Although the probability of largest PAPR is low, in order to transfer these high PAPR of OFDM signal with non-distortion, all the linearity of the HPA in sending side, the front-end amplifier and A/D converter should meet the high requirement. But these equipments meeting the high requirement are expensive. Therefore, it is necessary and important to reduce PAPR in OFDM system.

4. Distribution of the PAPR in OFDM system

For an OFDM signal with N subcarriers, the PAPR can be defined as [17].

$$PAPR = \frac{\max |x(t)|^2}{E|x(t)|^2} \quad (9)$$

In particular, a base band OFDM signal with N subchannels has maximum PAPR equal[18] :

$$PAPR_{max} = 10 \log_{10}(N) \quad (10)$$

For M-PSK modulation, there are only M^2 sequences having maximum PAPR equal to $10 \log(N)$ as described in [18]. This means, the number of sequences that gives very high PAPR is not very high (for BPSK $M=2$ then only 4 sequence from 2^N have maximum PAPR equal $10 \log(N)$). If the number of subchannels increases, the ratio of the sequence (R) that gives so much PAPR and all distinct sequences decreases rapidly. The overall number of distinct sequences for the N subcarriers OFDM system with M-PSK is M^N . Thus the ratio can be obtained by equation (11) as:

$$R = \frac{M^2}{M^N} = M^{2-N} \quad (11)$$

From the central limit theorem, it follows that for large values of N ($N > 64$), the real and imaginary values of $x(t)$ become Gaussian distributed. Therefore the amplitude of the OFDM signal has Rayleigh distribution, with a cumulative distribution given by $F(z) = 1 - e^{-z}$. The probability that the PAPR is below a threshold level can be written as:

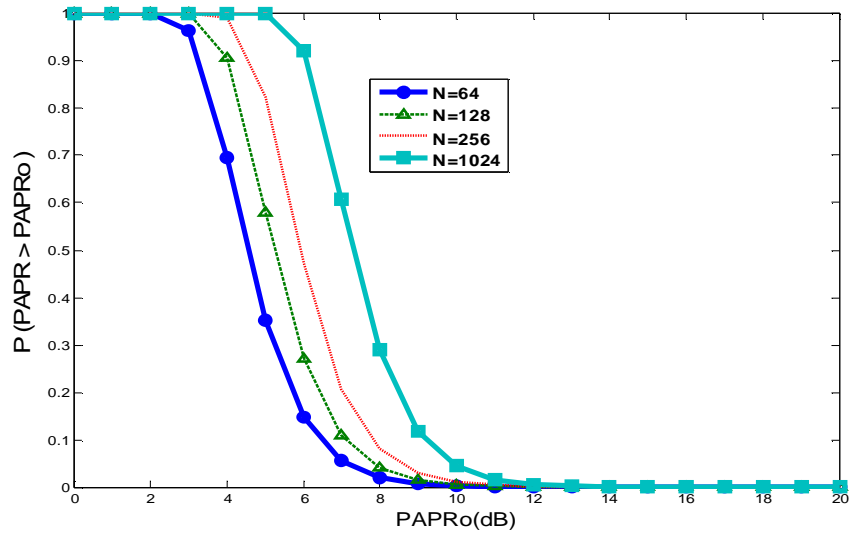
$$P(PAPR \leq z) = (1 - e^{-z})^N \quad (12)$$

The Complementary Cumulative Distribution Function (CCDF) of PAPR of an OFDM is usually used, and can be expressed as:

$$P(PAPR \geq PAPR_o) = 1 - (1 - e^{-PAPR_o})^N \quad (13)$$

Where $PAPR_o$ is the threshold power (dB).

This theoretical derivation is plotted against simulated values in Fig.(2) for different values of N.



Figure(2). CCDF for different values of subcarriers .

5. IDCT – OFDM proposed technique

Discrete Cosine Transform (**DCT**) used in most digital signal processing such as digital image processing. The most common DCT definition of a 1-D sequence of length N is:-

$$X_{DCT}(u) = a(u) \sum_{i=0}^{N-1} x(i) \cos\left(\frac{p(2i+1)u}{2N}\right) \quad (14)$$

for $u=0,1,2,\dots,N-1$.

Similarly, the inverse transformation IDCT is defined as:

$$x(i) = a(u) \sum_{u=0}^{N-1} X_{DCT}(u) \cos\left(\frac{p(2i+1)u}{2N}\right) \quad (15)$$

For $i=0, 1, 2, \dots, N-1$. In both equations (14) & (15).

$$a(u) = \begin{cases} \sqrt{\frac{1}{N}} & \text{for } u = 0 \\ \sqrt{\frac{2}{N}} & \text{for } u \neq 0 \end{cases}$$

In this paper ,Inverse Discrete Cosine Transform (IDCT) is cascaded after IFFT to insure the required redistribution power of subcarriers. The orthogonality of subcarriers in OFDM signal maintained because of the orthogonality and decorrelated property of IDCT [19]. The original signal can be resumed if DCT is inserted before FFT. DCT-OFDM system block is shown in Figure(3).

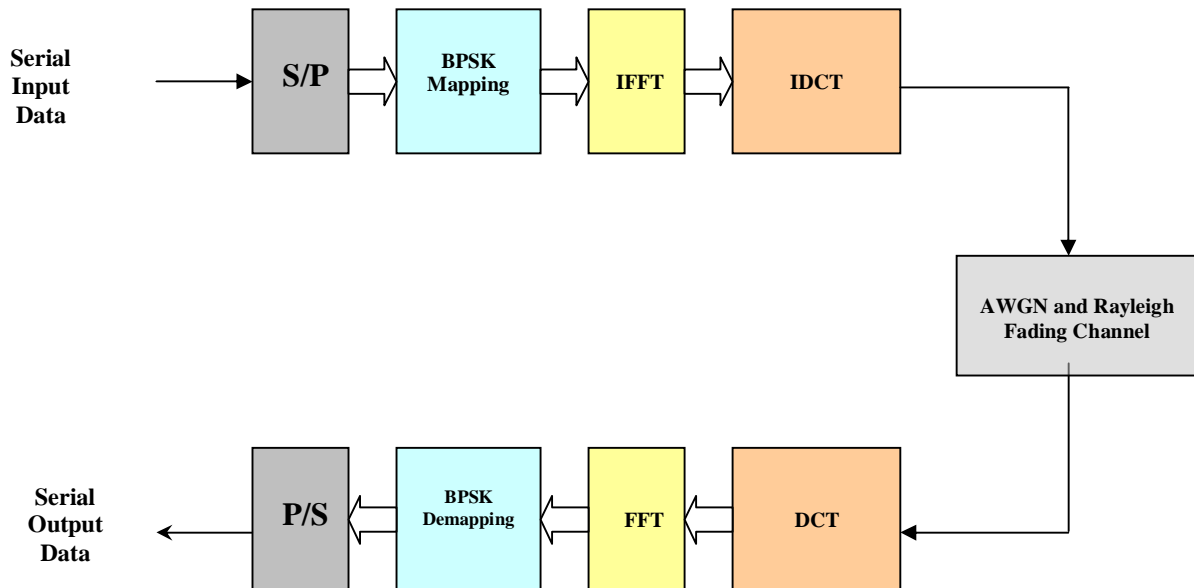


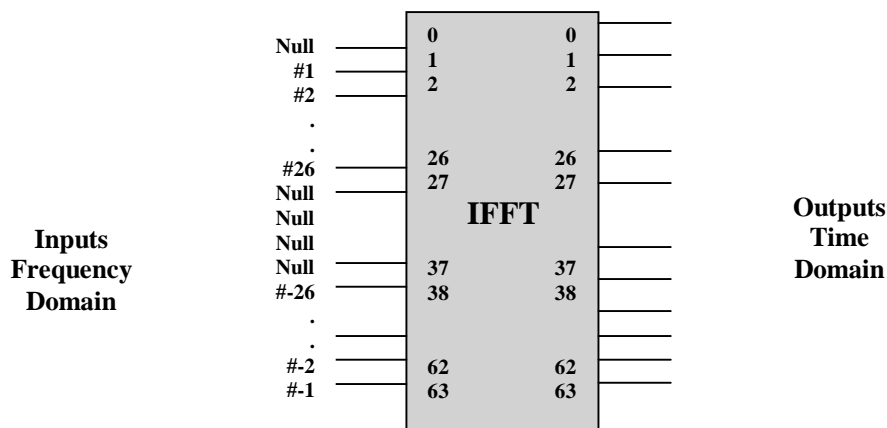
Figure (3). Block diagram of proposed scheme.

6. OFDM simulation model

The model of DCT-OFDM transmitter and receiver was made in MATLAB 7.6 (R2008a) octave codes. For all simulated tests, the IEEE 802.11a as standard wireless LAN OFDM system is used with 640 K symbols.

IEEE 802.11a used as Wireless LAN communication system. The IEEE 802.11a standard specifies an OFDM physical layer (PHY) that splits an information signal across 52 separate subcarriers to provide transmission of data at a different rate. Four of the subcarriers are pilot that the system uses as a reference to disregard frequency or phase shifts of the signal during transmission. A pseudo binary sequence is sent through the pilot subchannels to

prevent the generation of spectral lines. The remaining 48 subcarriers provide separate pathways for sending the information in a parallel fashion. The resulting subcarrier frequency spacing is 0.3125 MHz (for a 20 MHz) with 64 possible subcarrier frequency. Binary Phase Shift Keying used as a modulation technique. A 64-point IFFT is used, the coefficients 1 to 26 are mapped to the same numbered IFFT inputs, while the coefficients -26 to -1 are copied into IFFT inputs 38 to 63. The rest of the inputs, 27 to 37 and the 0 (dc) input, are set to zero. This mapping is illustrated in Figure (4).

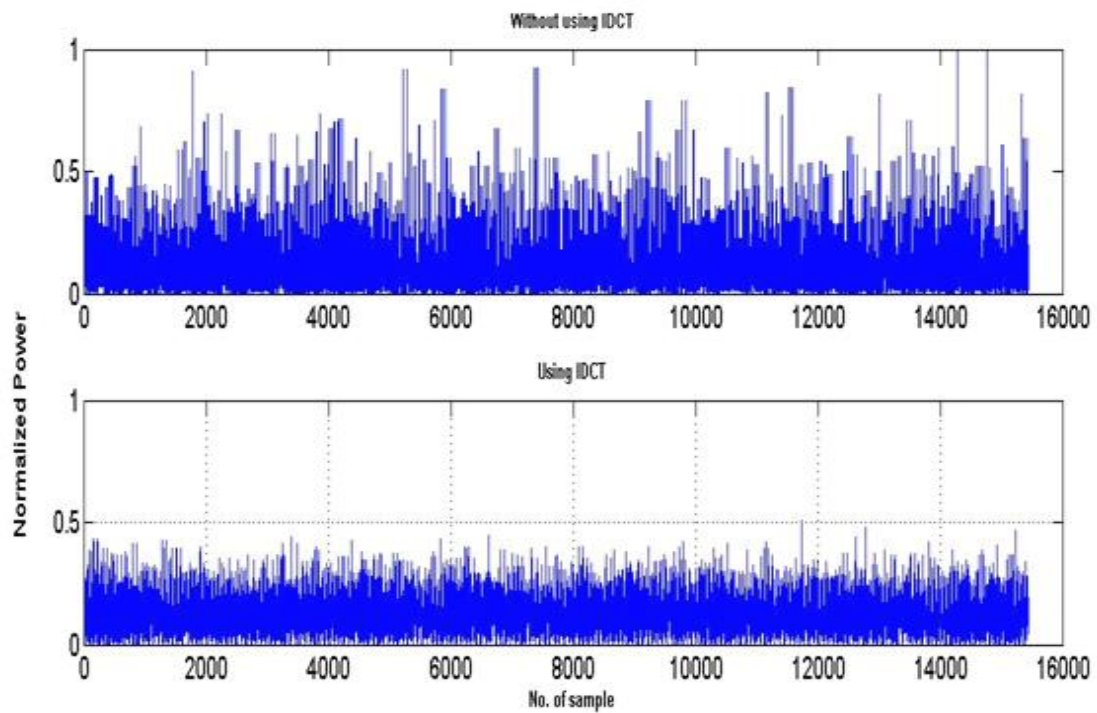


Figure(4).Inputs & outputs of IFFT in 802.11a system.

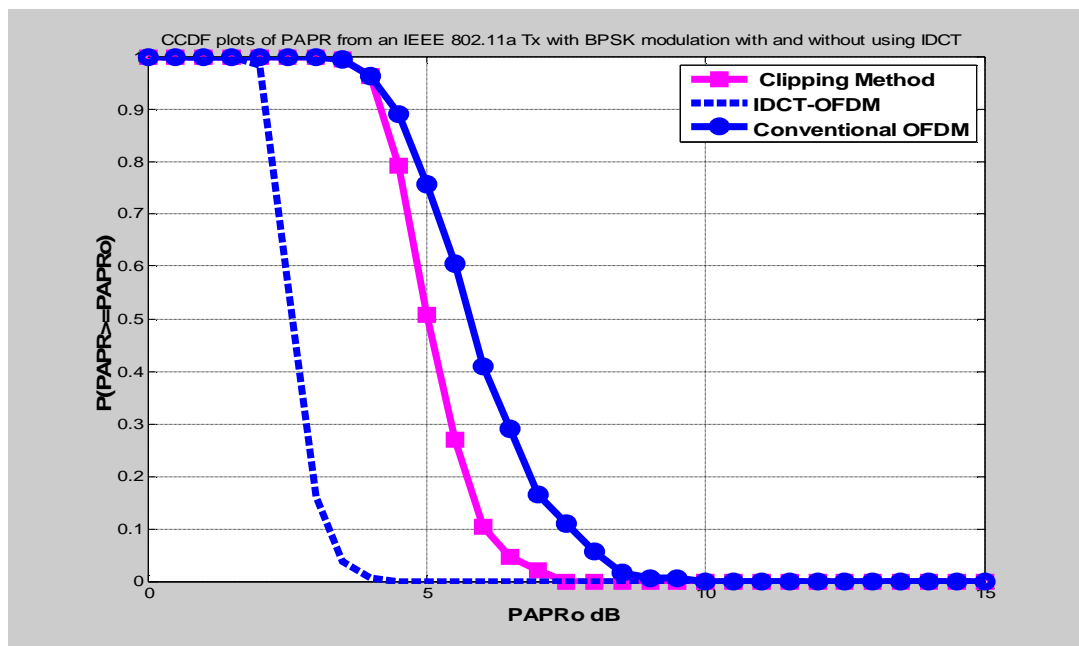
7. Results and discussion

Figure(5) shows the normalized output power of the proposed OFDM system with and without IDCT technique. From this figure, it is clear that IDCT reduces maximum power. This result because of IDCT rearranges power distribution of subcarriers.

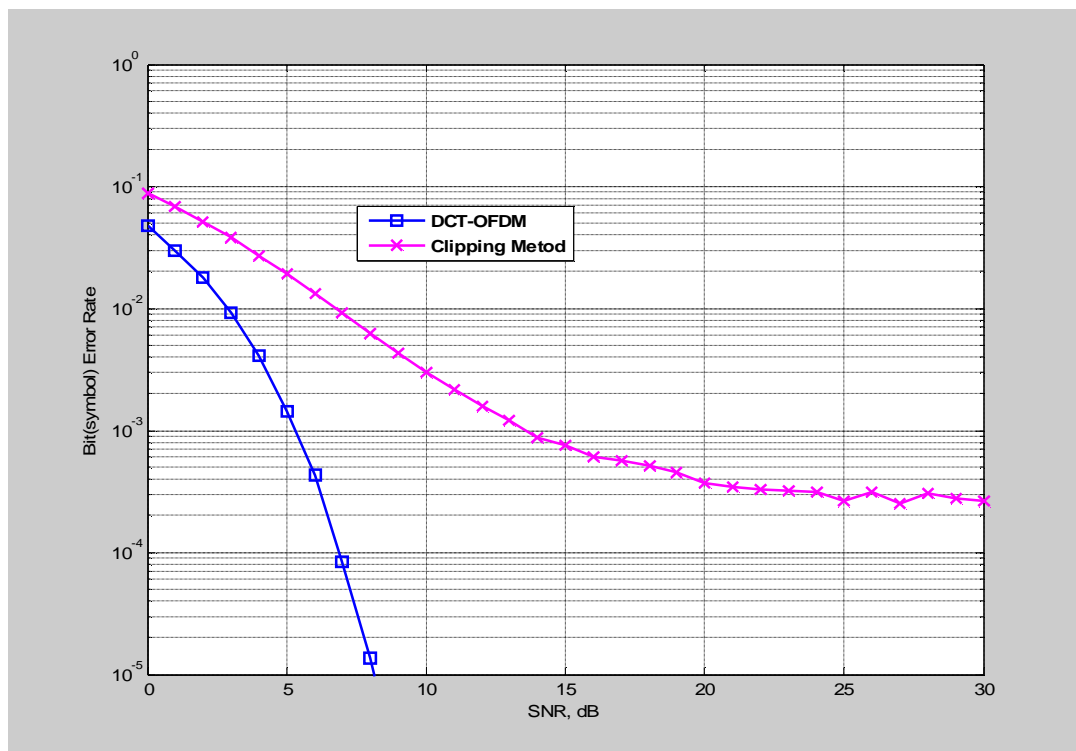
There are many methods to reduce the PAPR problem of OFDM system .Clipping method consider the easy method for reduction PAPR. We will compare PAPR performance of conventional OFDM , Clipping Method and IDCT-OFDM. The best way to compare these techniques is Complementary Cumulative Distribution Function CCDF as shown Figure(6). IDCT-OFDM exhibited more reduction in PAPR compare with Clipping method. The simulation parameters of Clipping method chosen to ensure that it gave similar BER performance of IDCT-OFDM in receiver side. From Figure(6),the PAPR of IDCT-OFDM systems can be reduced about 6dB compared with convention OFDM and about 3dB less than clipping methods.



Figure(5).Normalize power for OFDM with and without IDCT technique.



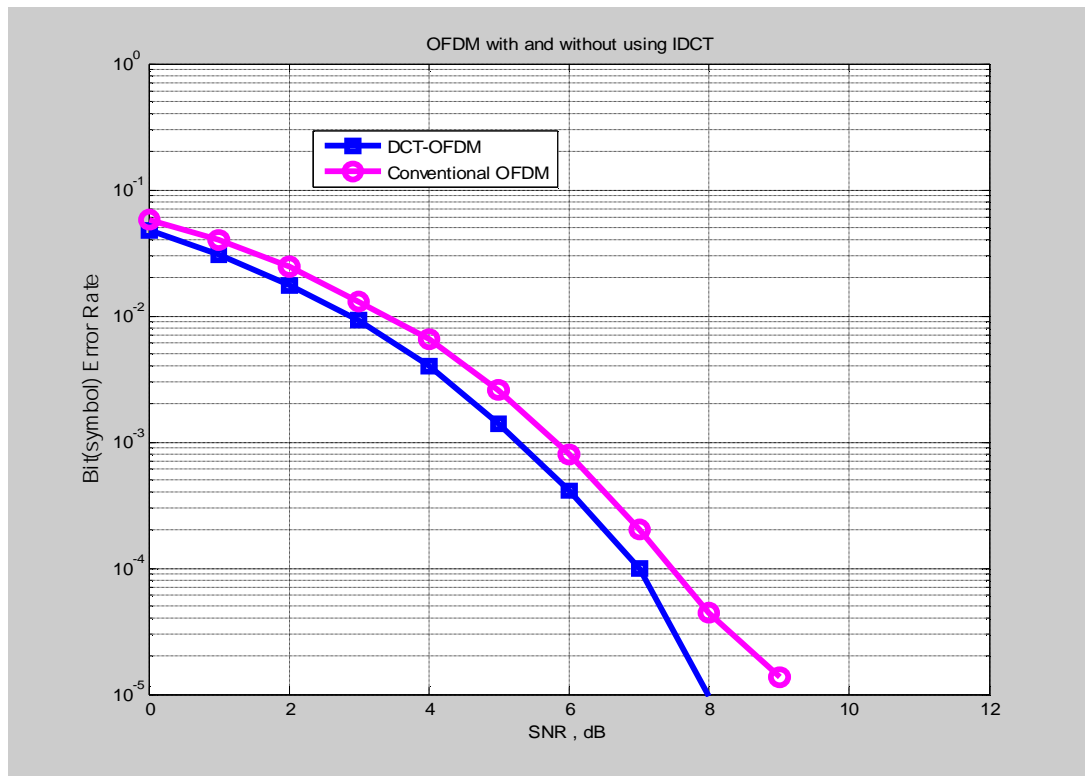
Figure(6).CCDF Comparison between clipping and IDCT.



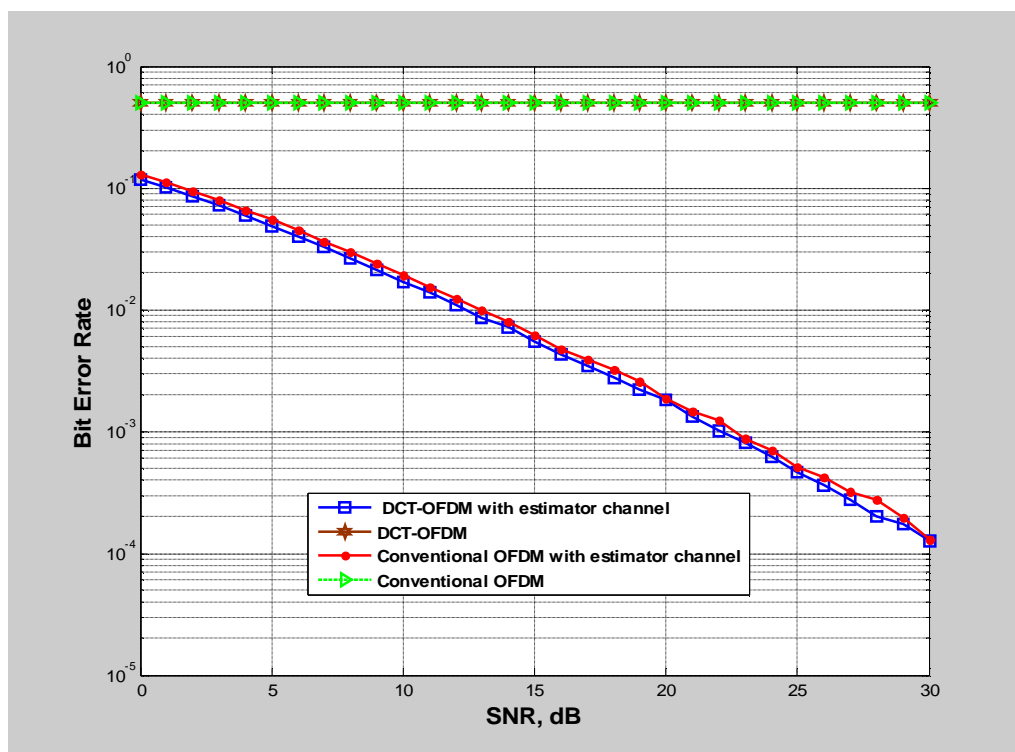
Figure(7).BER performance for IDCT and clipping method.

Figure (7) shows the BER performance for IDCT and Clipping method when the CCDF of clipping method is similar to CCDF of IDCT-OFDM method. The similarity can be achieved when the power threshold is change for suitable value where $PAPR_o$ don't exceed 4dB. The BER in Figure(7) was under AWGN channel environments. The limitation of Clipping method because of Clipping causes distorting the OFDM signal. IDCT technique exhibited good performance toward reduction PAPR in transmitter side and decreasing Bit Error Rate (BER) in receiver side about 1dB less than conventional OFDM as shown Figure (8). This results because of de-noising property of IDCT[20].

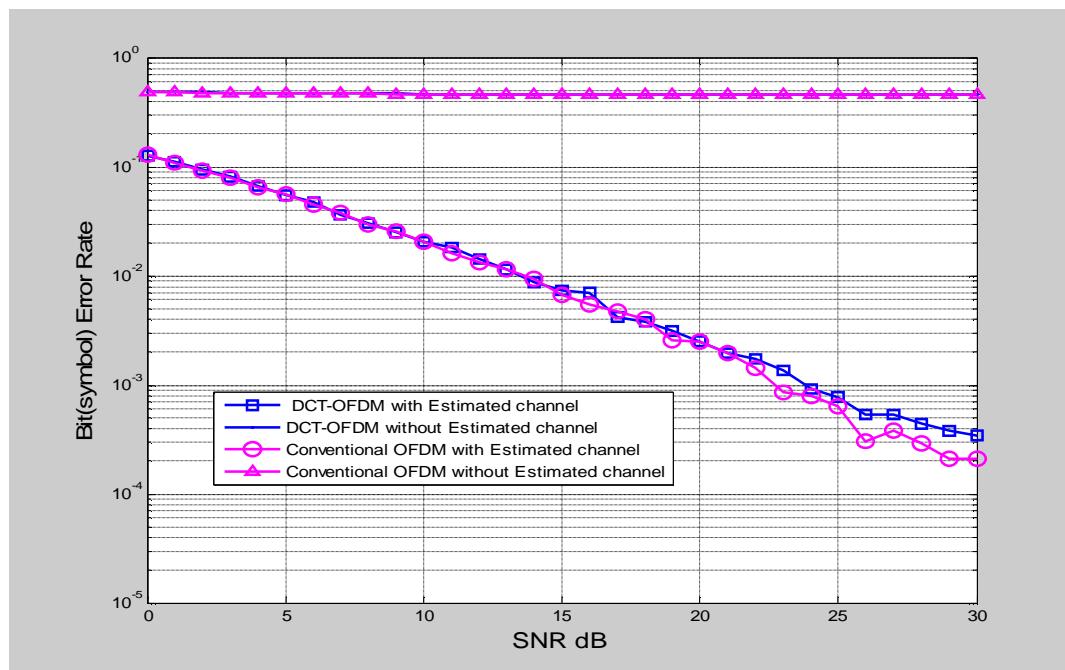
Figure(9) and Figure(10) show the BER performance of OFDM system with and without using IDCT under static flat fading and selective (2-Taps) noisy channel. It is important to see that, without channel estimation, data cannot be recovered. IDCT method has no effect on BER performance compared with conventional OFDM because of the output coefficients of IDCT orthogonal and the properties of IDCT it seemed similar to properties of FFT in ordinary OFDM.



Figure(8).BER performance of OFDM with and without IDCT in AWGN channel.



Figure(9). Performance of OFDM with and without using IDCT under Rayleigh flat fading(single-tap) noisy channel.



Figure(10). Performance of OFDM with and without using IDCT under Rayleigh selective fading(2-Taps) noisy channel.

8. Conclusions

Inverse Discrete Cosine Transform IDCT cascaded after IFFT exhibited good results toward reducing PAPR with acceptable performance as compared with clipping method and conventional OFDM. These results because energy de-compaction property for IDCT in Tx side and denoising property for DCT in Rx side. The BER performance of DCT-OFDM likes the performance conventional OFDM under static flat and selective (2-Taps) fading noisy (AWGN) channel. DCT-OFDM technique is not needed to transmit side information and is simple hardware implementation (DCT blocks available as IC chip sets). For these reasons DCT-OFDM makes it more applicable.

9. References

- [1] H. Sari, G. Karam, and I. Jeanclaude, "Transmission techniques for digital terrestrial TV broadcasting", IEEE Communication Mag., Vol.33, PP.100-109, Feb.1995.
- [2] J. chow, J. Tu, and J. cioffi, "A discrete multitone transceiver system for HDSL applications", "IEEE J. Select. Areas Commun.,Vol.9,PP.895-908,Aug. 1991.
- [3] R. Van Nee, G. Awater, M. Morikura, H. Takanashi, M. Webster, and K.W. Halford, "New high rate wireless LAN standards", "IEEE Commun. Mag., PP.82-88, Dec.1999.
- [4] C. Eklund, R.B. Marks,K. L. Stanwood, and S. Wang, "IEEE standard 802.16:A technical over view of the wireless access", "IEEE Commun. Mag., PP. 98-107,June 2002.

- [5] W. Lu, "4G mobile research in Asia, "IEEE Commun.Mag.,PP.104-106, Mar. 2003.
- [6] Saul, A., "Analysis of peak reduction in OFDM systems based on recursive clipping", M Proc. Of Int. OFDM workshop,Vol.1,Hamburg,Germany,Sept.24-25,2003.
- [7] X. Li and L. J. Cimini, Jr., "Effect of clipping and filtering on the performance of OFDM," IEEE Commun. Lett., vol. 2, no. 5, pp.131-133, May 1998.
- [8] N. Carson and T. A. Gulliver, "Performance of OFDM with modified RAS codes and clipping," IEEE Commun. Lett., vol. 7, pp. 440–442, Sept.2003.
- [9] S. Krongold and D. L. Jones, "PAR reduction in OFDM via active constellation extension," IEEE Trans. Broadcast., vol. 49, no. 3, pp. 258-268, Sep. 2003.
- [10]S. H. Muller and J. B. Huber, "OFDM with reduced peak-to-average power ratio by optimum combination of partial transmit sequences, "Elect. Lett., vol. 33, no. 5, pp. 368-369, Feb. 1997.
- [11]R. W. Bauml, R. F. H. Fisher, and J. B. Huber, "Reducing the peak-to-average power ratio of multicarrier modulation by selected mapping," Elect. Lett., vol. 32, no. 22, pp. 2056-2057, Oct. 1996.
- [12]L. Valbonesi and R. Ansari, "Frame-based approach for peak-to-average power ratio reduction in OFDM," IEEE Trans. Commun., vol. 54, no. 9, pp. 1604-1613, Sep. 2006.
- [13]D. S. Jayalath and C. Tellambura, "Reducing the peak-to-average power ratio of orthogonal frequency division multiplexing signal through bit or symbol interleaving," Elect. Lett., vol. 36, no. 13, pp. 1161-1163, June 2000.
- [14]K. R. Roo and P. Yip, "Discrete Cosine Transform-Algorithm advantages, Applications," academic Press, Inc. 1990.
- [15]Rohling, H.,et al., "Broad-band OFDM Radio Transmission for Multimedia Applications ",IEEE Proceedings,Vol.87, October,pp.1778-1788,1999.
- [16]Jayalath, A. D. S., "OFDM for wireless broadband Communications(Peak Power Reduction, Spectrum and Coding)", Ph.D. thesis, Monash University, Clayton, VIC 3800,Australia,2002.
- [17]Van Nee R. J. ,and Prasard R., "OFDM for Wireless Multimedia Communications", Artech House,Boston,1999.
- [18]Ochiai, H., "Analysis and Reduction of Peak to Average Power Ratio in OFDM system", PhD Thesis, The Graduate School of Engineering, The university of Tokyo, Japan, March, 2001.
- [19]G. Strang, "The Discrete Cosine Transform," *SIAM Review*, Volume 41, Number 1, pp.135-147, 1999.
- [20]L.P. Yaroslavsky, "Local Adaptive Image Restoration and Enhancement with the Use of DFT and DCT in a Running Window", Wavelet Applications in Signal and Image Processing IV, Eds.: M. A. Unser, A. Aldroubi, A.F. Laine, SPIE Vol. 2825, pp. 2-11, 1996.

High Performance PCC-DMT System Based on Hybrid Multi-Wavelet Functions

Hussein Abdel Mohicin Kazem

Electrical Department
College of Engineering
Thi-Qar University
hussien_elec@yahoo.com

Abstract

In this paper a scheme is proposed to improve the Bit Error Rate (BER) performance for Discrete Multi-Tone (DMT) system in wireless channel. The conventional DMT system is based on Fast Fourier Transform (FFT). The proposed system is based on Hybrid Multi-Wavelet Transform (HMWT). The HMWT is mixed between FFT and Multi-Wavelet Transform (MWT). The Inter-Carrier Interference (ICI) in DMT system due to Doppler spread is reduced by using Polynomial Cancellation Coding (PCC). Simulation results are done in three different types of channels: Additive White Gaussian Noise (AWGN) channel, flat fading channel and selective fading channel. The results show that the PCC-DMT system based on HMWT achieves better performance than the PCC-DMT system based on FFT and the PCC-DMT system based on MWT in all channels types.

Keywords: DMT, FFT, Multi-Wavelet Transform (MWT), Hybrid Multi-Wavelet Transform (HMWT), Polynomial Cancellation Coding (PCC).

منظومة PCC-DMT عالية الأداء المستندة على تهجين تحويل الموجة المتعدد

المستخلص

في هذا البحث تم اقتراح نظام لتحسين معدل الخطأ لمنظومة متعددة النغمات المنفصلة (DMT) في القناة اللاسلكية. أن نظام DMT الموجود يعتمد على تحويل فورير السريع (FFT). أما النظام المقترح يعتمد على تهجين تحويل الموجة المتعدد (HMWT). حيث أن تحويل الموجة المتعدد المهجن هو خليط بين FFT و تحويل الموجة المتعدد (MWT). كما أن تداخل النواقل في نظام DMT بسبب انتشار دوبلر تم تقليله باستخدام تقنية الغاء التشفير المتعدد (PCC). أن نتائج المحاكاة نفذت على ثلاثة أنواع من قنوات الاتصال: قناة الإرسال ذات الضوضاء جاوزية الشكل (AWGN) وقناة الإرسال ذات تردد الأضعاف اللانقائي وقناة الإرسال ذات تردد الأضعاف الانتقائي. أن منظومة PCC-DMT المستندة على HMWT حققت أداء أفضل من منظومة PCC-DMT المستندة على FFT وكذلك منظومة DMT المستندة على تحويل الموجة المتعدد (MWT) وفي كل أنواع القنوات.

الكلمات الرئيسية: DMT، FFT، تحويل الموجة المتعدد (MWT)، تحويل الموجة المتعدد المجهن (HMWT)، إلغاء التشفير المتعدد (PCC).

1. Introduction

The major goal of modern communications is the development of a reliable high-speed wireless communication system that supports high user mobility. The next generation of wireless systems will require higher data quality than current cellular mobile radio systems and should provide higher bit rate services. In other words, the next generation of wireless systems are supposed to have better quality and coverage, be more powerful and bandwidth efficient, and deploy diverse environments [1]. The ever-increasing demand for wireless and multimedia applications such as video streaming keeps pushing future wireless local area network (WLAN) systems to support much higher data rates (100 MB/s up to 1 GB/s) at high link reliability and over greater distances. Next-generation wireless communication systems are focused on increasing the link throughput (bit rate), the network capacity, and the transmit range [2]. A multi-band orthogonal frequency division multiplexing (OFDM) ultra wideband system is being considered for the physical layer of the new IEEE wireless personal area network (WPAN) standard, IEEE 802.15.3a [3,4]. The standard is targeting high data transmission rates of 110 Mb/s over 10 m, 220 Mb/s over 4 m and 480 Mb/s over 1 m. The IEEE 802.15.3a transceivers will be used in portable devices, such as camcorders, and laptops, as well as in fixed devices, such as TVs and desktops. Therefore the link throughput (bit rate), the network capacity and bandwidth efficiency are very important issues to be addressed [5].

DMT is similar to OFDM, with the difference that DMT carries different numbers of bits on different subchannels. This signaling scheme leads to a better usage of the channel capacity [6]. DMT systems exploit the capabilities of orthogonal subcarriers to cope efficiently with narrowband interference, high frequency attenuations and multipath fading's with the help of simple equalization filters [7]. An important feature of DMT is the possibility to allocate the number of bits per subcarrier according to its corresponding signal-to-noise ratio (SNR), typically known as bit-loading [8]. To perform bit loading, the SNR of each sub-channel is estimated during the modem's training phase. Then, based on the measured SNR, the appropriate bit loading is assigned to that channel to maximize the modem's throughput [9].

The DMT system can be regarded as a filter bank in transmultiplexer configuration [10-12]. Typically, the filter banks used for this purpose are discrete Fourier transform (DFT)

filter banks which can be implemented efficiently with the FFT. The filters in these DFT filter banks provide poor separation between adjacent subchannels [13].

The block diagram of the DMT system is shown in Figure (1). The input data stream is grouped into quadrature amplitude modulation (QAM) sub-symbols. A complex-to-real (IFFT) used for modulation is performed to convert QAM subsymbols to real ones. Then the last samples of each real-valued data vector are copied and prefixed to the data vector then the parallel to serial converter (P/S) is done for this data. At the receiver, the channel outputs are converting from serial to parallel (S/P). After removing the samples corresponding to the cyclic prefix the FFT which acts as the demodulation operation [14, 15].

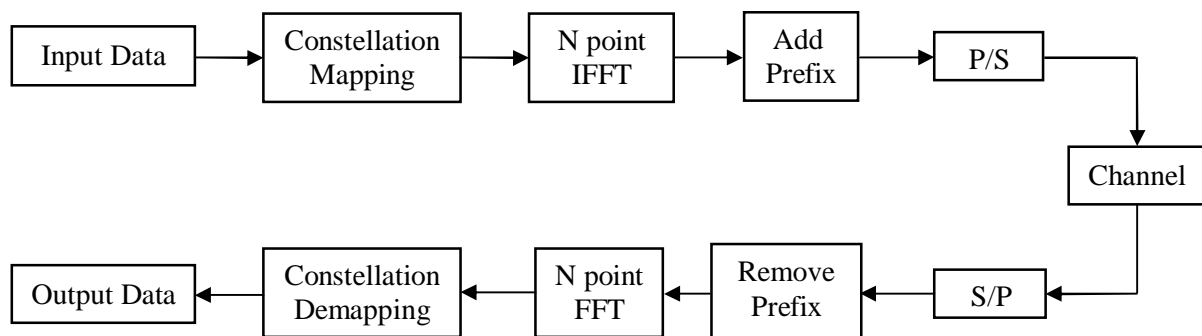


Figure (1). Block diagram of the DMT system.

Many researchers replaced the FFT with wavelet transform (WT) to improve the BER performance of the DMT system and this DMT is named discrete wavelet multitone (DWT). The main difference between ordinary FFT and WT is the FFT uses the sine and cosine as a basis functions but the WT uses the wavelet function and scaling function as a basis functions [16, 17].

2. Multi-Wavelet Transform (MWT)

The Multiwavelet (MWT) uses more than one scaling function and wavelet function. Multiwavelets have some advantages in comparison to scalar ones (ordinary wavelets that have been mentioned). For example, such features as short support, orthogonality, symmetry, and vanishing moments are known to be important in signal processing. A scalar wavelet can not possess all these properties at the same time. On the other hand, a multiwavelet system can

have all of these properties simultaneously. This suggests that multiwavelets could perform better in various applications [18].

For notational convenience, the set of scaling functions can be written using the vector notation $\Phi(t) = [f_1(t) \ f_2(t) \ \dots \ f_r(t)]^T$, where $\Phi(t)$ is called the multiscaling function. Likewise, the multiwavelet function is defined from the set of wavelet functions as $\Psi(t) = [y_1(t) \ y_2(t) \ \dots \ y_r(t)]^T$. When $r = 1$, $\Psi(t)$ is called a scalar wavelet, or simply wavelet. While in principle, r can be arbitrarily large, the multiwavelets up to date are primarily for $r = 2$ [19].

$$\Phi(2^j t) = \sum_k H_{j+1}(k) \Phi(2^{j+1} t - k) \quad (1)$$

$$\Phi(2^j t) = \sum_k G_{j+1}(k) \Phi(2^{j+1} t - k) \quad (2)$$

Note, however, that H_k and G_k are matrix filters, i.e. H_k and G_k are $r \times r$ matrices for each one. The matrix elements in these filters provide more degrees of freedom than a traditional scalar wavelet. These extra degrees of freedom can be used to incorporate useful properties into the multiwavelet filters, as mentioned before. However, the multi-channel nature of multiwavelets also means that the subband structure resulting from passing a signal through a multifilter bank is different. The two-scale Eqs.(1) and (2) can be realized as a matrix filter bank (as shown in Figure (2)) operating on r input data streams and filtering them into $2r$ output data streams, each of which is down-sampled by a factor of two.

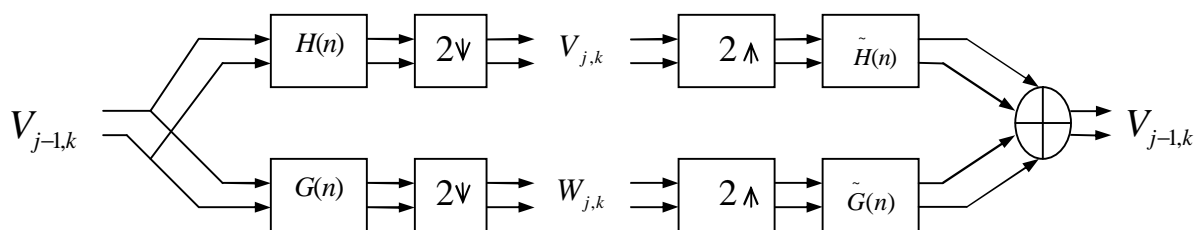


Figure (2). Analysis and Synthesis of a single level DMWT.

In the scalar-valued expression $v_{j,k}^l$, where j refers to the scale, k refers to the translation, and l refers to the sub-channel or vector row. It should be mentioned that the term discrete MWT (DMWT) is the same as MWT since the processing here is in discrete form always.

The multiwavelet have many types and this work deals with a GHM-type constructed by Geronimo, Hardian and Massopust for their smoothing compared with other types of MWT. Where H_k for GHM system are four scaling matrices H_0 , H_1 , H_2 , and H_3 [20]:

$$H_0 = \begin{bmatrix} \frac{3}{5\sqrt{2}} & \frac{4}{5} \\ \frac{1}{20} & -\frac{3}{10\sqrt{2}} \end{bmatrix}, H_1 = \begin{bmatrix} \frac{3}{5\sqrt{2}} & 0 \\ \frac{9}{20} & \frac{1}{\sqrt{2}} \end{bmatrix}, H_2 = \begin{bmatrix} 0 & 0 \\ \frac{9}{20} & -\frac{3}{10\sqrt{2}} \end{bmatrix}, H_3 = \begin{bmatrix} 0 & 0 \\ -\frac{1}{20} & 0 \end{bmatrix} \quad (3)$$

and four wavelet matrices G_0, G_1, G_2 , and G_3 :

$$G_0 = \begin{bmatrix} -\frac{1}{20} & -\frac{3}{10\sqrt{2}} \\ \frac{1}{10\sqrt{2}} & \frac{3}{10} \end{bmatrix}, G_1 = \begin{bmatrix} \frac{9}{20} & -\frac{1}{\sqrt{2}} \\ -\frac{1}{10\sqrt{2}} & 0 \end{bmatrix}, G_2 = \begin{bmatrix} \frac{9}{20} & -\frac{3}{10\sqrt{2}} \\ \frac{9}{10\sqrt{2}} & -\frac{3}{10} \end{bmatrix}, G_3 = \begin{bmatrix} -\frac{1}{20} & 0 \\ -\frac{1}{10\sqrt{2}} & 0 \end{bmatrix} \quad (4)$$

2.1 Preprocessing

The low pass filter H and high pass filter G consist of coefficients corresponding to the dilation Eq.(1) and wavelet Eq.(2). But, in the multiwavelet setting these coefficients are r by r matrices, and during the convolution step they must multiply vectors (instead of scalars). This means that multifilter banks need r input rows. Here $r = 2$ and two data streams will be used as inputs to the multifilter. An Over-Sampling Scheme (repeated row) will be used because its convenient to the case of one-dimensional signal [19], where the input length 2 vectors are formed from the original signal as

$$v_{o,k} = \begin{bmatrix} v_{0,k}^0 \\ v_{0,k}^1 \end{bmatrix} = \begin{bmatrix} X_k \\ a X_k \end{bmatrix} \quad k = 0, 1, \dots, N-1 \quad (5)$$

For the GHM case $a = 1/\sqrt{2}$, where a is the preprocessing factor.

3. Polynomial Cancellation Coding (PCC)

Polynomial cancellation coding (PCC) is a coding method in which the information to be transmitted is modulated onto weighted groups of subcarriers rather than onto individual subcarriers.

In Ref. [21] an OFDM system is designed with PCC where the high-speed data to be transmitted is divided into n lower speed parallel channels. The data in the k^{th} parallel channel in the i^{th} symbol period is represented by $d_{k,i}$. This will in general be a complex value. The data values $d_{0,i} \dots d_{n-1,i}$ determine the values $a_{0,i} \dots a_{N-1,i}$ which modulate the N subcarriers in the i^{th} symbol period. For normal OFDM $n = N$, and $a_{k,i} = d_{k,i}$; one data value is used to modulate each subcarrier. With PCC, the data to be transmitted is mapped onto weighted groups of subcarriers. For example, to apply PCC to pairs of subcarriers, the subcarriers in

each pair must have relative weightings +1 and -1. In this case $n = N/2$. The first data value in each symbol period is used to modulate the first two subcarriers: $a_{0,i} = d_{0,i}$, $a_{1,i} = -d_{0,i}$.

The demodulated subcarriers are then weighted and added to generate the data estimates $v_{0,i} \dots v_{n-1,i}$. For a pair of PCC-OFDM subcarriers $z_{2M,i}$, $z_{2M+1,i}$ an estimate is calculated using $v_{M,i} (z_{2M,i} - z_{2M+1,i})/2$ [22].

4. Proposed PCC-DMT system based on HMWT

The HMWT is a combination between FFT and MWT and therefore it has all the advantages of the FFT and MWT. Since the MWT is the same as WT but with two wavelet functions and two scaling functions and that leads to enhance the BER performance of DMT system in AWGN flat faded channel. In selective fading channel, the MWT gives worse BER performance in comparison to FFT since the BER is constant at certain signal to noise ratio (SNR) and gives a straight line but that does not happen in FFT and therefore the FFT will increase the orthogonality of MWT filters in HMWT.

The procedure steps to obtain on HMWT are:

Step 1: Apply the two dimensional FFT on each scaling matrix H and wavelet matrix G given in Eqs.(1) and (2) respectively. Assume Y any matrix (scaling or wavelet), then the two dimensional FFT for this matrix can be denoted by Z as:

$$Z(k_1, k_2) = \sum_{r=1}^N \sum_{s=1}^M Y(r, s) e^{-\frac{2\pi i}{N}(r-1)(k_1-1)} e^{-\frac{2\pi i}{M}(s-1)(k_2-1)} \quad (6)$$

where N is the number of elements in each row and M is the number of elements in each column (here $N=M=2$) and $k_1 = k_2 = 1, 2$.

Step 2: Multiply the Z matrix which is calculated from *step 1* with itself for two times by using corresponding elements multiplication method as shown in the following steps:

a) Change the dimensions of the Z matrix from 2×2 to 4×4 as shown:

$$Z = \begin{bmatrix} z_{11} & z_{12} \\ z_{21} & z_{22} \end{bmatrix} \Rightarrow Z = \begin{bmatrix} z_{11} & 0 & 0 & 0 \\ 0 & z_{12} & 0 & 0 \\ 0 & 0 & z_{21} & 0 \\ 0 & 0 & 0 & z_{22} \end{bmatrix} \quad (7)$$

b) Multiply the Z matrix in Eq.(7) by itself for two times, and assume F is the result of multiplication, then:

$$F = Z * Z * Z$$

$$F = \begin{bmatrix} z_{11}^3 & 0 & 0 & 0 \\ 0 & z_{12}^3 & 0 & 0 \\ 0 & 0 & z_{21}^3 & 0 \\ 0 & 0 & 0 & z_{22}^3 \end{bmatrix} \quad (8)$$

c) Change the dimensions of the F matrix in Eq.(8) from $4*4$ to $2*2$ as shown:

$$F = \begin{bmatrix} f_{11} & 0 & 0 & 0 \\ 0 & f_{12} & 0 & 0 \\ 0 & 0 & f_{21} & 0 \\ 0 & 0 & 0 & f_{22} \end{bmatrix} \Rightarrow F = \begin{bmatrix} f_{11} & f_{12} \\ f_{21} & f_{22} \end{bmatrix} \quad (9)$$

Where $f_{ij} = z_{ij}^3$ for $i=j=1, 2$.

Step 3: Apply the two dimensional IFFT on the matrix F in Eq.(9). Assume \tilde{F} is the two dimensional IFFT for matrix F and calculate using Eq.(10):

$$\tilde{F}(r, s) = \frac{1}{NM} \sum_{k_1=1}^N \sum_{k_2=1}^M F(k_1, k_2) e^{\frac{2\pi i}{N}(r-1)(k_1-1)} e^{\frac{2\pi i}{M}(s-1)(k_2-1)} \quad (10)$$

Applying the steps 1-3 on all scaling matrices H and wavelet matrices G to obtain new GHM multifilter bank. Assuming the hybrid four scaling matrices that corresponding to GHM system are A_0, A_1, A_2 , and A_3 then:

$$A_0 = \begin{bmatrix} 1.0023 & 1.0850 \\ -0.5619 & -0.6348 \end{bmatrix}, \quad A_1 = \begin{bmatrix} 0.9705 & 0.8100 \\ 1.0091 & 1.1650 \end{bmatrix}, \quad (11)$$

$$A_2 = \begin{bmatrix} 0 & 0 \\ 0.1519 & -0.1384 \end{bmatrix}, \quad A_3 = \begin{bmatrix} 0 & 0 \\ -0.1250 * 10^{-3} & 0 \end{bmatrix}$$

and hybrid four wavelet matrices B_0, B_1, B_2 , and B_3

$$B_0 = \begin{bmatrix} -0.0481 & -0.0780 \\ 0.0486 & 0.0788 \end{bmatrix}, \quad B_1 = \begin{bmatrix} 1.3129 & -1.6423 \\ -1.5989 & 1.2150 \end{bmatrix}, \quad (12)$$

$$B_2 = \begin{bmatrix} 1.0631 & -0.9689 \\ 1.0739 & -0.9788 \end{bmatrix}, \quad B_3 = \begin{bmatrix} -0.8750 * 10^{-3} & 0 \\ -0.8839 * 10^{-3} & 0 \end{bmatrix}$$

As in MWT the coefficients are r by r matrices, and during the convolution step they must multiply vectors (instead of scalars). This means that hybrid multifilter banks need two data streams and therefore a repeated row will be used. Because of the repeated row is formed input length 2 vectors from the original signal by dividing on a ; a is taken equal to -1 in the proposed system to perform the repeated row and PCC in the same time.

5. Simulation results

Matlab 2009a is used to compute the BER performance of the proposed system. The number of subcarriers taken (the number of FFT points) equals to 64. Three types of channels are used: The AWGN channel, AWGN with Raleigh flat fading channel and AWGN with Raleigh selective fading channel. The results show that the BER performance for proposed system in AWGN with Raleigh flat fading channel for different Doppler frequency shift (5 and 500) Hz. Also the results show that the BER performance for proposed system in AWGN with Raleigh selective fading channel for different Doppler frequencies shift (5, 100 and 500) Hz, path delay (1, 2 and 8) samples and attenuation of the second path gain (-8 and -11) dB. In all schemes, the uniform bit-loading across the subchannels with number of bits (b) = 64.

The BER performance for proposed system compared with different DMT systems based on FFT, MWT and HMWT. In DMT system that based on MWT or HMWT, $a = 1/\sqrt{2}$ but in PCC-DMT system that based on FFT, MWT or HMWT, $a = -1$.

5.1 Performance of the proposed system in AWGN channel

As shown in Figure (3) the gain at $\text{BER} = 10^{-3}$ is about 4.145 dB when using DMT system based on HMWT as compared with the DMT system based on MWT. The gain of DMT system based on HMWT is 22.584 dB as compared with the DMT system based on FFT. The gain for PCC-DMT system is about 0.5 over the DMT system without PCC and for all transforms.

5.2 Performance of the proposed system in flat fading channel

Figure(4) shows the BER performance for the proposed system in AWGN with Raleigh flat fading channel at Doppler frequency shift = 5 Hz. At $\text{BER} = 10^{-3}$, the gain is about 4.477 dB and 22.41 dB when using DMT based on HMWT system as compared with the DMT system based on MWT and the DMT system based on FFT respectively. The performance of proposed system is nearly the same performance of DMT system based on HMWT but it given gain about 3.683 dB and 21.81 dB as compared with itself when it's based on MWT and FFT respectively.

Figure(5) shows the BER performance for the proposed system in AWGN with Raleigh flat fading channel at Doppler frequency shift = 500 Hz. The gain between all

systems in this Figure is nearly the same gain that obtained in Figure(4). but the BER performance in Figure(4) is better than the BER performance in Figure(4). with gain about 4 dB for all systems.

5.3 Performance of the proposed system in selective fading channel

Figures(6) and (7) show the BER performance for the proposed system in AWGN with Raleigh selective fading channel at Doppler frequency shift = 5 Hz, path delay = 1 and 2 samples respectively and attenuation of the second path gain = -11 dB. In Figure(6), at $\text{BER} = 10^{-3}$, the gain is about 3.938 dB and 22.298 dB when using DMT based on HMWT system as compared with the DMT system based on MWT and the DMT system based on FFT respectively. The performance of PCC-DMT system based on HMWT is nearly the same performance of DMT system based on HMWT but the first system given gain about 3.566 dB and 22.01 dB as compared with itself but when it is based on MWT and FFT respectively. The gain between all systems in Figure(7). is nearly the same gain that obtained in Figure(6). but the BER performance in Figure(6). is better than the BER performance in Figure(7). because the path delay is increased from 1 sample to 2 samples.

Figures(9) and (10) show the BER performance for the proposed system in AWGN with Raleigh selective fading channel at Doppler frequency shift = 500 Hz, path delay = 1 and 2 samples respectively and attenuation of the second path gain = -11 dB. The gain between all systems in Figures(9) and (10) is nearly the same gain that obtained in Figures(6) and (7) but the BER performance in Figures (9) and (10) is increased due to increase the Doppler frequency shift to 500 Hz.

Figures (8) and (11) show the BER performance for the proposed system in AWGN with Raleigh selective fading channel at different Doppler frequency shift = 5 Hz and 500 Hz respectively ,path delay = 8 samples and attenuation of the second path gain = -8 dB. The gain between all systems in these figures is nearly the same gain that obtained in Figures(6) and (9) respectively but the BER performance in Figures(8) and (11) is not better than the BER performance in Figures (6) and (9) respectively because the attenuation of the second path gain is increased and that lead to decrease the BER performance.

6. Conclusions

In this paper a proposed transform HMWT is used based on both FFT and MWT. The reason of using the FFT for GHM multiwavelet filter banks is to increase the orthogonality of these filters where the orthogonality will increase on the rows and columns and that leads to more orthogonal filters. FFT were taken for each GHM filter bank then multiply the result with itself for three times to obtain best results as in wavelet transform when taken more level of decomposition that gives best results. The comparison between the BER performance for a proposed system and other systems is taken for three different types of channels. Simulation results of PCC-DMT system based on HMWT show a good SNR gain improvement compared with DMT system with and without PCC and either based on FFT or MWT.

Many techniques can be used as future work to increase system performance such as channel coding, channel equalization and using multi FFT.

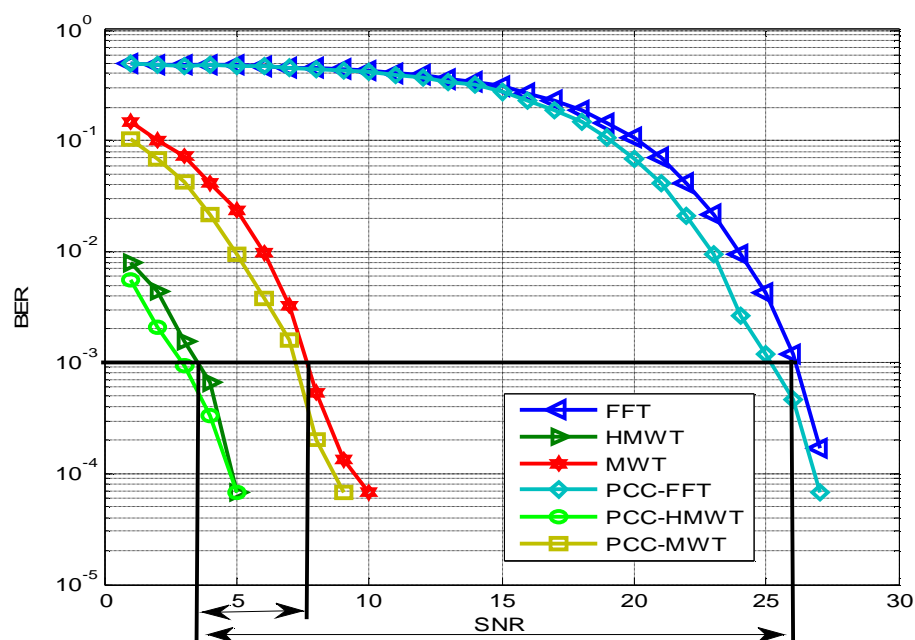
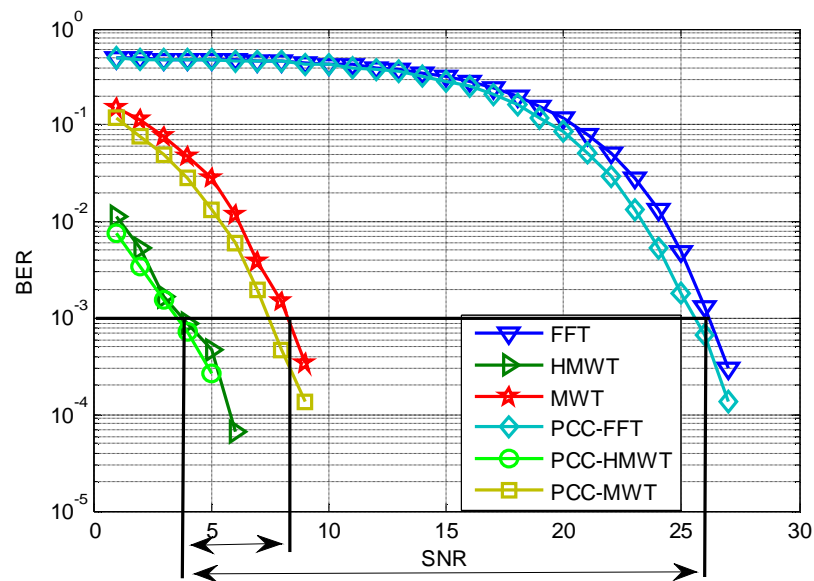
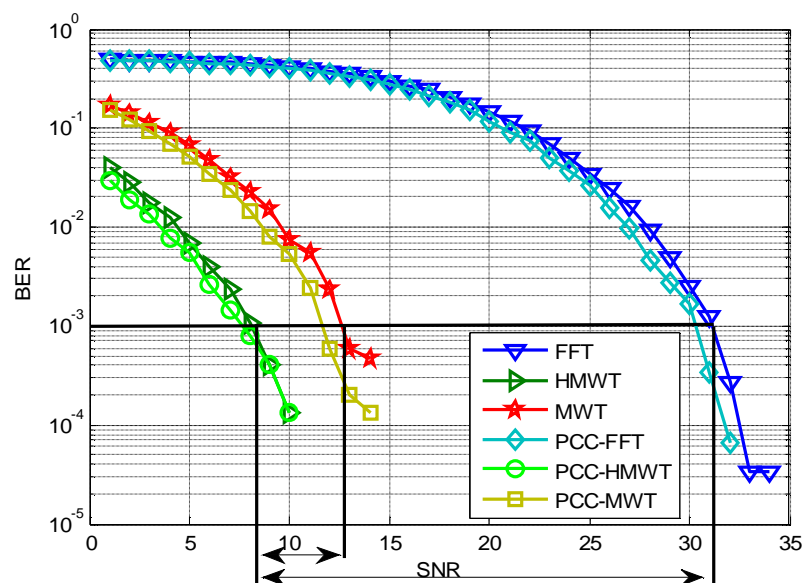


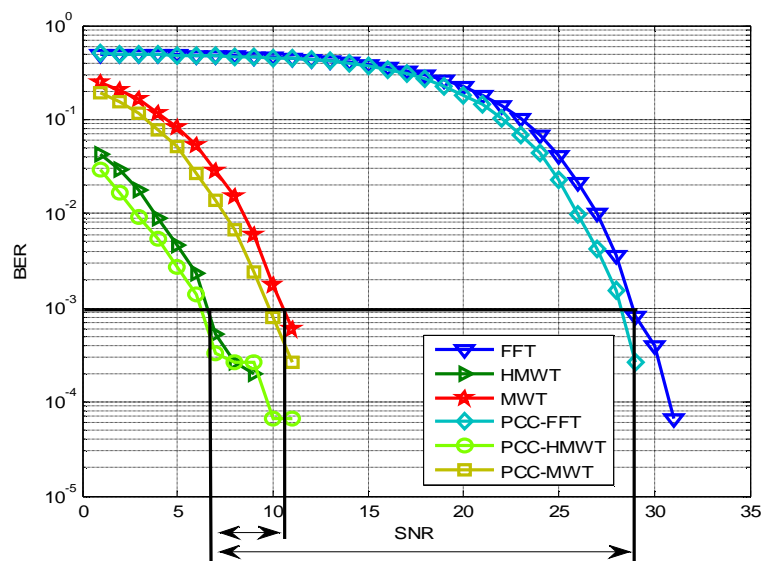
Figure (3). Performance of different types of multi-carrier system under AWGN channel.



Figure(4). Performance of different types of multi-carrier system under AWGN channel with flat fading channel at Doppler frequency shift = 5 Hz.



Figure(5). Performance of different types of multi-carrier system under AWGN channel with flat fading channel at Doppler frequency shift = 500 Hz.



Figure(6). Performance of different types of multi-carrier system under AWGN channel with selective fading channel at Doppler frequency shift = 5 Hz, path delay = 1 sample and attenuation of the second path gain = -11 dB.

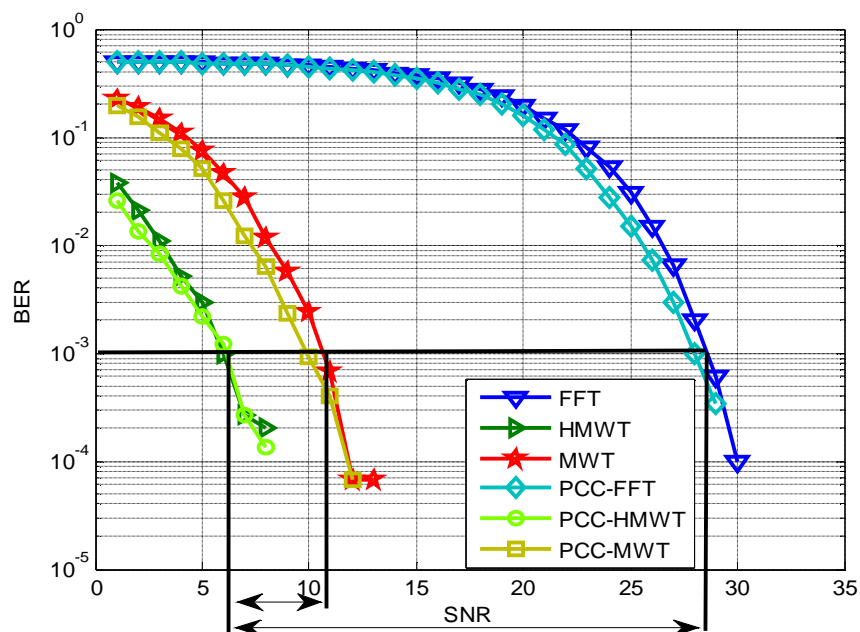


Figure (7). Performance of different types of multi-carrier system under AWGN channel with selective fading channel at Doppler frequency shift = 5 Hz, path delay = 2 samples and attenuation of the second path gain = -11 dB.

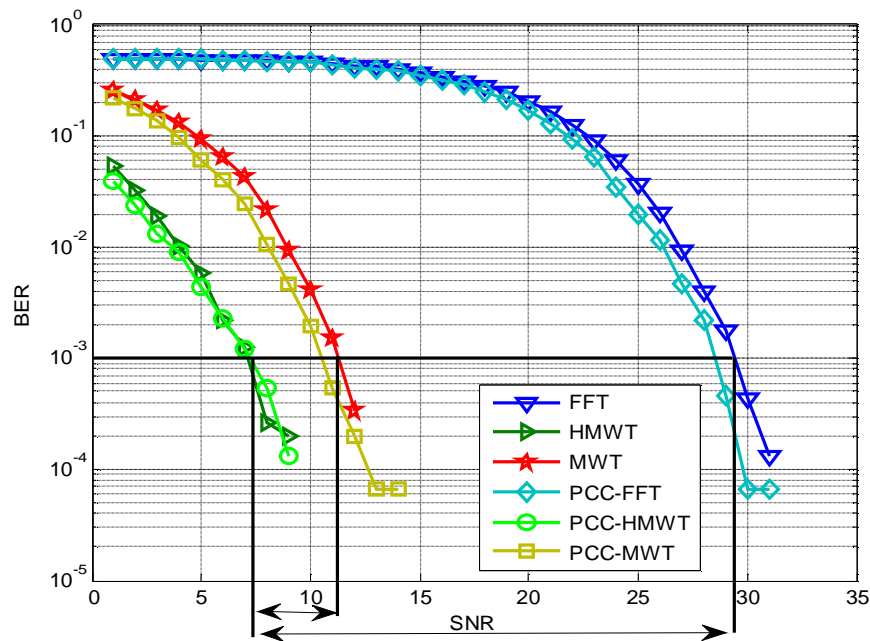


Figure (8). Performance of different types of multi-carrier system under AWGN channel with selective fading channel at Doppler frequency shift = 5 Hz, path delay = 8 samples and attenuation of the second path gain = -8 dB.

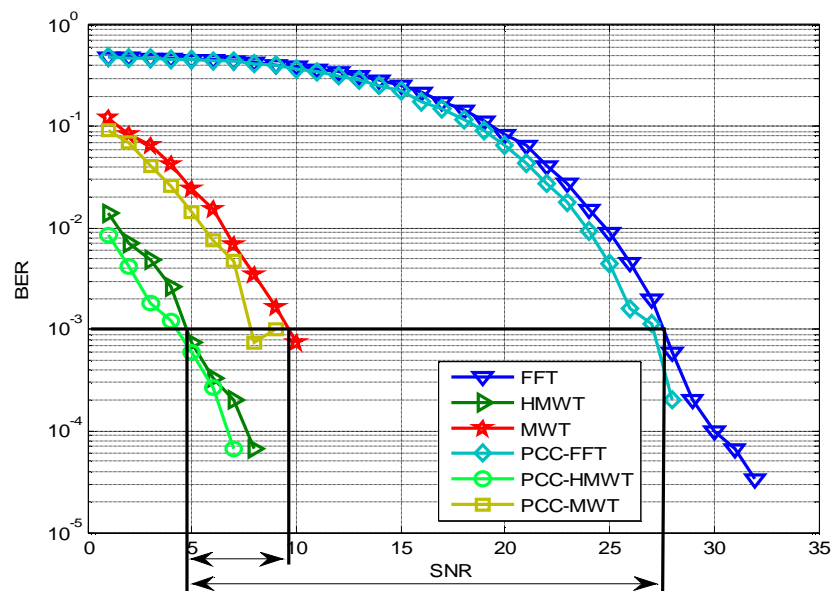


Figure (9). Performance of different types of multi-carrier system under AWGN channel with selective fading channel at Doppler frequency shift = 500 Hz, path delay = 1 sample and attenuation of the second path gain = -11 dB.

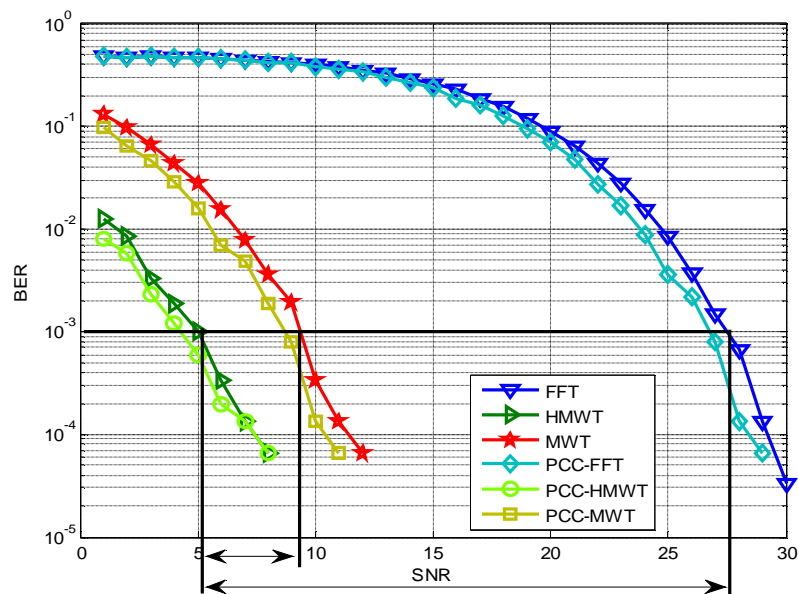


Figure (10). Performance of different types of multi-carrier system under AWGN channel with selective fading channel at Doppler frequency shift = 500 Hz, path delay = 2 samples and attenuation of the second path gain = -11 dB.

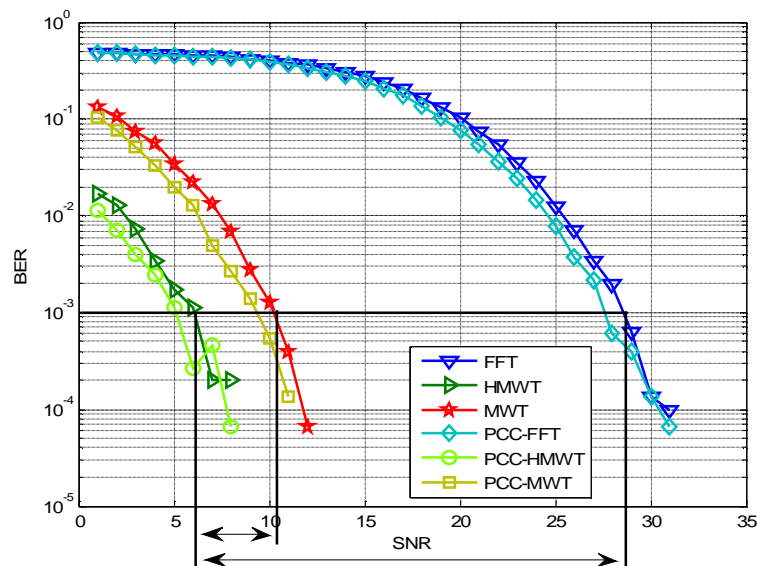


Figure (11). Performance of different types of multi-carrier system under AWGN channel with selective fading channel at Doppler frequency shift = 500 Hz, path delay = 8 samples and attenuation of the second path gain = -8 dB.

7. References

- [1] Alamouti, S.M., October 1998, "A Simple Transmit Diversity Technique for Wireless Communications" , IEEE J. Selected Area in Communication ,Vol. 16, No. 8, pp. 1451-1458.
- [2] Rahn, D.G., Cavin, M.S., Dai, F.F., Fong, N.H.W., Griffith, R., Macedo, J., Moore, A.D., Rogers, J.W.M., and Toner, M., 2005, "A Fully Integrated Multiband MIMO WLAN Transceiver RFIC" ,IEEE J. Solid-State Circuits ,Vol. 40 ,No. 8 ,pp. 1629-1641.
- [3] Foerster, J., 2003, "Channel Modeling Sub-Committee Report Final" ,Technical report ,IEEE802.1502/490.
- [4] Balakrishnan, J., Batra, A., and Dabak, A., 2003, "A Multi-Band OFDM System for UWB Communication" ,in: IEEE Conference on Ultra Wideband Systems and Technologies ,University of British Columbia ,Vancouver ,Canada ,pp. 354-358.
- [5] Shin, O.S., Chan, A.M., Kung, H.T., and Tarokh, V., July 2007, "Design of an OFDM Cooperative Space-Time Diversity System" ,IEEE Trans. Vehic. Technol ,Vol. 56 ,No. 4, pp. 2203-2215.
- [6] Bengtsson, D., and Landström, D., 21 February 1996, "Coding in a Discrete Multitone Modulation System" , M.Sc. Thesis ,Luleå University of Technology ,Sweden.
- [7] Muhammad, F.S., Baudais, J.Y., Helard, J.F., and Crussiere, M., April 2008, "Coded Adaptive Linear Precoded Discrete Multitone Over PLC Channel" ,IS-PLC'08.
- [8] Lee, S.C.J., Breyer, F., Randel, S., Cárdenas, D., Boom, H.P.A., and Koonen, A.M.J., 17 June 2009, "Discrete Multitone Modulation for High-Speed Data Transmission Over Multimode Fibers using 850-nm VCSEL" ,IEEE standard ,Eindhoven University of Technology.
- [9] Mireles, F.R., Aldrubi, Q., Heidari, S., and Sevalia, P., 11 October 2002, "The Benefits of Discrete Multi-Tone (DMT) Modulation for VDSL Systems" ,Version 1.4, available at <http://www.analogzone.com/nett0722.pdf>
- [10] Akansu, A.N., Duhamel, P., Lin, X., and Courville, M.D., April 1998, "Orthogonal Transmultiplexers in Communications: A review" ,IEEE Trans. Signal Processing ,Vol. 46 , No. 4 , pp. 979-995.
- [11] Vaidyanathan , P.P. , 1993, "Multirate Systems and Filter Banks" ,Englewood Cliffs, NJ: Prentice-Hall.

- [12] Vandendorpe, L., Cuvelier, L., Deryck, F., Louveaux, J., and Wiel, O.V., April 1998, "Fractionally Spaced Linear and Decision Feedback Detectors for Transmultiplexers" ,IEEE Trans. Signal Processing ,Vol. 46 ,No. 4 ,pp. 996-1011.
- [13] Rizos, A.D., Proakis, J.G., and Nguyen, T.Q., November 1994, "Comparison of DFT and Cosine Modulated Filter Banks in Multicarrier Modulation", In Processing of Globe communication, pp. 687-691.
- [14] Vanbleu, K., Ysebaert, G., Cuypers, G., Moonen, M., and Acker, K.V., June 2004, " Bitrate-Maximizing Time-Domain Equalizer Design for DMT-Based Systems" ,IEEE Transactions Communications, Vol. 52, No. 6, pp. 871-876.
- [15] Wang, B., and Adali, T., 2000, " Time-Domain Equalizer Design for Discrete MultiTone Systems" ,University of Maryland ,Baltimore County ,pp. 1080-1084.
- [16] Tzannes, M.A., April 1993, "System Design Issues for the DMWT Transceiver" ,ANSI Standard Committee T1E1.4, pp.93-100.
- [17] Mustafa, S. A., and Hikmat, V. E., 2009, " Performance Evaluation of DWMT Downlink Scheme over UTP-3 Cable" ,Faculty of Electrical Engineering ,University Teknologi Malaysial ,Vol. 11 ,No. 2 ,pp. 20-26.
- [18] Strela, V., June 1996, "Multiwavelets: Theory and Applications" ,Ph.D. Thesis ,Massachusetts Institute of Technology ,Cambridge.
- [19] Al-Taai, H.N., "Optical Flow Estimation Using DSP Techniques" ,Ph.D Thesis, University of Technology, Iraq, April 2005.
- [20] Strela, V., and Walden, A.T., 1998, "Orthogonal and Biorthogonal Multiwavelets for Signal Denoising and Image Compression" ,Proc.SPIE ,Vol. 3391 ,pp107-96.
- [21] Armstrong, J., Grant, P.M., and Povey, G., Novmber 1998, "Polynomial Cancellation Coding of OFDM to Reduce Intercarrier Interference Due to Doppler Spread" ,In Proc. of IEEE GLOBECOM 98 ,Sydney ,Australia ,pp. 2771-2776.
- [22] Sentu, J., and Armstrong, J., June 2003, "Effects of Phase Noise on the Performance of PCC-OFDM Systems" ,IEEE Trans. Broadcast ,Vol. 49 ,pp. 221-224.

Kinematic Analysis of Bicycle Pedaling

Haider J. Abed

Mechanical Engineering Department

College of Engineering

Thi-Qar University

haider_jabaur@yahoo.com

Abstract

In this study, the kinematic equations are derived to describe the angles, velocities, and accelerations of the leg of bike rider when changing the height and angle of seat tube. These equations are useful to get the optimum seat position, (in separated study), for best performance and efficiency.

The pedaling motion model was simulated as four-bar mechanism (the foot was not considered), and by using polar form of complex number notation to get the kinematic equations. These equations are agreed with MATLAB/Simulink/SimMechanics/Four-Bar Model, as well as, the graphical method. The derived equations (kinematic equations) can describe the crossed and open four-bar mechanism.

Key Words: Bike Fit, Pedaling , Kinematic Equations, Four-Bar Mechanism.

المستخلص

في هذا البحث تم اشتقاق معادلات الزوايا و السرعة والتعجيل لحركة ساق راكب الدراجة نسبة إلى حركة الدواسة في حالة تغيير ارتفاع وزاوية المقعد, وذلك لإيجاد, (في بحث منفصل), الموقع المثالي للمقعد للحصول على أفضل أداء و اقل جهد على السائق. ومثلت حركة الساق مع الدواسة بميكانيكية التراكيب الأربعة (four-bar mechanism) حيث تم إهمال دور القدم.

باستخدام المحاور القطبية للإعداد المركبة تم الحصول على المعادلات الحركية حيث قورنت وبنجاح مع برنامج المحاكاة المتوفر في برنامج الماتلاب (MATLAB/SIMULINK), إضافة إلى طريقة الرسم التقليدية (Graphical Method). والمعادلات الحركية الكينماتيكية تصف ميكانيكية التراكيب الأربعة للتراكيب المتقاطعة والتراكيب المفتوحة (Crossed and Open four-bar mechanism).

1. Introduction

Correct body position on the bike (i.e. equipment configuration, seat tube angle, correct seat height and the foot placement on the pedal) are all interrelated and are collectively known as the bike fit. For this reason, the bike fit has the outcome of proper muscle recruitment, achievable pedaling rate, power and ultimately maximum pedaling efficiency[1]. Where the pedaling efficiency is the difference between the human power expended and the actual power delivered to the road. The maximum efficiency can be attained through training of proper pedaling technique and also through a proper bike fit to maximize joint angles of individual [2].

The bike fit adjusts the angles of the 'lever' of the hip, knee and ankle joints as they relate to the foot-to-pedal interface to achieve the overall performance objective. An improper bike fit will result in reduced efficiency through less than optimal muscle recruitment (improper angles of the levers and potentially, in serious cases, injuries could result from an improper bike fit). Finally, the bike fit must always begin with the individual assessment (i.e. goals, fitness level, biking experience, flexibility, body measurement) then adjust/fit bicycle to the individual, being sure not to make the common mistake of fitting the individual to the bicycle[3]. Following is a list of bike fit adjustment/ variables [4]:

- 1- Seat tube angle-correct hip lever angle.
- 2- Seat height-achieve optimal performance height and angle of hip lever.
- 3- Seat position fore/aft-get knee directly over pedal and correct knee lever angle.
- 4- Adjustment of shoe cleats-correct knee and ankle lever angle.
- 5- Handle bar height, reach and size-maximize hip flexor/extender angle. Correct back and shoulder positioning for comfort and aerodynamics.
- 6- Foot placement on pedal-correct ankle lever angle at the man/machine interface.
- 7- Crank arm length- needs to be optimum length for cycling purpose.
- 8- Power meter technology to assess bike fit- technology of power meters uses biomechanical technology to assess and improve power and thus performance.

The motion of cycling as if it were the face of clock, beginning at approximately the 11 o'clock position[3]:

- | | |
|--------------------------|-------------------|
| 1- Preparatory phase: | 11:00 to 1:00, |
| 2- Power phase: | 1:00 to 5:00, |
| 3- Follow through phase: | 5:00 to 7:00, and |
| 4- Recovery phase: | 7:00 to 11:00. |

The Preparatory Phase: prepares the leg and foot for the power phase. This phase begins with the knee in its most flexed position, ready for the push through into the movement phase. The ankle will tend to go from a slightly plantar flexed position at 11:00 to a nearly neutral at the 1:00 position.

The Power Phase: during the power phase, hip and knee extension continue, the most effective force applied is that one which is perpendicular to the crank clearly, the 3:00 position is the peak of the movement phase (when the seat position above the pedal axis). During this phase, particularly in the lower part of the movement phase knee extension is also occurring.

The Follow Through Phase: as the pedaling foot is moving from 5:00 to 7:00 in follow through, both feet are in the least effective position to produce power. The joint action here is knee flexion, with some slight hip extension and flexion as the foot moves through the bottom of the circle and begins upward travel and the ankle joint will begin a slight plantar-flexion, helping to keep applied force as nearly tangential as possible.

Recovery: the primary joint movement at the hip is flexion. Some of the energy expended by the leg in the power phase will be wasted and used to help push the recovering leg up to the top of its phase, where knee is flexion and the ankle joint will continue to be slightly plantar-flexed beginning to move slightly toward neutral. A viewing the motion of pedaling a bicycle can be simplified by considering only one leg at a time while the opposite leg will be doing the exact same motions, only in 180 degree opposition. If the right knee is flexing at any given moment, the left knee will be extending at the same moment. Thus the motion of only one leg at a time will be considered. The most pedal effective, force applied is that which is perpendicular to the crank. The ankle joint will ideally remain nearly neutral (pedal level), so that all force applied through power phase will follow a tangential line, perpendicular to the crank [1].

2. Literature review

There are many researchers who have studied the subjects which related to bicycle as: Jim M. Papadopoulos [5], studied the bicycle pedaling and the forces which exerted on the muscles by using two actuators for modeling the real muscles one to move the thigh and another to move the leg, by used real model as four-bar mechanisms.

Jim M. Papadopoulos, R. Scott Hand and Andy Ruina [6], presented the linearized equations of motion for lateral motion for a basic bicycle (not for pedaling).

D. G. Kooijman, J.P.Meijaurd &A.L. Schwab [7], were Studied the bicycle stability by experimental test by equipped with sensor, data acquisition unit and laptop on the rear rack to measure forward speed, steering angle, lean rate and yaw rate, where the experimental results were within the results obtained from the linearized analysis on the simple bicycle model.

Grant Bullock, Davon Cabraloff, Jessica Hickman, Mark Mico, Laura Netcher & Dan Ward [3] discussed the muscle activity during phases of pedaling. They divided the pedal stroke into four individual phases of moment and identified the mechanical purpose of each phase.

3. The goal of this study

The main goal of this study is to derive kinematic equations of pedaling, which will use to get the optimum seat position. These equations will describe the positions (angles), the velocities (angular and linear velocities) and acceleration (tangential, radial and linear accelerations) of the thigh, calf, and crank, when changing angle and height of seat position.

4. Kinematic analysis for peddling

4.1 Vector position analysis

The vectors loop closes on itself making the sum of the vectors around the loop is zero [8]:

$$R_{AO2} + R_{BA} - R_{BO4} - R_{O4O2} = \text{Zero}$$

Substitute the complex number notation for each position vector gives:

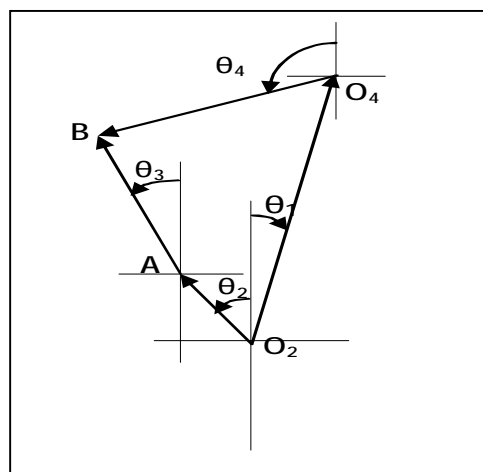


Figure (1). Modeling of pedaling as four-bar linkage.

$$ae^{j\theta_2} + be^{j\theta_3} - ce^{j\theta_4} - de^{-j\theta_1} = \text{Zero} \quad (1)$$

where : a, b, c, and d are the length of pedaling crank, calf, thigh and ground link respectively.

θ_2 , θ_3 , θ_4 , and θ_1 are the angles of pedaling crank, Calf, thigh and ground link respectively as shown in figure (1).

$\overline{O_2O_4}$: is the ground link (is the link between center of pedal to seat position).

$\overline{AO_2}$: is pedal crank link.

\overline{BA} : is the calf link.

$\overline{BO_4}$: is the thigh link.

θ_2 : is independent variable.

∴ Euler identity: $e^{\pm j\theta} = (\cos \theta \pm j \sin \theta)$.

Substitute Euler identity in equation (1) gives:

$$a(\cos \theta_2 + j \sin \theta_2) + b(\cos \theta_3 + j \sin \theta_3) - c(\cos \theta_4 + j \sin \theta_4) - d(\cos \theta_1 - j \sin \theta_1) = \text{Zero} \quad (2)$$

equation (2) can be separated into its real and imaginary parts and each set to zero:

real part:

$$a \cos \theta_2 + b \cos \theta_3 - c \cos \theta_4 - d \cos \theta_1 = \text{Zero} \quad (3)$$

imaginary part:

$$a \sin \theta_2 + b \sin \theta_3 - c \sin \theta_4 + d \sin \theta_1 = \text{Zero} \quad (4)$$

Square both sides of the real and imaginary equations and add them, then arrange, gives:

$$\begin{aligned} & (\cos \theta_2 \cos \theta_4 + \sin \theta_2 \sin \theta_4) \\ & = [K_3 - K_2 * M * \cos \theta_2 + K_2 * N * \sin \theta_2 + K_1 * M * \cos \theta_4 - K_1 * N * \sin \theta_4] \end{aligned} \quad (5)$$

Where:

$$M = \cos \theta_1, \quad N = \sin \theta_1, \quad K_1 = \frac{d}{a}, \quad K_2 = \frac{d}{c}, \quad K_3 = \frac{a^2 - b^2 + c^2 + d^2}{2ac}$$

$$\therefore \sin \theta_4 = \frac{2 \tan(\frac{\theta_4}{2})}{1 + (\tan(\frac{\theta_4}{2}))^2} \quad (6)$$

$$\text{and } \cos \theta_4 = \frac{1 - (\tan(\frac{\theta_4}{2}))^2}{1 + (\tan(\frac{\theta_4}{2}))^2} \quad (7)$$

Substituting equations (6) and (7) in equation (5) gives:

$$\begin{aligned} & \tan^2 \left(\frac{\theta_4}{2} \right) [K_3 - K_2 * M * \cos \theta_2 + K_2 * N * \sin \theta_2 + \cos \theta_2 - K_1 * M] \\ & + \tan \left(\frac{\theta_4}{2} \right) [2 \sin \theta_2 + 2 K_1 * N] \\ & + [K_3 - K_2 * M * \cos \theta_2 + K_2 * N * \sin \theta_2 - \cos \theta_2 + K_1 * M] = \text{Zero} \end{aligned}$$

The solution of quadratic is:

$$\theta_4 = 2 * \tan^{-1} \left[\frac{-(B) \pm \sqrt{(B^2 - 4 * A * C)}}{2 * A} \right] \quad (8)$$

Where:

$$A = [K_3 - K_2 * M * \cos \theta_2 + K_2 * N * \sin \theta_2 + \cos \theta_2 - K_1 * M]$$

$$B = -[2 \sin \theta_2 + 2 K_1 * N]$$

$$C = [K_3 - K_2 * M * \cos \theta_2 + K_2 * N * \sin \theta_2 - \cos \theta_2 + K_1 * M]$$

The solution for angle θ_3 is essentially similar to that for θ_4 :

Rearranging equations (3) and (4) as follows:

$$c \cos \theta_4 = (a \cos \theta_2 + b \cos \theta_3 - d \cos \theta_1) \quad (9)$$

$$c \sin \theta_4 = (a \sin \theta_2 + b \sin \theta_3 + d \sin \theta_1) \quad (10)$$

Square both sides of equations (9) and (10) respectively, and add them, then arrange and substitute the half angle identities will convert the $\sin \theta_3$ and $\cos \theta_3$ terms to $\tan \theta_3$, gives:

$$\begin{aligned} \tan^2 \left(\frac{\theta_3}{2} \right) [\cos \theta_2 (1 + K_4 * M) - K_4 * N * \sin \theta_2 + K_5 - K_1 * M] \\ + \tan \left(\frac{\theta_3}{2} \right) [2 K_1 * N + 2 \sin \theta_2] + [\cos \theta_2 (K_4 * M - 1) \\ - K_4 * N * \sin \theta_2 + K_5 + K_1 * M] = \text{Zero} \end{aligned}$$

Where:

$$K_4 = \frac{d}{b}, \quad K_5 = \frac{-a^2 - b^2 + c^2 - d^2}{2ab}$$

The solution of quadratic is:

$$\theta_3 = 2 * \tan^{-1} \left[\frac{-(E) \pm \sqrt{(E^2 - 4 * D * F)}}{2 * D} \right] \quad (11)$$

Where:

$$D = [\cos \theta_2 (1 + K_4 * M) - K_4 * N * \sin \theta_2 + K_5 - K_1 * M]$$

$$E = -[2 K_1 * N + 2 \sin \theta_2]$$

$$F = [\cos \theta_2 (K_4 * M - 1) - K_4 * N * \sin \theta_2 + K_5 + K_1 * M]$$

4.2 Vector velocity analysis

For velocity expression differentiate the equation (1) respect to time, gives:

$$\begin{aligned} j \frac{d\theta_2}{dt} a e^{j\theta_2} + j \frac{d\theta_3}{dt} b e^{j\theta_3} - j \frac{d\theta_4}{dt} c e^{j\theta_4} + j \frac{d\theta_1}{dt} d e^{-j\theta_1} = \text{Zero} \\ j \omega_2 a e^{j\theta_2} + j \omega_3 b e^{j\theta_3} - j \omega_4 c e^{j\theta_4} = \text{Zero} \end{aligned} \quad (12)$$

Where : $\frac{d\theta_1}{dt} = \text{Zero}$ (because the linkage is stationary).

And let $\frac{d\theta_2}{dt} = \omega_2$, $\frac{d\theta_3}{dt} = \omega_3$, and $\frac{d\theta_4}{dt} = \omega_4$

Where the θ_3 and θ_4 are obtained from position analysis equation (11) and (8) respectively.

Substitute the Euler identity in equation (12), gives:

$$j\omega_2 a(\cos\theta_2 + j\sin\theta_2) + j\omega_3 b(\cos\theta_3 + j\sin\theta_3) - j\omega_4 c(\cos\theta_4 + j\sin\theta_4) = \text{Zero} \quad (13)$$

Separate equation (13) into its real and imaginary parts and set each part to zero gives:

real part:

$$-a\omega_2 \sin\theta_2 - b\omega_3 \sin\theta_3 + c\omega_4 \sin\theta_4 = \text{Zero} \quad (14)$$

imaginary part:

$$a\omega_2 \cos\theta_2 + b\omega_3 \cos\theta_3 - c\omega_4 \cos\theta_4 = \text{Zero} \quad (15)$$

solving equations(14) and(15) gives:

$$\omega_3 = \frac{a\omega_2 \sin(\theta_4 - \theta_2)}{b \sin(\theta_3 - \theta_4)} \quad (16)$$

$$\omega_4 = \frac{a\omega_2 \sin(\theta_2 - \theta_3)}{c \sin(\theta_4 - \theta_3)} \quad (17)$$

The relative velocity:

$$V_A + V_{BA} - V_B = \text{zero}$$

Where:

$$V_A = j\omega_2 a e^{j\theta_2} = a\omega_2 (-\sin\theta_2 + j\cos\theta_2) \quad (18)$$

$$V_{BA} = j\omega_3 b e^{j\theta_3} = b\omega_3 (-\sin\theta_3 + j\cos\theta_3) \quad (19)$$

$$V_B = j\omega_4 c e^{j\theta_4} = c\omega_4 (-\sin\theta_4 + j\cos\theta_4) \quad (20)$$

4.3 Vector acceleration analysis

Now, differentiating equation(12) versus time to obtain an expression for acceleration in the linkage gives:

$$(j^2 a \omega_2^2 e^{j\theta_2} + j a \alpha_2 e^{j\theta_2}) + (j^2 b \omega_3^2 e^{j\theta_3} + j b \alpha_3 e^{j\theta_3}) - (j^2 c \omega_4^2 e^{j\theta_4} + j c \alpha_4 e^{j\theta_4}) = \text{zero}$$

Simplifying and grouping terms give:

$$(j a \alpha_2 e^{j\theta_2} - a \omega_2^2 e^{j\theta_2}) + (j b \alpha_3 e^{j\theta_3} - b \omega_3^2 e^{j\theta_3}) - (j c \alpha_4 e^{j\theta_4} - c \omega_4^2 e^{j\theta_4}) = \text{zero} \quad (21)$$

Where:

α_2 = angular acceleration of pedal = $\frac{d\omega_2}{dt}$ (rad/sec).

α_3 = angular acceleration of calf = $\frac{d\omega_3}{dt}$ (rad/sec).

α_4 = angular acceleration of thigh = $\frac{d\omega_4}{dt}$ (rad/sec).

Substituting the Euler identity in each term of equation (21) then collecting all real and all imaginary terms separately gives:

Real part:

$$-a\alpha_2 \sin \theta_2 - a\omega_2^2 \cos \theta_2 - b\alpha_3 \sin \theta_3 - b\omega_3^2 \cos \theta_3 + c\alpha_4 \sin \theta_4 - c\omega_4^2 \cos \theta_4 = \text{Zero} \quad (22)$$

Imaginary part:

$$a\alpha_2 \cos \theta_2 - a\omega_2^2 \sin \theta_2 + b\alpha_3 \cos \theta_3 - b\omega_3^2 \sin \theta_3 - c\alpha_4 \cos \theta_4 + c\omega_4^2 \sin \theta_4 = \text{Zero} \quad (23)$$

Solving equations (22) and (23) simultaneously gives:

$$\alpha_3 = \frac{R * S - P * U}{P * T - Q * S} \quad (24)$$

$$\alpha_4 = \frac{R * T - Q * U}{P * T - Q * S} \quad (25)$$

Where:

$$P = c \sin \theta_4$$

$$Q = b \sin \theta_3$$

$$R = a\alpha_2 \sin \theta_2 + a\omega_2^2 \cos \theta_2 + b\omega_3^2 \cos \theta_3 - c\omega_4^2 \cos \theta_4$$

$$S = c \cos \theta_4$$

$$T = b \cos \theta_3$$

$$U = a\alpha_2 \cos \theta_2 - a\omega_2^2 \sin \theta_2 - b\omega_3^2 \sin \theta_3 + c\omega_4^2 \sin \theta_4$$

The relative acceleration and linear accelerations are:

$$A_A + A_{BA} - A_B = \text{Zero}$$

$$A_A = (A_A^t + A_A^n) = j a \alpha_2 e^{j\theta_2} - a \omega_2^2 e^{j\theta_2} \\ = a \alpha_2 (-\sin \theta_2 + j \cos \theta_2) - a \omega_2^2 (\cos \theta_2 + j \sin \theta_2) \quad (26)$$

$$A_B = (A_B^t + A_B^n) = j c \alpha_4 e^{j\theta_4} - c \omega_4^2 e^{j\theta_4} \\ = b \alpha_3 (-\sin \theta_3 + j \cos \theta_3) - b \omega_3^2 (\cos \theta_3 + j \sin \theta_3) \quad (27)$$

$$A_{BA} = (A_{BA}^t + A_{BA}^n) \\ = j b \alpha_3 e^{j\theta_3} - b \omega_3^2 e^{j\theta_3} c \alpha_4 (-\sin \theta_4 + j \cos \theta_4) \\ - c \omega_4^2 (\cos \theta_4 + j \sin \theta_4) \quad (28)$$

Equations (24) to (28) are complete solution for the angular acceleration of the links and the linear acceleration of the joints in the pin jointed four bar linkage.

5. Results and discussion

To check the kinematic equations (derived equations) of four-bar mechanisms, an the example of four bar mechanism modeling was used as shown in figure (2) in MATLAB Package / Simulink / SimMechanics as shown in Table (1).

Table (1). Specifications of four-bar mechanisms.

| Link | Length (cm) | Angle (degree) | Note: Consider as |
|-------------------------------|-------------|----------------|-------------------|
| Crank link(Shortest link) | 12 | 60 | Pedal of bike |
| Stationary link(Longest link) | 86.7 | 0.0 | Height of seat |
| Rocker link | 60 | 83.96 | Thigh of rider |
| Coupler link | 100 | 29.52 | Calf of rider |

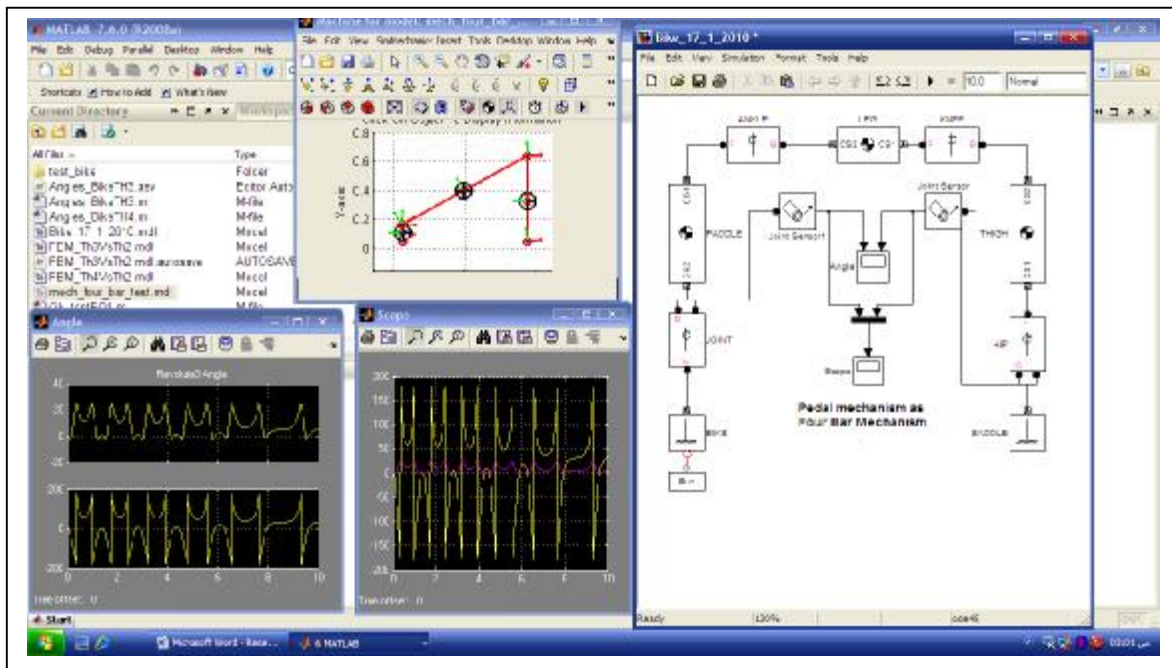
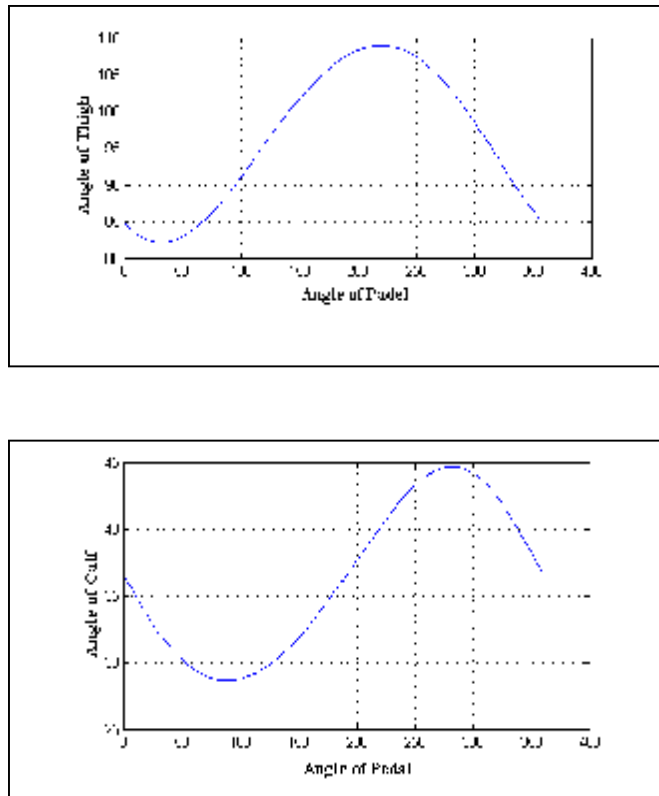


Figure (2). Simulation of four-bar mechanism in MATLAB/Simulink/Sim-mechanics.

By using MATLAB editor to calculate equations (8) and (11), the plot of the angle of thigh versus the pedal angle, and the angle of calf versus the pedal angle respectively as shown in figure (3), were coincided with the angles of thigh and calf versus pedal angle which obtained from four-bar modeling, (where the absolute angle of revolute motion is

mapped in angle or scope window(as shown in figure-2) on to the interval -180° , $+180^{\circ}$, thus the angles are modified to be suitable for global coordinates).

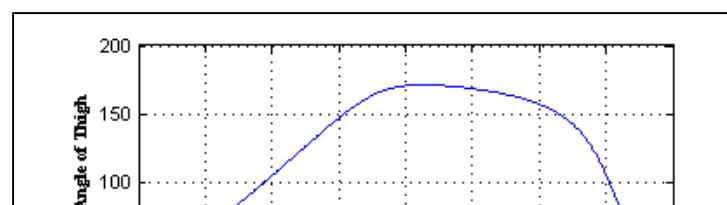


Figure(3). The angles of thigh and calf versus angle of pedal, from derived equations and four-bar model .

When the derived equations compared with graphical method and with the information of example of quadric cycle chain [8], the dimensions of four bar chain are given in Table (2). The derived kinematic equations coincide with result of the example as shown in figure (4), also .

Table (2). Dimensions of four-bar chain.

| Link | Length (cm) | Angle (degree) | Angular velocity(rad/s) | Consider as |
|-----------------|-------------|----------------|-------------------------|----------------|
| Crank link | 15 | 60 | 10 | Pedal of bike |
| Stationary link | 22 | 0.0 | 0.0 | Height of seat |
| Rocker link | 18 | 73.76 | 7.0 | Thigh of rider |
| Coupler link | 20 | 12.39 | -2.035 | Calf of rider |



Figure(4). Angular velocity of thigh and calf versus angle of pedal.

6. Conclusions

The derived equations in this study can be considered as equations to describe the kinematic motion of the four-bar mechanism.

The equation (8) has two solutions, obtained from the \pm conditions on the radical. These two solutions as with any quadratic equation, may be of three types: real and equal, real and unequal, and complex conjugate. The complex conjugate solution means that the link lengths chosen are not capable of connection for the chosen value of the input angle θ_2 . Thus the links must satisfy the Grashof Condition which satisfies crank-rocker : (length of shortest link(pedal length) + length of longest link(saddle position) < length of one remaining link (Thigh length) + length of other remaining link(calf length)).[8]

The real and unequal solution means that there are two values of θ_4 corresponding to any value of θ_2 , these are referred to as the crossed and open configurations of the linkage, as the two circuits of the linkage.

Where the minus solution gives θ_4 for the open configuration (which was taken in this study), and positive solution gives θ_4 for the crossed configuration. Also, the minus solution

gives θ_3 for the open configuration (which was taken in this study), and positive solution gives θ_3 for the crossed configuration.

7. References

- [1] Gonzalez H, Hull M.L. 1989 "Multivariable Optimization of Cycling Biomechanics" Journal of Biomechanics, 1151-1153.
- [2] Burke, Edmond R., 2002, "Serious Cycling". Second Edition, Publisher: Human Kinetics.
- [3] Grant Bullock, Davon Cabraloff, Jessica Hickman, Mark Mico, Laura Netcher & Dan Ward , 2009 "A qualitative Analysis of The Biomechanics of Proper Pedal Stroke".
- [4] White, Peter. , 2009, "How to Fit a Bicycle". www.peterwhitecycles.com.
- [5] Jim M. Papadopoulos, 1987, " Force in Bicycle Pedaling" , ASME, Biomechanics sport volume.
- [6] Jim M. Papadopoulos, . Scott Hand and Andy Ruina, 1990 "Bicycle and Motorcycle Balance and Steer Dynamics".
- [7] J. D. G. Kooijman, J.P.Meijaurd &A.L. Schwab, 2006 "Experimental Bicycle Dynamics".
- [8] V.Ramamurti, 2005, "Mechanics of Machines", second edition, Alpha Science International Ltd. Harrow, U.K.

8. Nomenclature

| | |
|-------------------|--|
| $\overline{AO2}$ | Vector of pedal link. |
| \overline{BA} | Vector of calf link. |
| $\overline{BO4}$ | Vector of thigh link. |
| $\overline{O2O4}$ | Vector of ground link (is the link between center of pedal to seat position). |
| ω_2 | Angular velocity of pedal link (rad/sec). |
| ω_3 | Angular velocity of calf link (rad/sec). |
| ω_4 | Angular velocity of thigh link (rad/sec). |
| A_A^n | Normal acceleration of pedal link (m/sec ²). |
| A_A^t | Tangential acceleration of pedal link (m/sec ²). |
| A_{BA}^n | Normal acceleration of calf link relative to pedal link (m/sec ²). |
| A_{BA}^t | Tangential acceleration of calf link relative to pedal link (m/sec ²). |
| A_E^n | Normal acceleration of thigh link (m/sec ²). |

| | |
|------------|--|
| A_B^t | Tangential acceleration of thigh link (m/sec ²). |
| V_A | Linear velocity of pedal link (m/sec). |
| V_B | Linear velocity of thigh link (m/sec). |
| V_{BA} | Linear velocity of calf link relative to pedal link (m/sec). |
| α_2 | Angular acceleration of pedal link (rad/sec ²). |
| α_3 | Angular acceleration of calf link (rad/sec ²). |
| α_4 | Angular acceleration of thigh link (rad/sec ²). |
| a | Length of pedaling link (m). |
| b | Length of calf link (m). |
| c | Length of thigh link (m). |
| d | Length of seat tube link (m). |
| θ_1 | Angle of seat tube link (degree). |
| θ_2 | Angle of pedaling link (degree). |
| θ_3 | Angle of calf link (degree). |
| θ_4 | Angle of thigh link (degree). |

Numerical Investigation of Heat Transfer and Fluid Flow a cross Circular and Elliptical Tube Bank

Ghassan Adnan Abd

Mechanical Engineering Department

College of Engineering

Thi-Qar University

Ghassan_adnan77@yahoo.com

Abstract

In this study, a numerical investigation of heat transfer and fluid flow a cross circular and elliptical tube bank has been made then comparisons made between these two types. The study focus on the effect of Reynolds number and ellipse eccentricity on the Nusselt number and pressure drop through the tube bank for two arrangements (in-line and staggered). The results are reported for air and for Reynolds number range of $20 \leq Re \leq 500$. The results of the study shows that Nusselt number increased as Reynolds number increased for all cases. The values of Nusselt number for elliptical tube are higher than for circular tube for Reynolds number range of $100 \leq Re \leq 500$. The pressure drop for the two arrangements increased as the Reynolds number increases. The elliptical tube array has batter thermal performance and lower pressure drop than circular tube array .

المستخلص

تم في هذا البحث دراسة انتقال الحرارة وجريان السائل خلال نوعين من مجمعات الأنابيب عدديا. مجمع ذا أنابيب دائرية المقطع ومجمع ذا أنابيب بيضوية المقطع ثم تم المقارنة بينهما . تم دراسة تأثير عدد رينولد و درجة تحدب المقطع البيضوي على عدد نسلت وانخفاض الضغط خلال مجمع الأنابيب لنوعين من الترتيب هما (الخطي والمتعرج). النتائج المستخلصة كانت للهواء ولعدد رينولد بحدود $20 \leq Re \leq 500$. النتائج التي تم الحصول عليها تشير إلى إن عدد نسلت يزداد مع زيادة عدد رينولد لكل الحالات . كذلك فان قيمة عدد نسلت للأنابيب البيضوية اكبر للأنابيب الدائرية لقيم عدد رينولد $100 \leq Re \leq 500$. هبوط الضغط لكلا الترتيبين يزداد بزيادة عدد رينولد . كذلك وجد إن الأنابيب البيضوية لها أفضل أداء حراري من الأنابيب الدائرية.

1. Introduction

Heat exchangers have been playing a huge role in energy applications. Many studies have been done to improve the thermal and hydraulic performance of heat exchanger. Austin et al [1] studied the effect of the entering water jet on the heat transfer coefficient and pressure drops across of 10-row depth having staggered and in-line tube arrangement. For there study the heat transfer coefficient was found strongly dependent on the transverse and longitudinal position of the tube in the first rows.

Fujii et al[2] studies numerical analysis of laminar flow and heat transfer in tube bank. They solved numerically the two-dimensional Navier-Stokes and enegy equations. The calculation are carried out for in-line square tube bank up to five rows deep,with pitch –to diameter ratios 1.5×1.5 under the condition of uniform tube wall temperature for $Re = 60, 120$ and 300 . An analogous relation between an in-line tube bank and parallel plates with heat transfer characteristics is presented.

Ota et al[3] studied the flow in the neighborhood of an elliptical cylinder with an axis ratio of 0.33 in the Reynolds number range (based on major axis length) from 3.5×10^4 to 1.25×10^5 , where a discontinuous variation of both the drag and lift were observed. It is evidenced that at cross-flow the elliptical tube perform better drag than the circular tube .

Zdravistch et al[4] studied numerically the predication of the laminar and the turbulent fluid flow and heat transfer in the tube banks .Two tube arrangement investigated staggered and in-line tube banks. The cell-centred finit-volume algorithm is used to solve the steady state Reynolds-averaged Navier-Stokes equations. Two-dimensional results include velocity vectors and streamline, surfaces shear stresses, pressure coefficient distributions, temperature contours, local Nusselt number distributions and average convective heat transfer coefficient. These results indicate good agreement with experimental data.

Nishiyama et al[5] investigated the effects of cylinder spacing and angle of attack on heat transfer for elliptical tube. They found that the angle of attack as wall as the cylinder spacing influence the local heat transfer coefficient. They concluded that the cylinder spacing and angle of attack, should be arranged as small as possible to minimize the drag and to achieve higher heat transfer rate.

Badr[6] conducted a numerical study with a single elliptical cylinder and investigated the effects of Reynolds number, cylinder axis ratio and the angle of attack on heat transfer. The Reynolds number (based on the focal distance) varied from 20 to 500 for a constant

Prandtl number of 0.7. The axis ratio was varied between 0.4 and 0.9 for zero angle of attack and for a fixed Reynolds number of 100. In addition, the angle of attack was altered from 0° to 90° for a fixed axis ratio of 0.5 for Reynolds number between 20 to 500. He found that the maximum Nusselt number occurred at zero angle of attack and the maximum heat transfer at small axis ratio.

Nasibi and Shicani [7] investigated the laminar flow of air around three isothermal horizontal cylinders in an in-line tube bank. They used a body fitted curvilinear system with Beam-Wrming numerical method to solve full Navier-Stokes and energy equations. They study the effects of longitudinal and transverse pitches and Reynolds number ranged 25-2500 on the flow parameters such as streamlines, surface pressure, total drag, pressure drag and friction drag coefficient. They found that the change of longitudinal and transverse pitches and Reynolds number effects the flow parameters, As longitudinal pitch is decrease, the wakes behind the cylinder are spread between two rows. The drag coefficient as Reynolds number increased as the transverse pitch increased.

Harris and Goldschmidt [8] investigated the effect of axis ratio and angle of attack on overall heat transfer in the Reynolds number range from 7.4×10^3 to 7.4×10^4 . Both the Reynolds number and Nusselt number were based on the length of the major axis. They concluded that an axis ratio of 0.3 or less must be achieved to realize any appreciable change in heat transfer coefficient greater than 10% over the elliptical tube.

The objective of the present study is to numerically study the heat transfer and fluid flow across circular and elliptical tube bank then a comparison between the two types.

2. Mathematical formulation

Both in-line and staggered arrangement are considered for analysis. A total of six longitudinal rows have been considered. The working media is air of ($Pr=0.7$). The arrangements considered in this study are shown in Figures (1) and (2). The comparison is done by comparing circular array of tube diameter 1 cm with elliptical array. The ellipsoidal tubes were designed with the ratio of 0.8, 0.6 and 0.4 between the minimum and the maximum ellipse radius (b and a). This ratio is ellipse eccentricity ($e = b/a$). To give the same heat exchange area for all cases. To simplify the numerical solution and reducing the run time and due to similarity a heat exchanger module (HEM) consist of two tubes as shown in figures(1)and (2).

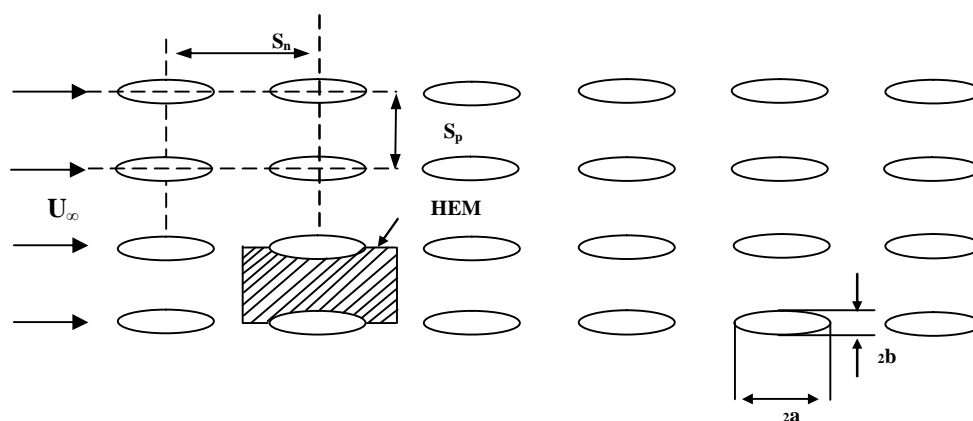


Figure (1). In-line arrangement of tube array .

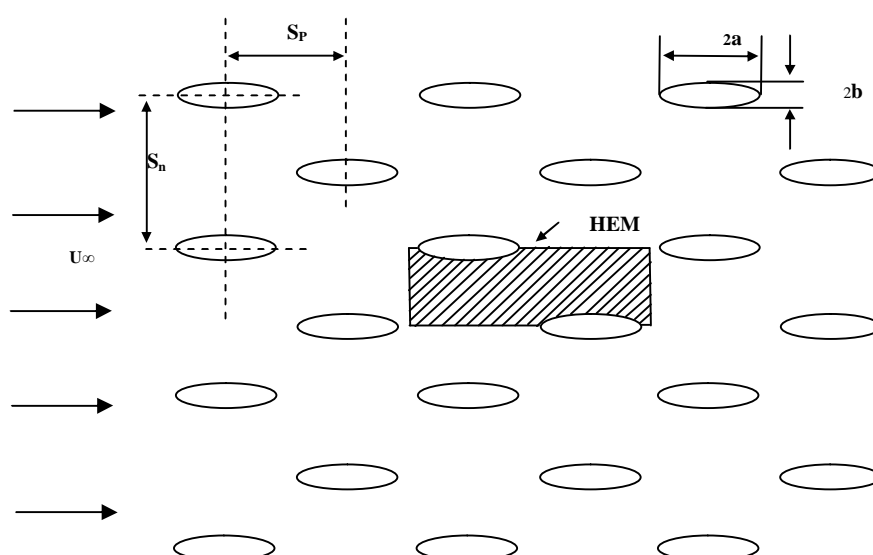


Figure (2). Staggered arrangement of tube array.

The parameters considered for numerical simulation are $20 \leq Re \leq 500$, $Pr = 0.7$. Reynolds number is define as

$$Re = \frac{U_{\max} D_H}{n} \quad (1)$$

Where:

$$D_H = \frac{4A_e}{P} \quad (2)$$

The flow is fully developed hydrodynamically and thermally. The thermo physical properties assumed constant and taken at the inlet temperature of the fluid.

2.1 Governing equations

For steady state, two-dimensional, incompressible flow, and constant fluid property, the governing equations are:

Continuity equation:

$$\frac{\partial U}{\partial X} + \frac{\partial V}{\partial Y} = 0 \quad (3)$$

X- momentum equation:

$$r \left[U \frac{\partial U}{\partial X} + V \frac{\partial U}{\partial Y} \right] = - \frac{\partial P}{\partial X} + m \left[\frac{\partial^2 U}{\partial X^2} + \frac{\partial^2 U}{\partial Y^2} \right] \quad (4)$$

Y-momentum equation:

$$r \left[U \frac{\partial V}{\partial X} + V \frac{\partial V}{\partial Y} \right] = - \frac{\partial P}{\partial Y} + m \left[\frac{\partial^2 V}{\partial X^2} + \frac{\partial^2 V}{\partial Y^2} \right] \quad (5)$$

Energy equation:

$$rC_p \left[U \frac{\partial T}{\partial X} + V \frac{\partial T}{\partial Y} \right] = K \left[\frac{\partial^2 T}{\partial X^2} + \frac{\partial^2 T}{\partial Y^2} \right] \quad (6)$$

2.2. Boundary condition:

2.2.1 Inlet condition

The fluid is assumed to enter with a uniform horizontal velocity, U_{in} and temperature of T_{in} .

$$U=U_{in}, T=T_{in}, V=0$$

2.2.2. Symmetry condition

For the top and bottom surfaces of the computational domain excluding the tube surfaces, symmetry boundary condition is used. The mathematical form of this condition is

$$\frac{\partial U}{\partial Y} = 0, V = 0, \frac{\partial T}{\partial Y} = 0$$

2.2.3. Wall condition

At the tube surfaces no slip condition is applied as far as energy equation is consider the tube is at isothermal condition:

$$U = V = 0, T = T_w$$

2.2.2 Outlet condition

Zero diffusion flux implemented for all variables at the outlet boundary.

$$\frac{\partial U}{\partial X} = \frac{\partial V}{\partial X} = \frac{\partial T}{\partial X}$$

The calculation of Nusselt number for the isothermal boundary condition:

$$Nu = \frac{hD_H}{K} \quad (7)$$

Where h is given by

$$h = \frac{Q}{A(T_w - T_b)} \quad (8)$$

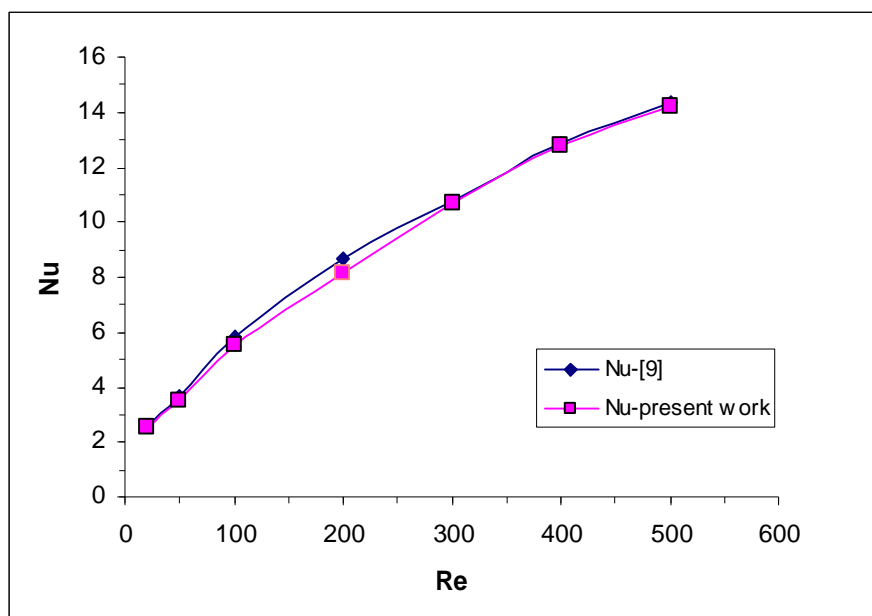
And

$$Q = \dot{m} C_p [T_b(\text{out}) - T_b(\text{in})] \quad (9)$$

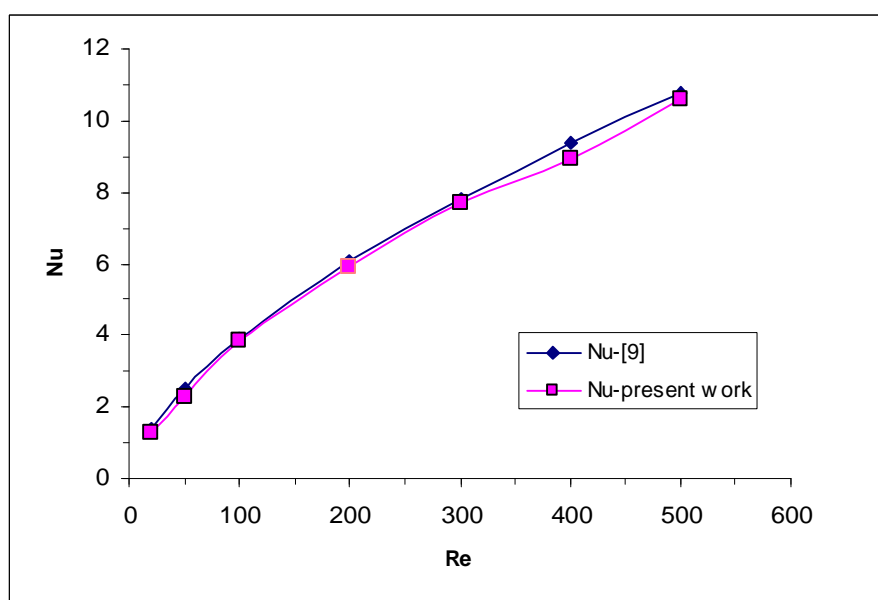
The governing continuity, fluid flow and energy equations (3-6) along with boundary conditions are solved simultaneously by using a finite volume method. Steady segregated solver was used with second order upwinding scheme for the convective terms in the momentum and energy equations. For pressure-velocity coupling, pressure implicit with splitting of operators (PISO) scheme was used. A convergence criterion of 1×10^{-6} was applied to the residual of the continuity and the momentum equations and 1×10^{-9} to the residual of the energy equation.

3. Validation

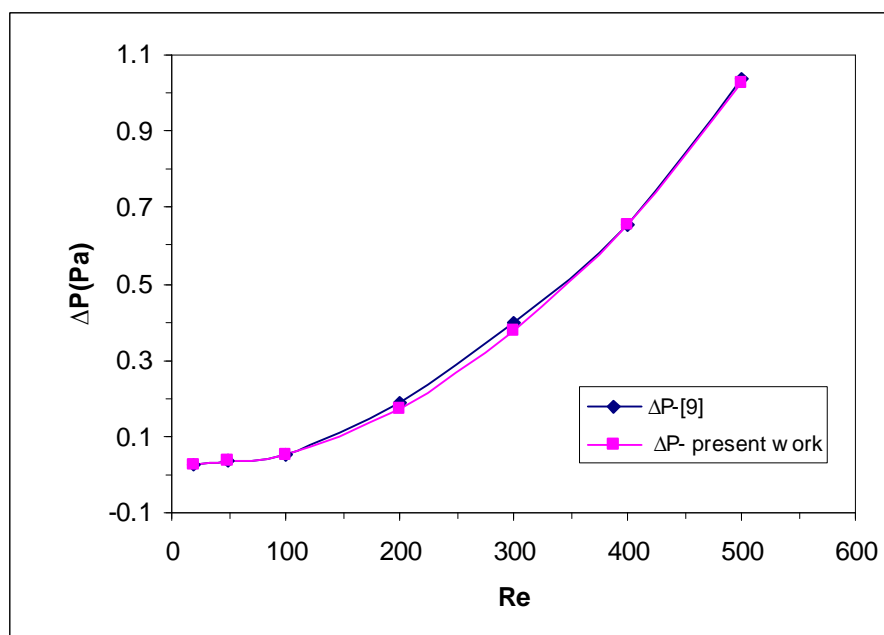
In order to check the validity of the present work, a comparison is made with [9]. A comparison of the Nusselt number and the pressure drop for the two arrangement in-line and staggered are made. Circular tube array of six longitudinal rows have been considered with tube diameter $d=1$ cm, $S_n=2$ cm and $S_p=2$ cm. Figure (3) shows the comparison between Nusselt number obtained from [9] with Nusselt number obtained from present model for staggered arrangement, from this Figure it can be seen that the agreement is accepted and the average error is 2.6%. From figure (4), it can be observed that the comparison of the Nusselt number computed from (9) with Nusselt number from present model for in-line arrangement also with accepted agreement, The average error is 3.6%. In Figure (5) the comparison of pressure drop calculated from [9] with pressure drop obtained from present model for staggered arrangement. The average error is 3.8 %. The comparison of pressure drop calculated from [9] with pressure drop obtained from present model for in-line arrangement is shown in Figure(6). The average error is 2.8 %. From the above results, it can be concluded that the present model have good accuracy.



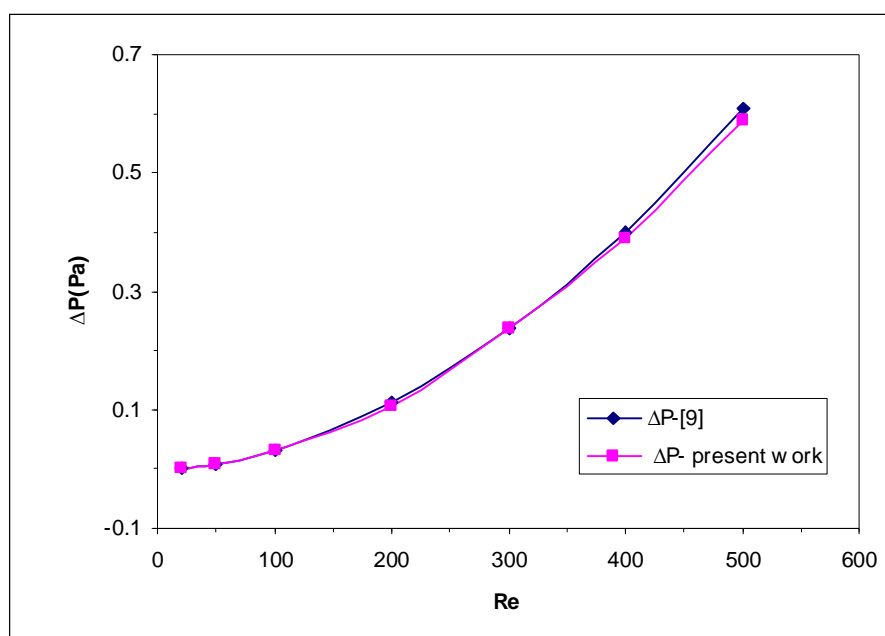
Figure(3). Comparison of Nu of [9] with Nu of present work for staggered arrangement.



Figure(4). Comparison of Nu of [9] with Nu of present work for in-line arrangement .



Figure(5). Comparison pressure drop of [9] with pressure drop of present work for staggered arrangement .



Figure(6). Comparison pressure drop of [9] with pressure drop of present work for in-line arrangement.

4. Results and discussion

The effect of a constant temperature boundary condition on the steady fluid flow and heat transfer is analyzed here Figure(7) shows the variation of Nusselt number with Reynolds number for staggered arrangement for circular and elliptical tube that have ellipse eccentricity $e=0.8$, $e=0.6$ and $e=0.4$. It can be seen that, Nusselt number increase with increasing of Reynolds number for all cases. The Nusselt number for elliptical tube is less than that of the circular tube for $20 \leq Re \leq 100$. However for $100 \leq Re \leq 500$ this relationship is inverted due to decreases in flow turbulence in case of elliptical tube. The effect of decreases ellipse eccentricity from $e=0.8$ to $e=0.4$, it gave high Nusselt number for the same Reynolds number. The maximum heat gain at ellipse eccentricity $e=0.4$.

Figure(8) shows the variation of Nusselt number with Reynolds number for in-line arrangement for circular and elliptical tube that have ellipse eccentricity $e=0.8$, $e=0.6$ and $e=0.4$. The Nusselt number exhibit the same behavior as that observed in staggered arrangement. The Nusselt number value have lowest than in staggered arrangement. From the above Figures, it can be observe that from a heat transfer point of view staggered arrangement performs better than in-line arrangement.

Figure(9) shows variation of pressure drop with Reynolds number for staggered arrangement for circular and elliptical tube that have ellipse eccentricity $e=0.8$, $e=0.6$ and $e=0.4$. It can be seen that, the pressure drop increases as the Reynolds number increases. The effect of ellipse eccentricity on the pressure drop are as ellipse eccentricity decreases from $e=0.8$, to $e=0.4$, the pressure drop value decreases for the same Reynolds number mainly due to its more streamline flow pattern. The differences between the pressure drop circular and elliptical tube increase with increase of Reynolds number.

Figure(10) illustrate variation of pressure drop with Reynolds number for in-line arrangement for circular and elliptical tube that have ellipse eccentricity $e=0.8$, to $e=0.4$. It can be observed that pressure drop exhibit the same behavior as was observed in staggered arrangement. The pressure drop value have lowest than in staggered arrangement. From the above Figures, it can be observe that from a pressure drop point of view in-line arrangement performs better than staggered arrangement.

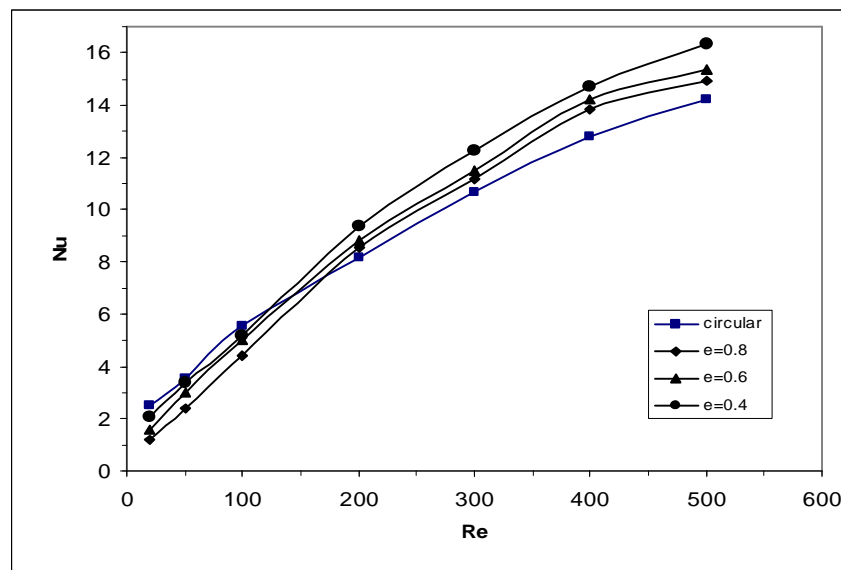
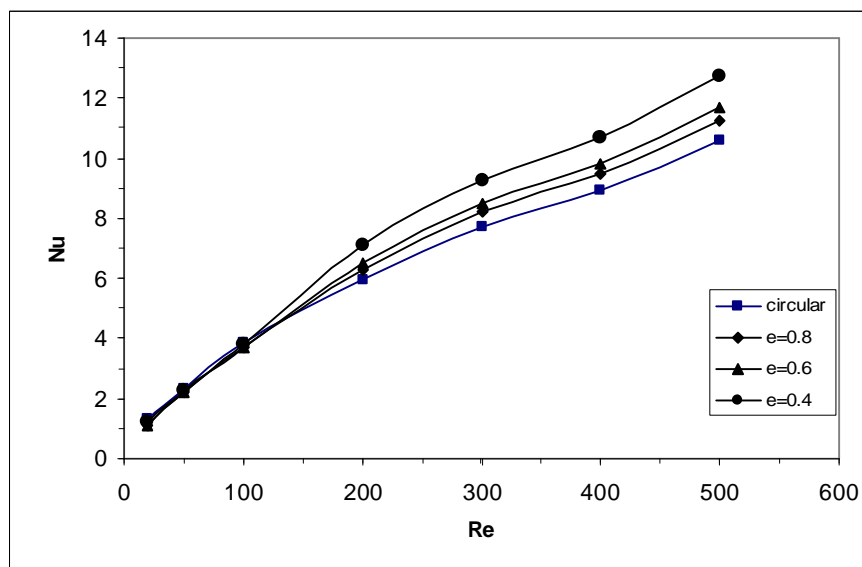


Figure (7). Variation of Nusselt number with Reynolds number for staggered configuration for circular and elliptical tube with ellipse eccentricity $e=0.8$, $e=0.6$ and $e=0.4$



Figure(8). Variation of Nusselt number with Reynolds number for in-line configuration for circular and elliptical tube with ellipse eccentricity $e=0.8$, $e=0.6$ and $e=0.4$

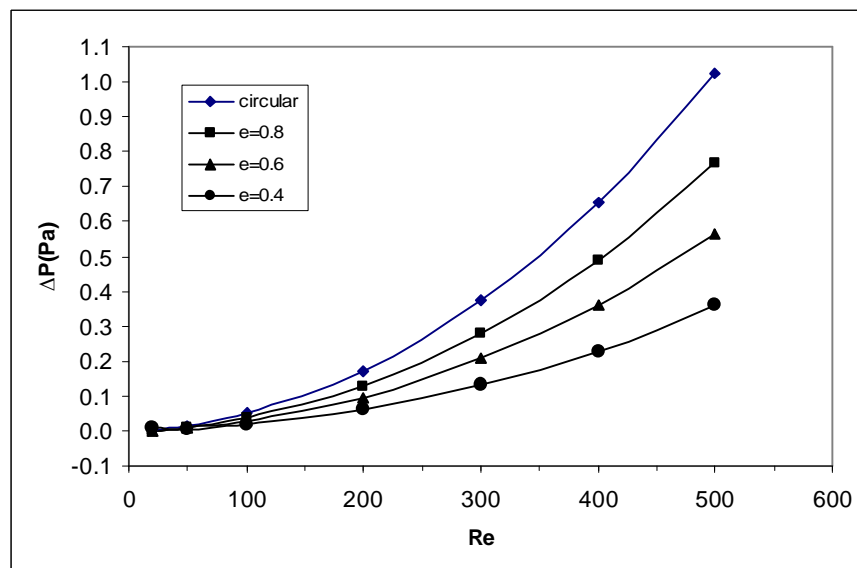


Figure (9). Variation of pressure drop with Reynolds number for staggered configuration for circular and elliptical tube with ellipse eccentricity $e=0.8$, $e=0.6$ and $e=0.4$.

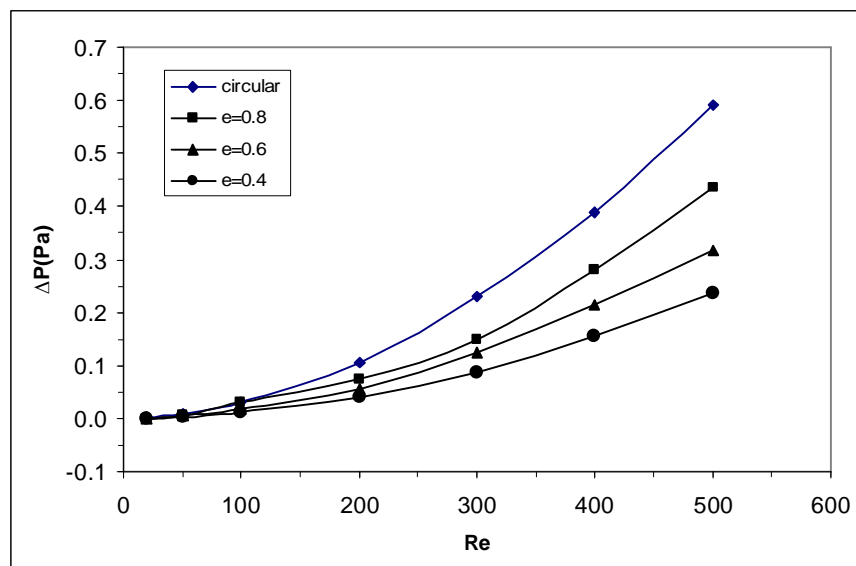


Figure (10). Variation of pressure drop with Reynolds number for in-line configuration for circular and elliptical tube with ellipse eccentricity $e=0.8$, $e=0.6$ and $e=0.4$.

5. Conclusions

Heat transfer and fluid flow a cross circular and elliptical tubes bank was numerically investigated. From the result obtained it can be concluded:

- 1- Nusselt number increased as Reynolds number increased for all cases.
- 2- The effect of decreases ellipse eccentricity from $e=0.8$ to $e=0.4$, it gave high Nusselt number for the same Reynolds number.
- 3- The pressure drop for the two arrangements increased as the Reynolds number increases.
- 4- The effect of decreases ellipse eccentricity from $e=0.8$ to $e=0.4$, it gave lower pressure drop for the same Reynolds number.
- 5- The elliptical tube array has batter thermal performance and lower pressure drop than circular tube array .

6. References

- [1] Asustin, A.A., Beckmann, R.S., Rothfus, R.R., and Kerode, R.I., 1965, "Convective Heat Transfer in Flow Normal to Banks of Tubes", Industrial & Engineering Chemistry Process Design and Development, Vol. 4, pp 379-387 .
- [2] Fujii, M., Fujii, T., Nagata, T., 1984, " Numerical Analysis of Laminar Flow and Heat Transfer of Air in an in-line Tube Banks", Numerical Heat Transfer, Part A, Applications , Vol. 7, Issue 1, pp 89-102.
- [3] Ota, T., Nishigama, H., and Taok, Y., 1987, " Flow Around an Elliptical Cylinder in Critical Reynolds Number Regime", J. Fluid Eng., Trans ASME , Vol. 109, pp 149-155.
- [4] Zdravistch, F., Fletcher, C.A., and Behina, M., 1993, " Numerical Laminar and Tarbulant Fluid Flow and Heat Transfer Predictions in Tube banks", International Journal of Numerical Methods for Heat & Fluid Flow, Vol. 5, Issue 8, pp 717-733.
- [5] Nishigama, H., Ota, T., and Matuno, T., 1998, " Heat Transfer and Fluid Flow Around Elliptical Cylinders in Tandem Arrangment", JSME International Journal, Series 33, Vol. 31 , pp 410-419.
- [6] Badr, H.M., 1998, "Force Convection from a Straight Elliptical Tube", Heat and Mass Transfer, Vol. 34, pp 229-236.
- [7] Nasibi, H., and Shirani, E., 2001, "Numircal simulation of Low Reynolds Number Flows in in-line Tube Bank", Journal of Applied Science , Vol. 1, Issue 3, pp 275-282.

- [8] Harris, D.K., and Goldschmidt, V.W.,2002, " Measurement of The Overall Heat transfer from Combustion Gases Confined Within Elliptical tube Heat Exchanger", Exp. Therm Fluid Sci, Vol.26,pp 33-37.
- [9] Holman, J.P.,1997," Heat Transfer",8th edition ,USA.
- [10] Hewitt, G.F., Shires, G.L., and Bott, R.T.,1994",Process Heat Transfer",USA.

7. Nomenclature

| Symbol | Description |
|------------------|--|
| a | Larger ellipse semi-axis,m. |
| A | Total area of all tubes ,m ² |
| A _e | Ellipse area |
| b | Smaller ellipse semi-axis,m. |
| C _p | Specific heat , J/kg. k |
| d | Tube Diameter,m. |
| D _H | Hydraulic Diameter ,m. |
| h | Heat transfer Coefficient ,W/m ² .k |
| HEM | Heat Exchanger Model |
| K | Thermal conductivity, W/m.k |
| Nu | Nusselt Number |
| P | Ellipse circumference |
| Q | overall heat transfer rate ,W. |
| Re | Reynolds number |
| S _n | longitudinal spacing between tubes ,m. |
| S _p | transverse spacing between tubes ,m. |
| T | Temperature, K. |
| T _b | Bulk Temperature, K. |
| T _{in} | Inlet Temperature, K. |
| T _w | Wall Temperature, K. |
| U _∞ | Upstream Velocity ,m/s. |
| U _{max} | maximum Velocity ,m/s. |
| ν | Kinematic Viscosity ,m ² /s. |
| ΔP | Pressure drop ,Pa. |

Using Geno-Iterative Approach to Identify Weiner and Hammerstein Models

Ali H. Hasan

Thi-Qar University

Abstract

This paper presents a novel method for identification of the Weiner and Hammerstein models and the model's parameters by the application of genetic algorithm optimization method and an iterative search through a lock up Table. The coefficient values of both linear and nonlinear parts are estimated by the GA while the type of nonlinearity and degree of delay of the linear part are determined by the iterative search through the lock up Table. The simulation results show the effectiveness and ability of the proposed algorithm for identification and realization of the Weiner and Hammerstein models that describe the real system.

Keywords: Hammerstein model identification, Weiner model identification, linear and nonlinear system identification , genetic algorithms, iterative method.

المستخلص

قمنا في هذا البحث بعمل طريقة جديدة لإيجاد نماذج Weiner و نماذج Hammerstein المستخدمان في تمثيل الأنظمة الحقيقية المحتوية على المكونات الخطية وغير الخطية وذلك باستخدام مبدأ الخوارزميات الجينية وطريقة البحث التكرارية. استخدمنا طريقة البحث التكرارية لاختيار النماذج الخطية وغير الخطية المكونة لنماذج Weiner و نماذج Hammerstein المستعملة في تمثيل النظام الحقيقي. بينما استخدمنا الخوارزميات الجينية لإيجاد القيم الحقيقية لمعاملات (coefficient) النماذج المستخدمة. بينت النتائج المستحصلة قدرة الطريقة الجديدة لاختيار النماذج وتمثيل النظم الحقيقية من ناحية إيجاد الصيغة الرياضية التي تمثل تصرف هذه النظم وكذلك إيجاد المعاملات الخطية المكونة لهذه الصيغ.

1. Introduction

System identification is the process of finding a model that best produces the data obtained by a system to known inputs, i.e. construct mathematical models from measured input and output data [1]. System identification differs from modeling in that, with modeling the observed system is broken down into subsystems, which can be described mathematically. Identification builds a picture of the system using just the observed data, that is, the input-output signals.

Practical systems have inherently nonlinear characteristics such as saturation and dead zone which grown the importance of nonlinear modeling in control engineering. So the development of accurate non linear system identification is important aspect for analysis and prediction of the system characteristics or control design problem.

Block oriented models are one of the major classes of nonlinear systems, which consist of linear models followed by, or proceeded by a static nonlinear model. This configuration is known as Hammerstein and Wiener models depends on the blocks order, this configuration provides a simple system architecture. More details can be found in [2-6].

The Hammerstein and Wiener models are used to model several classes of nonlinear systems, their flexibility lies in having the nonlinearity part entirely separated from the linear part [7]. Figure 1 represent the block oriented structure:-

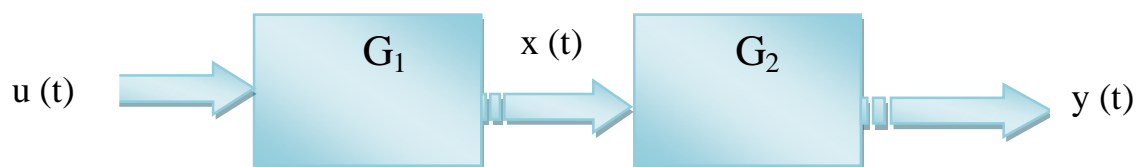


Figure (1). Structure of block oriented representation.

Where:-

$u(t)$ is the input signal to the system, $y(t)$ is the output signal from the system and $x(t)$ is the intermediate non measurable quantity.

G_1 is the static nonlinearity part for Hammerstein model and is the dynamic linear part for Wiener model.

G_2 is the dynamic linear part for Hammerstein model and is the static nonlinearity part for Wiener model.

The Hammerstein model can be described by the following equations:-

$$y(t) = \sum_{i=1}^m (a_i y(t-i)) + \sum_{j=0}^n (b_j x(t-j)) \quad (1)$$

$$x(t) = f(u(t)) \quad (2)$$

While Wiener model can be described by the following equations:-

$$y(t) = f(x(t)) \quad (3)$$

$$x(t) = \sum_{i=1}^m (a_i x(t-i)) + \sum_{j=0}^n (b_j u(t-j)) \quad (4)$$

Where:-

m is the number of poles of the linear part.

n is the number of zeros of the linear part.

a_i and b_i are linear part coefficients.

Genetic algorithms (GAs) are a family of general stochastic search methods, which can be viewed as computational models of Darwinian evolution theory. They use the analogs of evolutionary operators on a population of states in a search space to find those states that optimize a fitness function. The search space consists of character strings of fixed or variable length (chromosomes or genotypes) composed of the elements of a given alphabet (alleles).

The genotype space is mapped onto another (phenotype) search space. The fitness function is defined as a function of a state in the phenotype space [8-10].

An implementation of a genetic algorithm begins with a population of typically random chromosomes. One then evaluates these structures and allocates reproductive opportunities in such a way that those chromosomes which represent a better solution to the target problem are given more chances to reproduce than those chromosomes which are poorer solutions. The solution goodness is typically defined with respect to the current population [11]

There are many identification techniques that have been used to identify the linear and nonlinear parts of the Hammerstein model and the Wiener model each alone, examples of these identification techniques are Marconato et al [4] who used the Support Vector Machines to identify the nonlinear systems of Wiener-Hammerstein systems based on input/output measurements. Sou et al [12] used a convex semi definite programming SDP relaxation to obtain a sub-optimal solution to non-convex quadratic programming that formulates the Wiener-Hammerstein models. Marconato et al [13] presented an identification of the Wiener-Hammerstein models by a learning from example approach SVM for regression on the basis of real life benchmark data and they used the genetic algorithm to select the best model that describe the input/output relationship. Wang et al [14] presented an identification of Wiener model by a recurrent neural network with the observer Kalman filter (OKID) algorithm for unknown dynamic nonlinear system identification. There are many papers used genetic algorithm principles for identification purposes, for example Lu et al [15] used a GP models to obtain the nonlinear function and parameters of Wiener model. Dotoli et al [16] described the GA to identify nonlinear SISO Hammerstein model, they assume a bounded but not a prior known order for linear part and the nonlinear part belongs to a known structure. Xie et al [17] used an iterative method of GA to get the Wiener model but they assume a priori knowledge of the objective system and the expected object linear system.

Other uses of GA for identification of Hammerstein model can be found at Al-Duawaish et al [18], Hachino et al [19,20], while using of GA for identification of Wiener model can be found in Vázquez et al [21].

In this work, we used iterative search method combined with directed search by GA to find the Wiener and Hammerstein models parameters and identify number of delays for both

input and output also determine a good approximation for the nonlinearity type of the system under consideration.

2. Proposed algorithm

As shown in Figure (1) the Wiener-Hammerstein model consists of two sub-models. It's well known that the genetic algorithm can easily identify the sub-models, especially if the inputs and outputs of the corresponding sub-systems are known, many papers assumed that the middle stages are known [17] so the identification demands are simplified. In this work, the problem assumes there is no prior knowledge of the middle stages, only the input signals and output responses of the systems under consideration are known.

The basic idea is to walk through a lookup Table that contains a list of number of delays for the input and output. It also contains some nonlinear relationships. After selection of a specific relationship, we run the GA to search for the parameters values.

The complete algorithm can be described in the following steps which consists of two parts that work simultaneously, walking through the lookup Table and running the genetic algorithm:-

a- Part 1 : The lookup Table

The lookup Table contains two columns, the first one describes the behavior of the output by number of delays and type of nonlinearity, the second one describes the behavior of the input by number of delays and type of nonlinearity. Its well know that the linear subsystem is included within the output delays while the nonlinear subsystem is included within the input signal [2,22]. In our experiments we included some nonlinearity within the output signal which describes the unexpected behaviors of the original system like the disturbance and noise.

The selection process is as follows:-

Step 1:- Assume we select the first row; then the plant equation will be:-

$$y(t) = ay(t - 1) + bu(t - 1) \quad (5)$$

Step 2:- Start the Genetic Algorithm Phase (part two) to find the coefficients values of Step 1, if the result is not satisfied then go to Step 3

Step 3:- Select the second row for the 1st column and 1st row for the 2nd column, then the plant equation will be:-

$$y(t) = a_1 y(t-1) + a_2 y(t-2) + bu(t-1) \quad (6)$$

Step 4:- Start the Genetic Algorithm Phase (part two) to find the coefficients values of Step 1, if the result is not satisfied then go to Step 5

Step 5:- Select the second row for the 1st column and 2nd row for the 2nd column, the plant equation will be:-

$$y(t) = a_1 y(t-1) + a_2 y(t-2) + b_1 u(t-1) + b_2 u(t-2) \quad (7)$$

Step 6:- Repeat these selection criteria until the plant estimation will satisfy the requirements or the lockup Table is finished.

Where

a_i and b_i are linear part coefficients

Figure (2) describes the complete programming flowchart of the proposed work.

Table (1). Lock up Table . Number of delays and nonlinear order and type of both inputs and outputs.

| Item No. | Number of delays of o/ps | Number of delays of i/ps or nonlinearity type |
|----------|--------------------------|---|
| 1 | y^{-1} | u^{-1} |
| 2 | y^{-2} | u^{-2} |
| 3 | y^{-3} | u^{-3} |
| 4 | y^{-4} | u^{-4} |
| 5 | $\frac{1}{1 + \exp(y)}$ | u^2 |
| 6 | $\frac{1}{1 + y}$ | u^3 |
| 7 | | $\frac{1}{1 + \exp(u)}$ |
| 8 | | $\frac{\exp(-u) - \exp(-u)}{\exp(-u) + \exp(-u)}$ |
| 9 | | Sin(u) |
| 10 | | Cos(u) |

b- Part 2 : Genetic algorithm

- a- Set the population size = Number of coefficients of the selected equation that describe the system.
- b- Create the initial population values, which are the coefficients of initial subsystem. Here we used the matlab function ' crtrp' that creates real-valued initial population.
- c- Evaluate the population fitness by using the mean square error between the actual output $y(n)$ and the estimated output $\hat{y}(n)$

$$E = \frac{1}{N} \sum_{n=1}^N (y(n) - \hat{y}(n))^2 \quad (8)$$

Where: - N number of samples

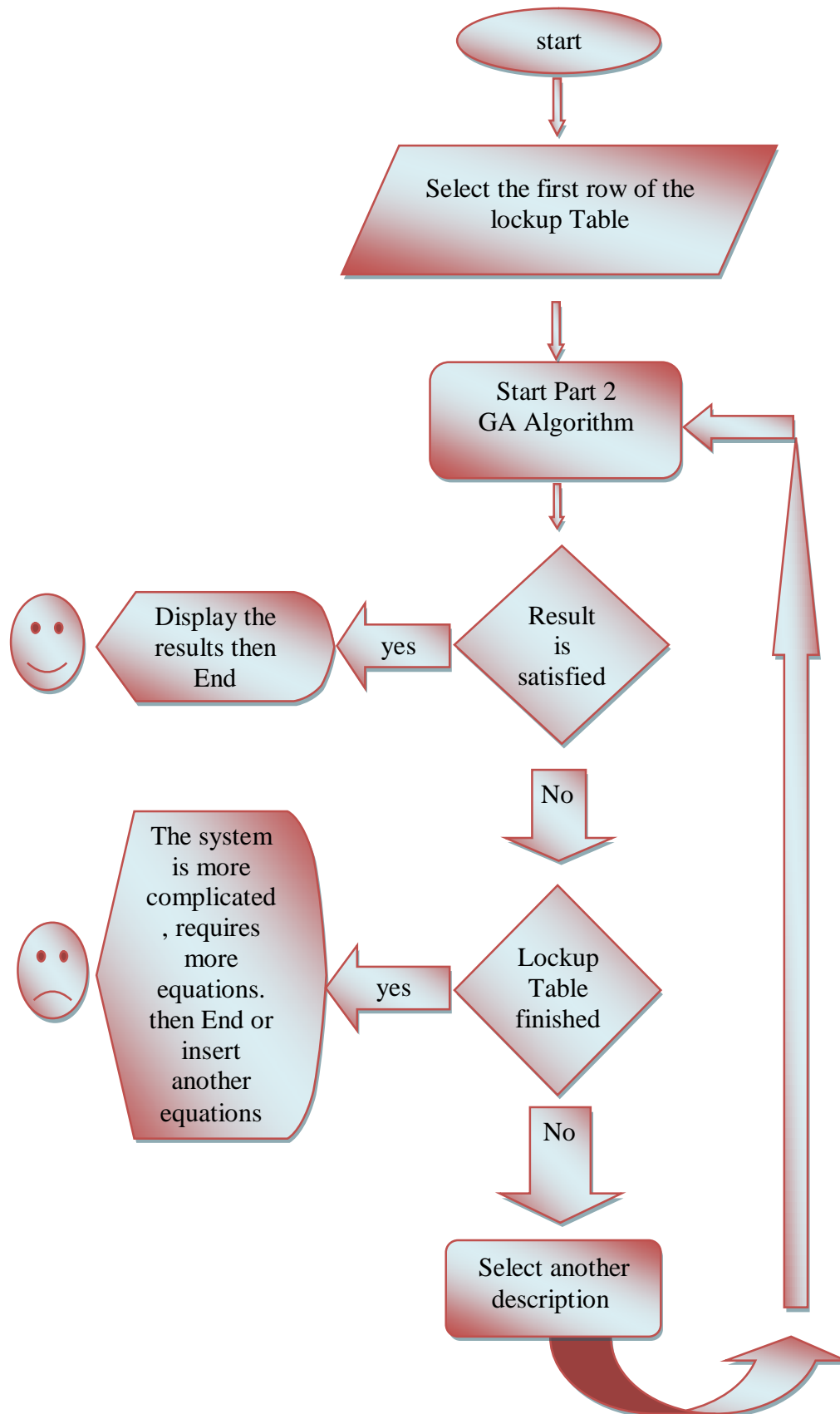
- d- If E is equal or less than the satisfying error then the description of the system is fixed.

else

- i. Do the selection process to select the winning parents, which is the roulette wheel.
- ii. Do the crossover process to get the offspring , we used the single point crossover method.
- iii. Go to step c until number of iterations is reached or step d is true.

For an efficient programming, we use the matlab functions that deals with genetic algorithms which are :-

- 1- 'gaoptimset' that creates genetic algorithm options structure, and
- 2- 'ga' that implements the genetic algorithm at the command line to minimize an objective function.

**Figure (2). Proposed work flowchart.**

3. Experimental results

To show the validity of the proposed algorithm many system are considered with different types:-

1- Plant 1:- Simple linear system

$$y(t) = a_1y(t-1) + a_2y(t-2) + bu(t-1) \quad (9)$$

The actual values of coefficients are:-

$$a_1=0.4;$$

$$a_2=0.35; \text{ and}$$

$$b=0.8$$

After running the proposed algorithm, we used 1500 generations with 100 population sizes for the GA we found the following system:-

$$y(t) = a_1y(t-1) + a_2y(t-2) + bu(t-1) \quad (10)$$

$$a_1= 0.4050;$$

$$a_2=0.3485; \text{ and}$$

$$b_1=0.801$$

Which gave a good description for both the two sub systems as shown in Figures (3), (4), and (5).

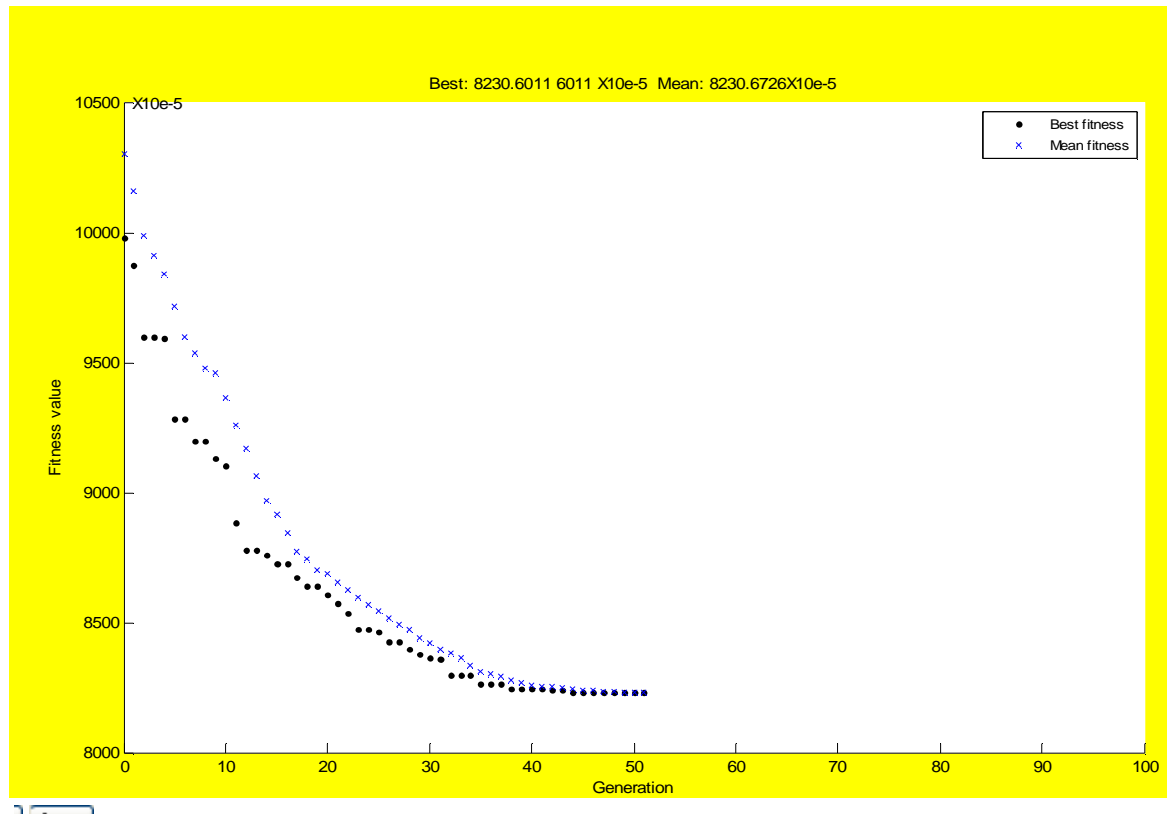


Figure (3). Genetic algorithm fitness values.

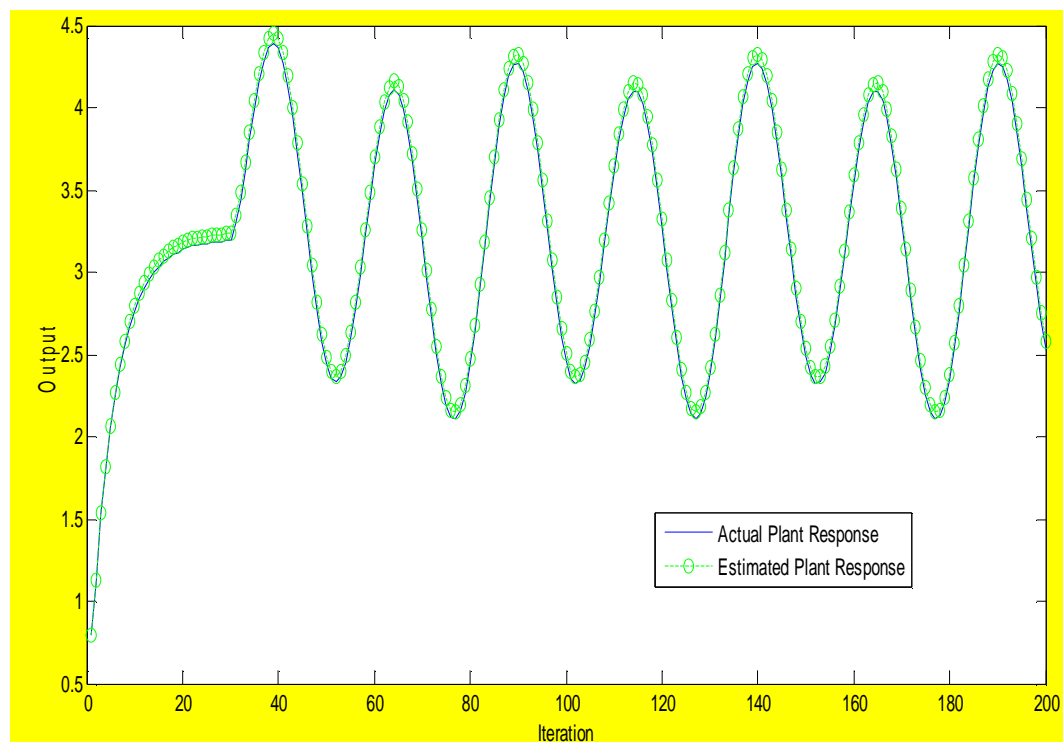


Figure (4). Actual and estimated plant output response.

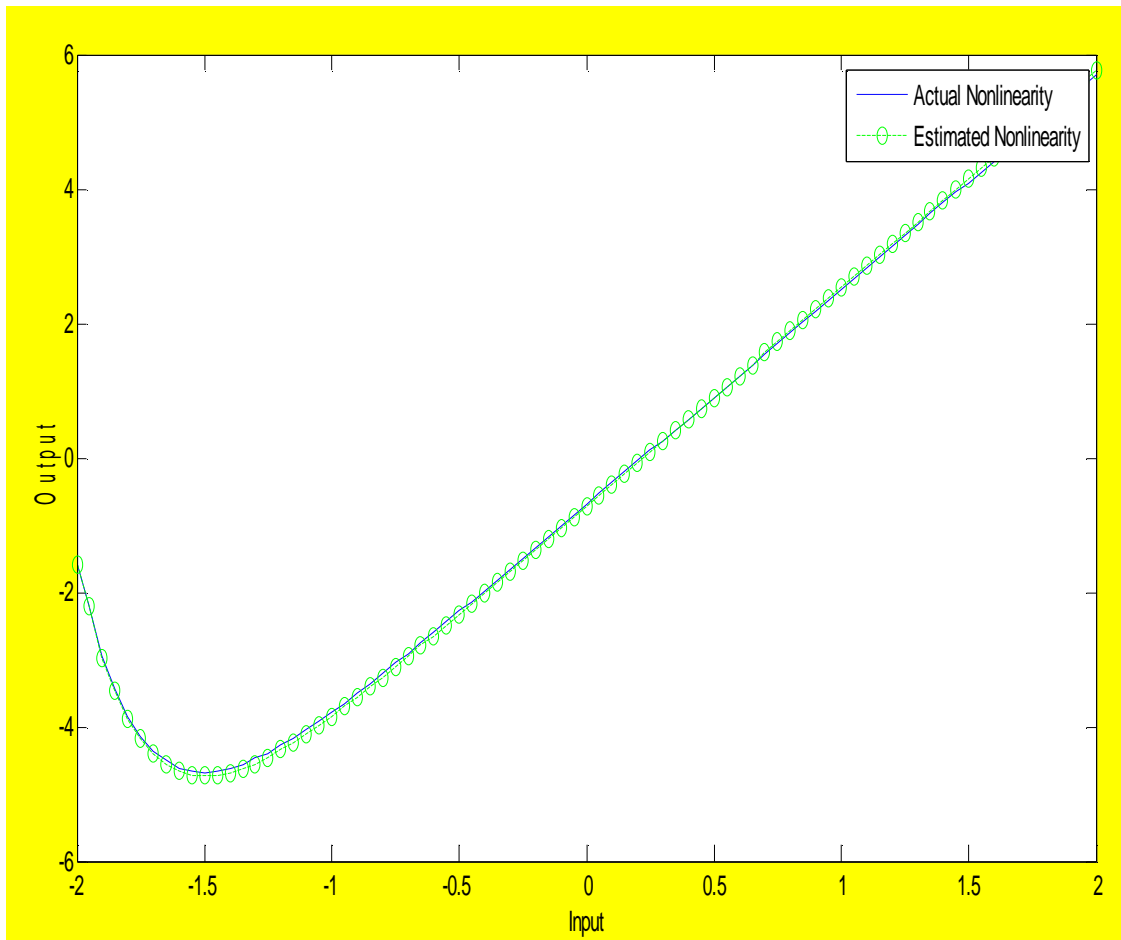


Figure (5). Nonlinearity behavior of the estimated system.

2- Plant 2:- which is 3rd order nonlinear system :-

$$y(t) = \frac{a y(t-1)}{1+y(t-1) * y(t-1)} + b x(t) \quad (11)$$

$$\text{and} \quad x(t) = (u(t-1))^3 \quad (12)$$

The real values are $a=1$ and $b=1$;

After running the proposed algorithm we found the following plant equation:-

$$y(t) = \frac{a y(t-1)}{1+y(t-1) * y(t-1)} + b x(t) \quad (13)$$

and $x(t) = (u(t-1))^3$ (14)

And estimated values are:-

$$a=1.0026$$

$$b=0.9954$$

Figures (6), (7), and (8) show the estimated and real plant equations behavior:-

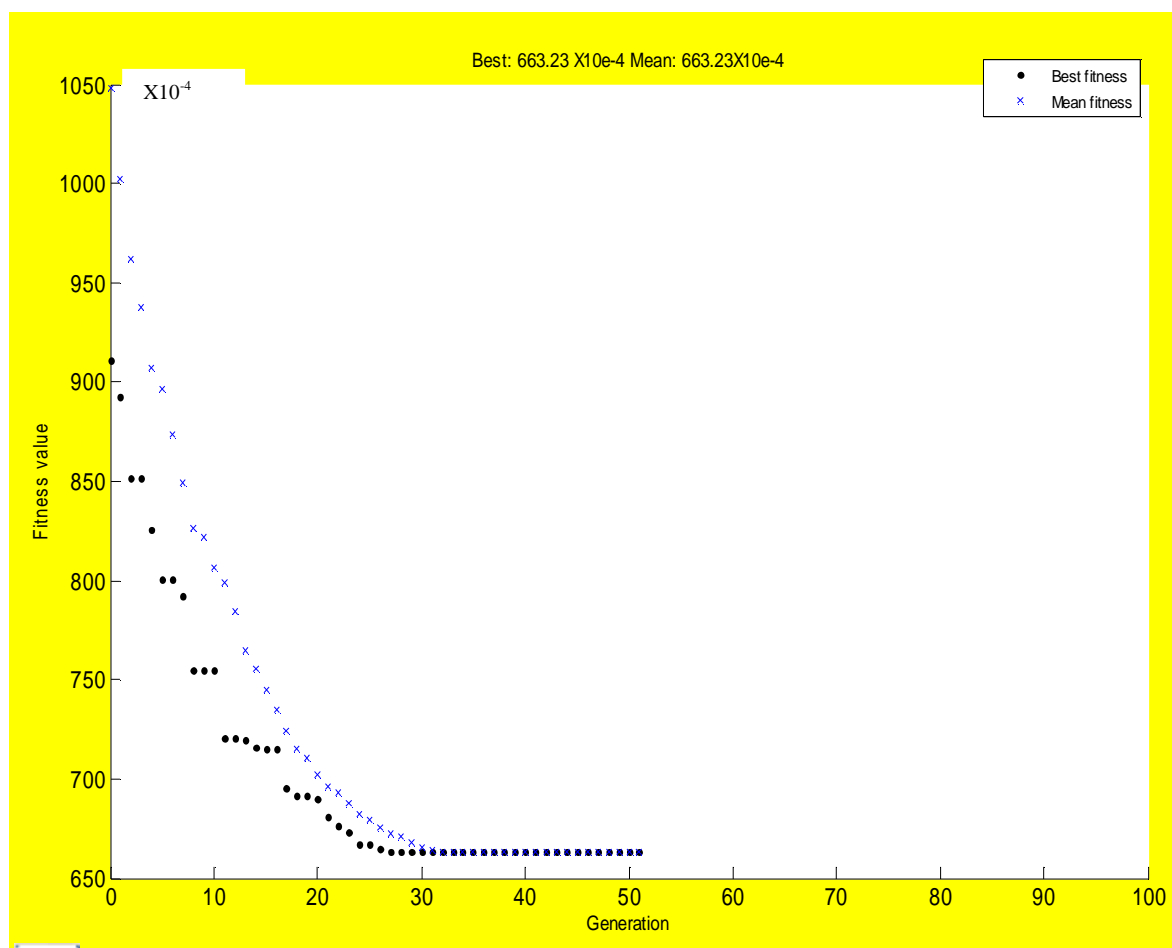


Figure (6). Genetic algorithm fitness values.

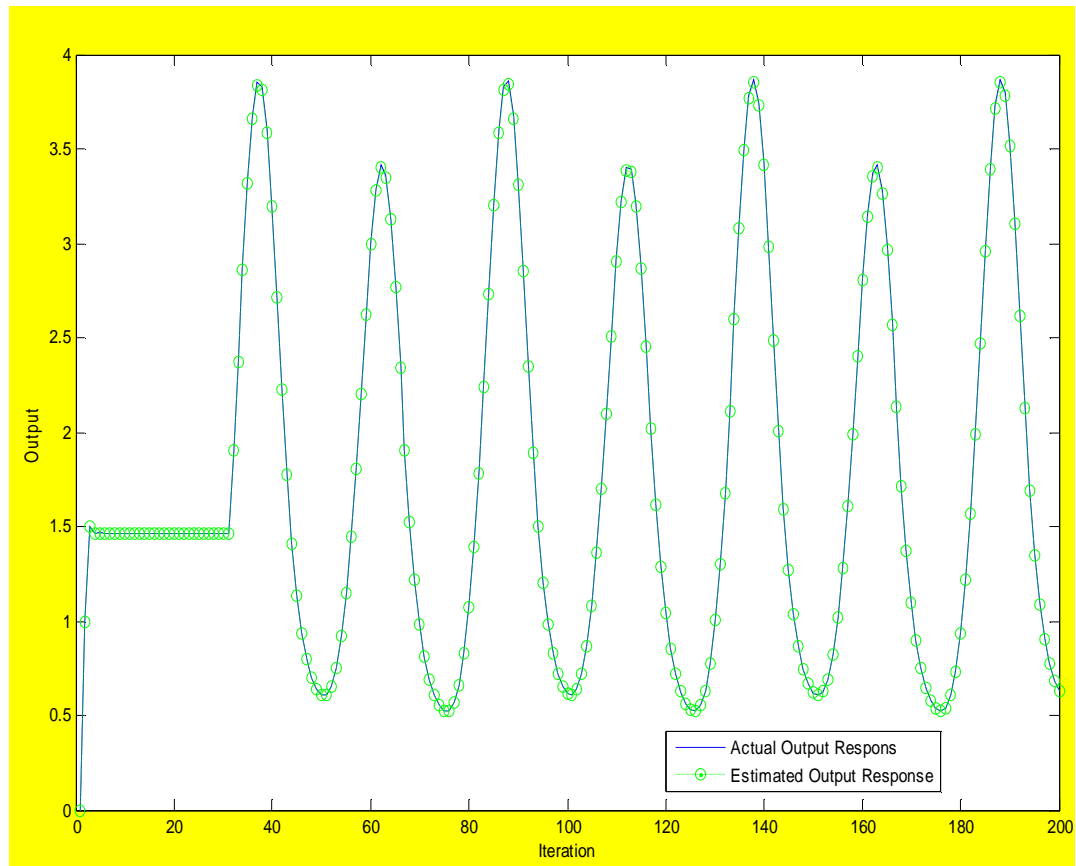


Figure (7). Actual and estimated plant output response.

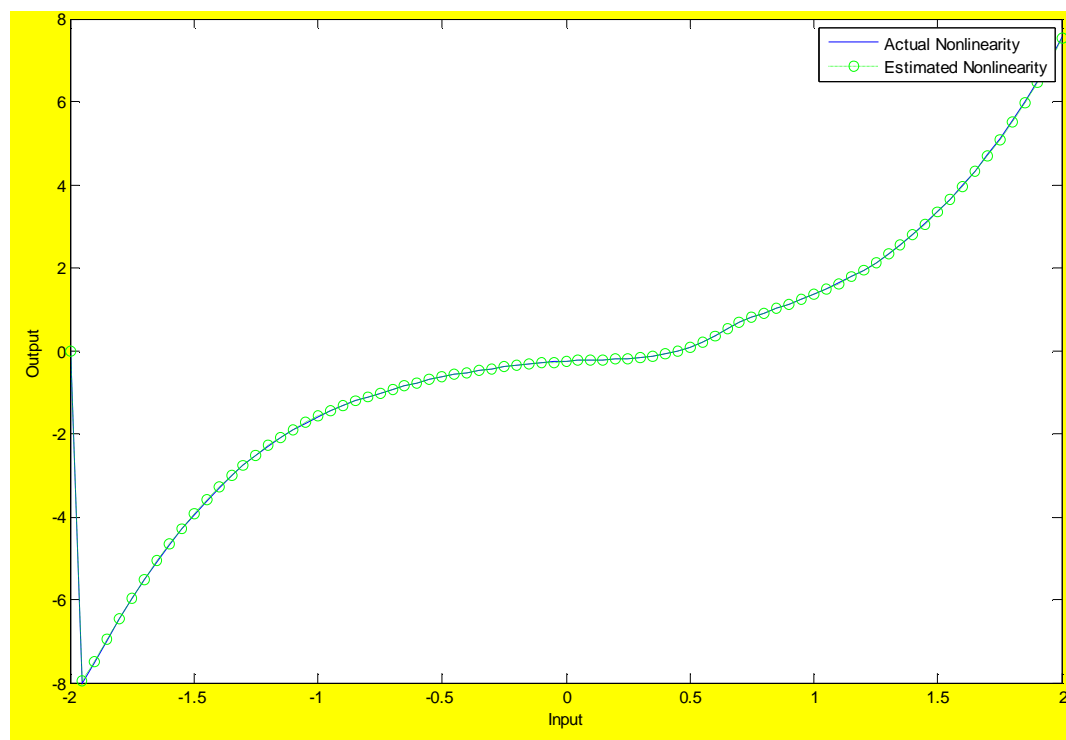


Figure (8). Nonlinearity behavior of the estimated system.

3- Plant 3:-

$$y(t) = a_1 y(t-1) + a_2 y(t-2) + a_3 y(t-3) + b_1 x(t-1) + b_2 x(t-2) \quad (15)$$

$$x(t) = \cos(3 * u(t)) + \exp(-u(t)) \quad (16)$$

The real values are

$$a_1 = 0.4;$$

$$a_2 = 0.35;$$

$$a_3 = 0.1;$$

$$b_1 = 0.8;$$

$$b_2 = -0.2.$$

The estimated ones are:-

$$y(t) = a_1 y(t-1) + a_2 y(t-2) + a_3 y(t-3) + b_1 x(t-1) + b_2 x(t-2) \quad (17)$$

$$x(t) = \cos(2.8 * u(t)) + \exp(-u(t)) \quad (18)$$

$$a_1 = 0.387$$

$$a_2 = 0.361$$

$$a_3 = 0.08976$$

$$b_1 = 0.07856$$

$$b_2 = -0.17878.$$

The validity is shown in figures (9), (10), and (11).

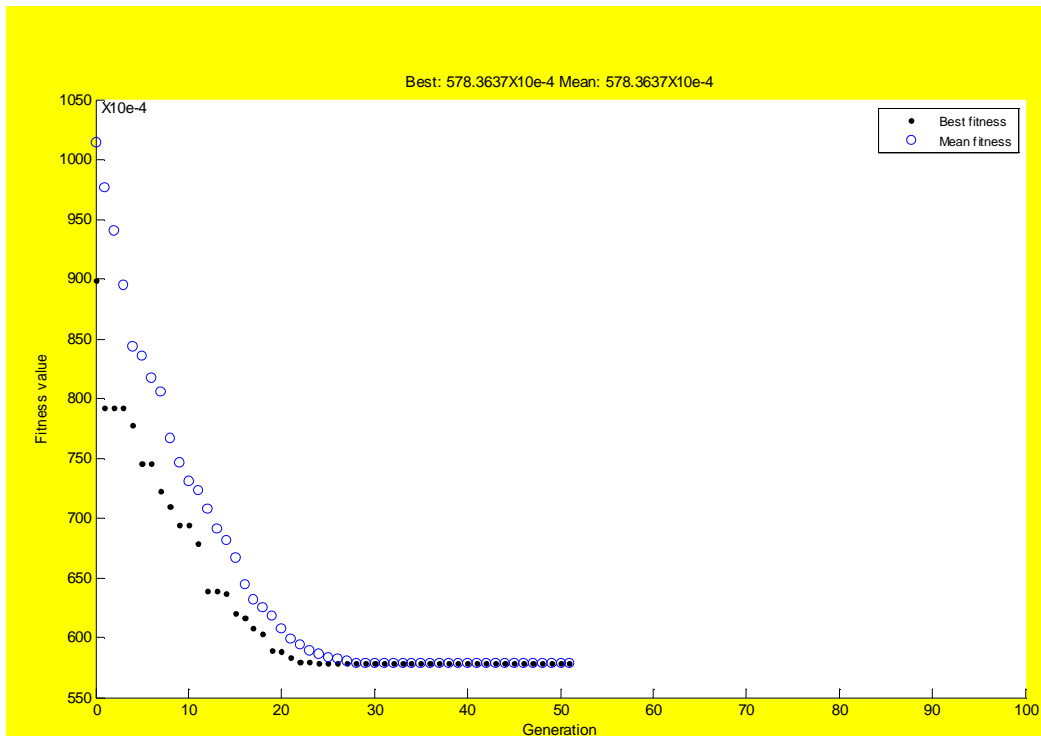


Figure (9). Genetic algorithm fitness values.

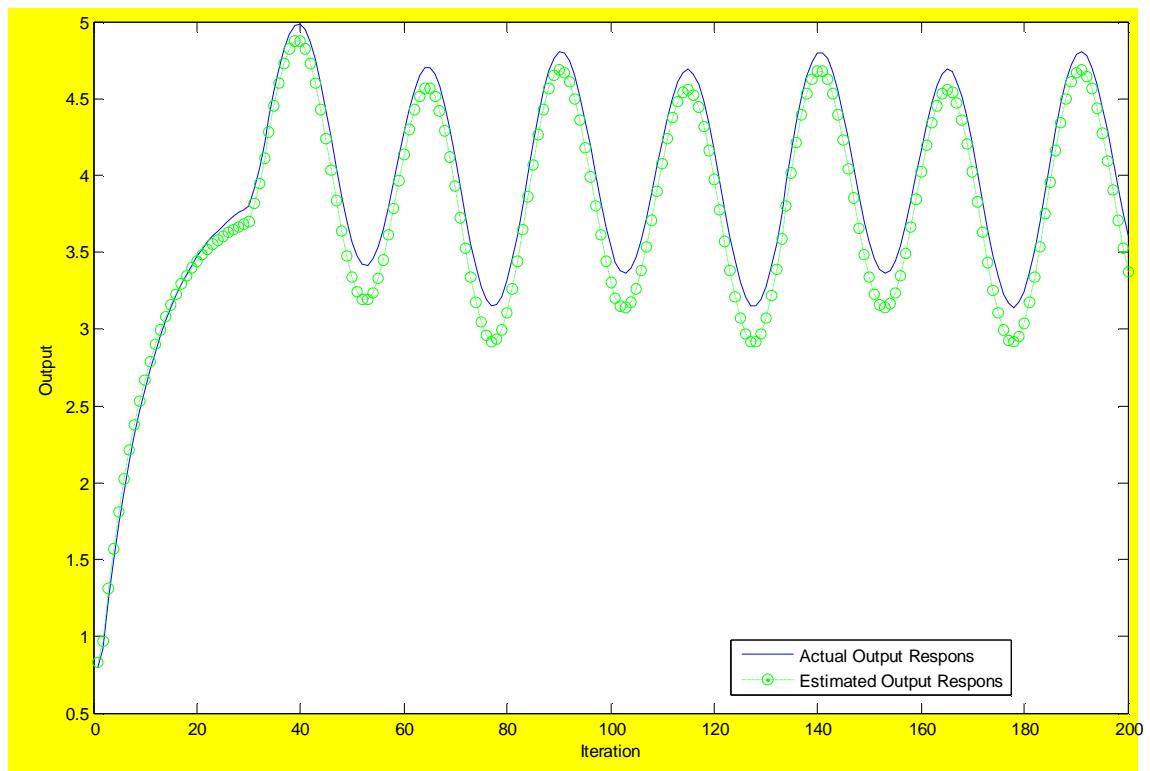


Figure (10). Actual and estimated plant output response.

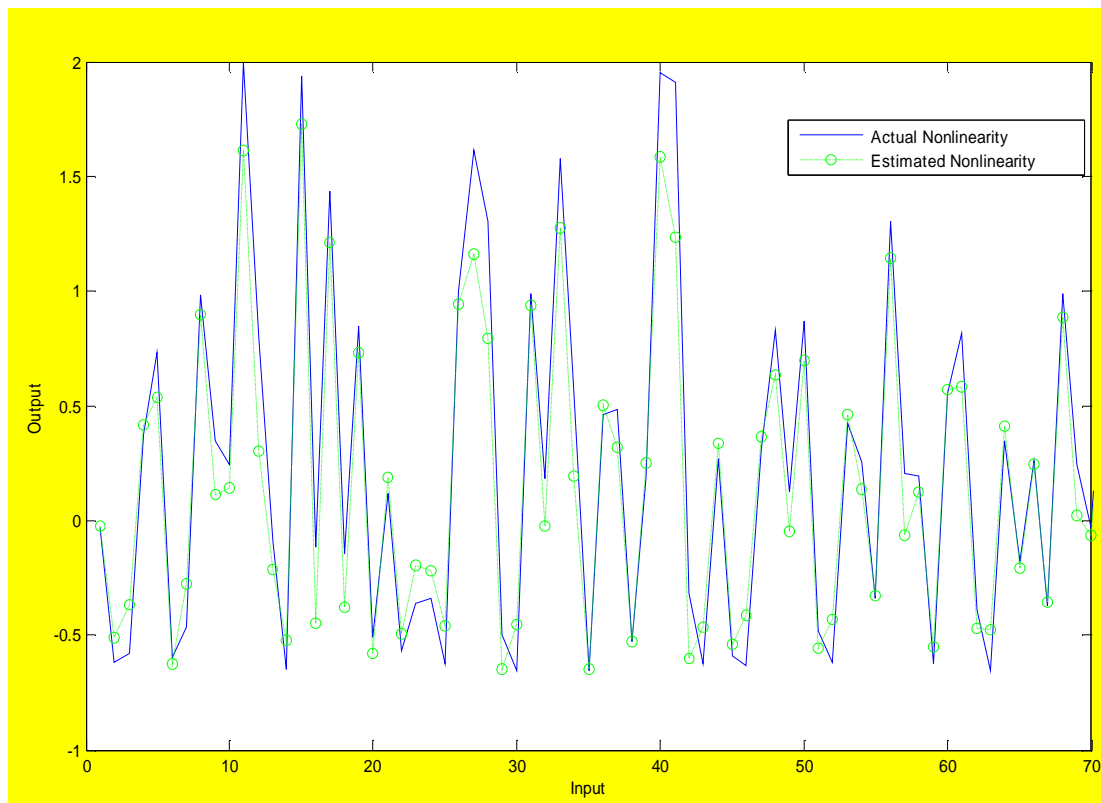


Figure (11). Nonlinearity behavior of the estimated system.

4- Conclusions

This work proposed a new method for identification of both Hammerstein and Wiener models. From the given examples of different nonlinearities systems which describe the real life plants, the results show that the proposed work is immune to noise and can be applied to real- time plants identification.

One can increase the reliability of this work by introducing more functions that describe real systems as well as using state space approach.

5- References

- [1] Ioan D. Landau and Gianluca Zito, " Digital Control Systems Design, Identification and Implementation", Springer-Verlag London Limited 2006.
- [2] Sayed Saad Azhar Ali, "Identification of Hammerstein and Wiener Models using radial basis functions neural networks", Msc Thesis in Electrical Eng. , King Fahad University of Petroleum and Minerals, Dhahran, Saudi Arabia, Dec. 2001.
- [3] Al-Duwaish H. and Naeem, Wasif, "Nonlinear Model Predictive Control of Hammerstein and Wiener Models Using Genetic Algorithms", I E E E, Proceedings of the 2001 IEEE

- International Conference on Control Applications,
http://isi.kfupm.edu.sa/proceedings/pdf/N/nonlinear_model_predictive_control_of_ha_al_duwaish_isip_000173316300082.pdf
- [4] Anna Marconato¹, Andrea Boni¹, Dario Petri¹, and Johan Schoukens²; "Nonlinear system identification by means of SVMs: choice of excitation signals", www.imeko.org/publications/tc4-2008/IMEKO-TC4-2008-152.pdf.
- [5] Anna Marconato, Johan Schoukens, "Identification of Wiener-Hammerstein Benchmark Data by Means of Support Vector Machines", 15th IFAC Symposium on System Identification Saint-Malo, France, July 6-8, 2009, <http://www.tw.vub.ac.be/elec/Papers%20on%20web/Papers/AnnaMarconato/IFAC-SYSID09-Marconato-Identification.pdf>.
- [6] R. Bhushan Gopaluni, Thomas B. Schön, and Adrian G. Wills, "Particle Filter Approach to Nonlinear System Identification under Missing Observations with a Real Application", www.control.isy.liu.se/~schon/Publications/GopaluniSW2009.pdf
- [7] Kin Cheong Sou, Alexandre Megretski and Luca Daniel, "Convex Relaxation Approach to the Identification of the Wiener-Hammerstein Model", institutes.lanl.gov/isti/isami/papers/cdc2008_WH.pdf
- [8] John R. Koza, "Genetic Programming On the Programming of Computers by Means of Natural Selection", A Bradford Book The MIT Press London, England, Sixth printing, 1998.
- [9] John S. Gero and Vladimir Kazakov, "A Genetic Engineering Volume 9, Number 1, 2001 by the Massachusetts Institute of Technology.
- [10] Randy L. Haupt and Sue Ellen Haupt, "PRACTICAL GENETIC ALGORITHMS", A JOHN WILEY & SONS, INC., PUBLICATION, second edition 2004.
- [11] Darrell Whitley, "A Genetic Algorithm Tutorial", www.stat.ucla.edu/~yuille/courses/Stat202C/ga_tutorial.pdf
- [12] Kin Cheong Sou, Alexandre Megretski and Luca Daniel, "Convex Relaxation Approach to Identification of the Wiener-Hammerstien Model", In proceedings of the 47th IEEE Conference on Decision and Control, December 2008, ieeexplore.ieee.org/xpls/abs_all.jsp?arnumber=4739417
- [13] Anna Marconato and John Schoukens, "Identification of Wiener-Hammerstein Benchmark Data by Means of Support Vector Machines", 15th IFAC symposium on system identification Saint-Malo, France, July 6-8, 2009.

- [14]Jeen-Shing Wang and Yu-Liang Hsu, "Dynamic nonlinear system identification using a Wiener-type recurrent neural network with OKID algorithm", Journal of Information Science and Engineering, 24, 891-905, 2008.
- [15]Yueh-Chun Lu, Ming-Hung Chang and Te-Jen Su," Wiener Model Identification using Genetic Programming", Proceeding of the International MultiConference of Engineers and Computer Scientists 2008 Vol II, IMECS 2008, 19-21 March, 2008, Hong Kong.
- [16]Mariagrazia Dotoli, Guido Maione, Davide Naso and Biagio Turchiano, " Genetic Identification of Dynamical System with Static Nonlinearities",
- [17]Changsong Xie and Xuhui Li, "An algorithm using genetic programming for the compensation of linear distortion based on Wiener system model", Facta Universitatis (NIŠ), Elect. Eng. Vol 17, Aug 2004, 219-229.
- [18]Tomohiro Hachino, Kenji Shimoda and Hitoshi Takata, "Hybrid algorithm for Hammerstein system identification using genetic algorithm and particle swarm optimization", World academy of Science, Engineering and Technology 53, 2009.
- [19]Al-Duwaish H and Naeem Wasif, "Nonlinear model predictive control of Hammerstein and Weiner models using genetic algorithms", Proceedings of the 2001 IEEE International Conference on Control Applications,
<http://citeseerx.ist.psu.edu/viewdoc/download?doi=10.1.1.2.3177&rep=rep1&type=pdf>.
- [20]Tomohiro Hachino, Katsuhisa Deguchi and Hitoshi Takata, " Identification of Hammerstein model using Radial basis function networks and genetic algorithm", Proceedings of the 5th Asian Control Conference 2004,
ascc2004.ee.mu.oz.au/proceedings/papers/P18.pdf
- [21]K. Rodriguez- Vázquez and P.J. Fleming, "Multi-objective genetic programming for nonlinear system identification", Electronics Letters, 30th April, 1998, Vol 34, No. 9.
- [22]Sayed Zeeshan Rizvi, " A new method for identification of MIMO Hammerstein model", Msc Thesis in Electrical Eng., King Fahad University of Petroleum and Minerals, Dhahran, Saudi Arabia, June 2008.

Performance of Sensitivity of Direct Detection Optical Receiver Incorporating MOSFET-Based Transimpedance-Type Amplifier

Abdulgaffar Swailim Muhawwis

Electrical & Electronic Department

College of Engineering

Thi-Qar University

Abstract

Metal-Oxide-Semiconductor Field-Effect Transistors (MOSFETs) offer many advantages due to their low noise and high associated gain at microwave frequencies. Therefore, they are well suited to the amplifier requirements of broadband light-wave receivers, through providing a high dynamic range and wide bandwidths.

In this work, the performance of integrated optical receiver consisting of PIN-photodiode and MOSFET-based transimpedance type amplifier is analyzed. The effect of various device parameters on receiver performance is investigated in details. The simulation results show that the sensitivity (P_{sen}) of an optical receiver is approximately constant if it is based on well-designed MOSFET.

Keywords : MOSFET, transimpedance amplifier, optical receiver, sensitivity, optical receiver noise, transconductance.

المستخلص

توفر ترانزستورات الموسفيت عدة مزايا وذلك لما تتمتع به من كسب عالٍ وضوضاء قليلة في حزمة الترددات المايكروية. وللمزايا آنفة الذكر فإنها تكون ملائمة للمكبرات المستخدمة في المستلمات الضوئية من خلال توفيرها مدى ديناميكي عالي ضمن نطاق ترددي واسع. تم خلال هذا البحث تحليل أداء المستلمات الضوئية المكونة من ثنائي ضوئي نوع بي-آي-أن ومكبر إشارة مبني على أساس ترانزستورات الموسفيت. تم بحث تأثير تغير معلمات الجهاز المذكور على الأداء بشكل تفصيلي. بينت نتائج المحاكاة بأن حساسية المستلم الضوئي تكون ثابتة تقريباً إذا تم تصميم ترانزستور الموسفيت بشكل جيد.

1. Introduction

The optical receiver is an optoelectronic device that recovers the transmitted electrical signal from the incident light wave signal. It is formed principally from a photo detector (photodiode or photoconductor), cascaded to a FET-based amplifier. Two photodiodes are mainly used in optical receiver design namely PIN photodiode and avalanche photodiode (APD). Theoretical sensitivities for both PIN/FET and APD/FET direct-detection receivers are shown in Figure (1) [1].

It is clear that the APD is attractive because of its superior sensitivity in APD/FET receivers. On the other hand, it is difficult to achieve significantly higher bandwidths in APD receivers, because of the avalanche build-up limitation, which could restrict the use of APDs in multigigabit systems [1]. PIN photodiodes have no such limitation, and bandwidth as high as 38 GHz has been reported [2]. Further, the PIN photodiode is preferred to APD because of the absence of excess multiplication noise.

MOSFETs based on AlGaAs/InGaAs structure offer many advantages due to their low noise [3], and high associated gain at microwave frequencies [1]. Therefore, they are well suited to the preamplifier requirements of broadband lightwave receivers.

It is also expected that the monolithic integration of optical and electronic components on the same chip will alternatively lead to ultra-high speed, high sensitivity, reliability, and low cost [4, 5]. Most of wide band optical receivers have been fabricated by integrating a PIN photodiode for light detection [3], and a transimpedance amplifier for electronic signal amplification and impedance matching [6].

In this work the performance of a monolithically integrated optical receiver consisting of a PIN photodiode and an MOSFET-based transimpedance type preamplifier is analyzed.

2. Optical receiver

2.1 Device description

In this analysis, the optical receiver considered consists of an InGaAs PIN photodiode integrated with a single gain stage transimpedance amplifier as shown in Figure (2). Such a preamplifier design provides a wide bandwidth and high dynamic range, which is defined as the range of input power levels over which the bit error rate is acceptable [7]. Note that all of the loads in the circuit are active to allow circuit integration with the other MOSFETs and to reduce device area and overall power dissipation. A conventional feedback resistor is replaced by a transistor (Q_3) with an equivalent output resistance R_F . The use of a FET feedback may reduce parasitic shunt capacitance, thereby resulting in a wide bandwidth operation.

2.2 Receiver noise sources

The noise current of a receiver consists of low frequency (LF) noise, thermal noise in the feedback resistor, FET channel noise, and shot noise due to the leakage in the FET gate and the detector. These various noise contributions in an optical receiver are given by [5, 7]:

$$S_{sh} = \sqrt{2q(I_{Dark} + I_{leak})I_2B} \quad (1)$$

$$S_{ch} = 4pC_T B \sqrt{\frac{kT\Gamma I_3 B}{g_m}} \quad (2)$$

$$S_{LF} = 4pC_T B \sqrt{\frac{2kT\Gamma f_c I_f}{g_m}} \quad (3)$$

$$S_{th} = 2 \sqrt{\frac{kT I_2 B}{R_F}} \quad (4)$$

Here, σ_{sh} , σ_{ch} , σ_{LF} , and σ_{th} are the shot noise, channel noise, low frequency (LF) noise, and thermal noise standard deviations respectively, q is the electronic charge, k is the Boltzmann constant, g_m is the extrinsic transconductance, I_{Dark} is the PIN dark current, I_{leak} is the gate leakage current, B is the data bit-rate, T is the temperature, Γ is the MOSFET noise Figure (≈ 1.6 [5]), f_c is the LF corner frequency, and C_T is the total front-end capacitance. C_T is calculated as:

$$C_T = C_{st} + C_{PD} + C_{GS} \quad (5)$$

where, C_{st} is the input stray capacitance, C_{PD} is the PIN diode capacitance, and C_{GS} is the MOSFET gate-source capacitance. Furthermore, I_f , I_2 , and I_3 are effective receiver bandwidth integrals which depend on the transfer function of the circuit and the input and output waveforms. Here a raised cosine output pulse response of the receiver for a rectangular pulse shape, and a NRZ data format are assumed.

2.3 Receiver sensitivity

The receiver sensitivity is expressed in terms of minimum, time-averaged incident optical power (P_{sen}), which can be detected for a given acceptable bit error rate (BER). Assuming Gaussian noise statistics, the sensitivity is given by [7]:

$$P_{sen} = \left(\frac{Qhf}{hq} \right) S_T \quad (6)$$

where, $Q=6$ for $BER=10^{-9}$, h is Planck constant, f is the frequency of the incident light, η is the overall efficiency in converting the incident optical power into a signal current, and σ_T is the total noise standard deviation which is defined as:

$$S_T = \sqrt{S_{sh}^2 + S_{ch}^2 + S_{LF}^2 + S_{th}^2} \quad (7)$$

Receiver sensitivity can be improved by decreasing the impedance at the interface. However, the low impedance at the PD-amplifier interface is highly non-optimal from a noise point of view, which, together with the intrinsic noise Figure of the amplifier, limits receiver sensitivity. The monolithic integration of transimpedance receiver is expected to be one of the facial ways to realize high sensitivity optoelectronic integrated circuits (OEICs) [8].

3. Transimpedance amplifier

The equivalent circuit of the PIN/transimpedance amplifier is shown in Figure.(3), where R_{in} is the input resistance of the amplifier, C_F is the stray capacitance of the feedback resistor R_F , and A is the amplifier voltage gain, and I_{ph} is the PIN diode photocurrent.

The response of the receiver is represented by the transimpedance Z_T , which is the ratio of the output voltage to the input photocurrent. The frequency dependence of Z_T is given by:

$$Z_T(f) = \frac{-AR_{in}R_F/[R_F + (1+A)R_{in}]}{1 + j\frac{2\pi fR_{in}R_F}{R_F + (1+A)R_{in}}[C_T + (1+A)C_F]} \quad (8)$$

Let Z_{T0} be the DC transimpedance, and f_{3dB} is the cutoff frequency (-3dB point), then:

$$Z_{To} = \frac{-AR_{in}R_F}{R_F + (1+A)R_{in}} \quad (9)$$

and

$$f_{3dB} = \frac{1}{2p \left[\frac{R_{in}R_F}{R_F + (1+A)R_{in}} [C_T + (1+A)C_F] \right]} \quad (10)$$

Due to the use of equalization stage [8] in the receiver, the noise due to the intersymbol interference (ISI) is not considered [7]. So that, Eqn.(10) is useful in determining the bandwidth of the system.

In order to achieve the operation of the bit-rate (B) without equalization, the bandwidth of the preamplifier should be at least equal to the effective noise bandwidth of the receiver (I2B). To accomplish this, RF must be adjusted such that f3dB is equal to the effective bandwidth. Let $A \gg 1$ and $AR_{in} \gg R_F$, Eqn.(10) can be simplified as:

$$f_{3dB} = [2pR_F(C_F + C_T/A)]^{-1} \quad (11)$$

then

$$R_F = [2pI_2B(C_F + C_T/A)]^{-1} \quad (12)$$

This choice of RF ensures that thermal noise (Eqn.(4)) is not excessive, although it also implies a negligible intersymbol interference (ISI) noise. Figures(4a-4d) display the variation of different receivers noise sources as a function of B. Unless otherwise stated, the parameter values used in the simulation are listed in Table (1). The solid and dotted lines correspond, respectively, to the presence or absence of the equalization stage. It is clear that thermal and shot noises decrease in the absence of equalization. At B=10 Gbit/s, the thermal noise reduces to 0.075 of its value when equalization exists. This to be compared with 0.91 reduction for shot noise. So that, the thermal noise reduction is more important than that of the shot noise. The channel and LF noise behave in an opposite manner. However, at the same bit-rate, the channel noise and LF noise increase by factors of 1.4 and 2.08, respectively. As a result of not employing an equalization stage, the total noise current decreases to 0.107 of its value at equalization for 10 Gbit/s bit-rate. This is clear from Figure (5) where the total noise is plotted as a function of bit-rate.

In Figure (6), RF that satisfies the condition of negligible intersymbol interference is plotted as a function of the bit-rate. Note that $R_F \approx 600 \Omega$ is required for B=10 Gbit/s. The dependence of receiver sensitivity on bit-rate is depicted in Figure (7). Note that Psen (in dBs)

decreases linearly with the logarithm of the bit-rate. For example, increasing B from 1 Gbit/s to 10 Gbit/s degrades the receiver sensitivity by 5 dB.

4. Receiver performance

To calculate the performance of the optical receiver, a MOSFET with parameter values given in Table (2) are assumed. Other parameters used in this analysis are listed in Table (1). The MOSFET performance such as g_m , C_{GS} , and C_{GD} are determined from expressions derived in [9].

Recall that the MOSFET capacitance and transconductance are functions of structure parameters of the device. Therefore, it is expected that the sensitivity of MOSFET-based receivers vary with transistor structure parameters. However, the simulation results reveal that this fact loses its importance when

- (i) C_{GS} is kept much lower than $(C_{PD}+C_{st})$; or
- (ii) The total front-end capacitance to transconductance ratio (C_T/g_m) is small. In other words, the operation speed of the MOSFET is much greater than the bit-rate.

Using the parameters listed in Tables (1) and (2), the PIN/MOSFET optical receiver sensitivity is plotted in Figure (8) as a function of CT for different values of g_m . The results in this Figure indicate clearly that the receiver sensitivity is less affected by the variation of CT when CT is small and this effect is more pronounced when g_m is high. For example, $P_{sen} = -21.17$ dBm when CT is less than 500 fF and $g_m = 800$ mS. For the receiver under consideration, the values of CT and g_m are 290 fF and 216 mS respectively. These values lead to -21.12 dBm receiver sensitivity. The simulation results indicate that P_{sen} is almost independent of the variation of MOSFET structure parameters. In fact, P_{sen} is almost independent of bias conditions (V_{GS} and V_{DS}) as shown in Table (3).

Figure (9a-9e) show, respectively, the effect of varying gate width (W), gate length (L_g) oxide layer thickens (di), semiconductor layer thickens (dd), and doping concentration (Nd) on receiver sensitivity. Investigating these Figures highlights the following facts:

- (i) For optical consideration, the optical receiver sensitivity is almost independent of gate width.
- (ii) There is a negligible degradation in P_{sen} (≈ 0.1 dBm) as a result of increasing L_g from 20 to 100 nm.
- (iii) Increasing the oxide layer thickness from 1 to 100 Å improves the sensitivity by only 1 dB.

- (iv) P_{sen} remains almost unchanged by increasing the semiconductor layer thickness from 10 to 130 Å.
- (v) There is no remarkable dependence of P_{sen} on the doping concentration of the MOSFET semiconductor layer doping (N_d).

To improve the receiver sensitivity slightly, the source resistance (R_s) must be minimized since the intrinsic transconductance, which inversely proportional to the total noise current, increases with minimizing R_s . Figure (10) depicts the effect of R_s on receiver sensitivity. Reducing R_s from 30 Ω to 0 Ω improves the P_{sen} by only 0.3 dB.

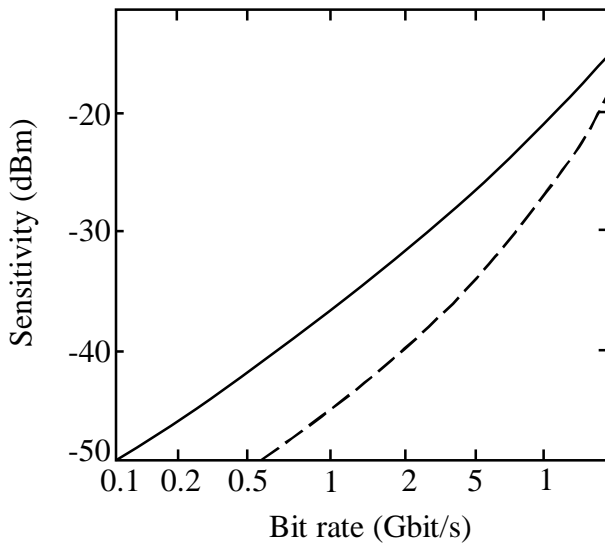
5. Conclusion

We analyze the performance optical receiver consisting of PIN-photodiode and MOSFET-based transimpedance type amplifier by investigating the effect of various device parameters on receiver performance. The simulation results show that the sensitivity (P_{sen}) of an optical receiver approximately independent of gate width, degrade negligibly with the increase of the gate length, enhanced with the increase of oxide layer thickness, and approximately it has no change with semiconductor layer thickness and doping concentration.

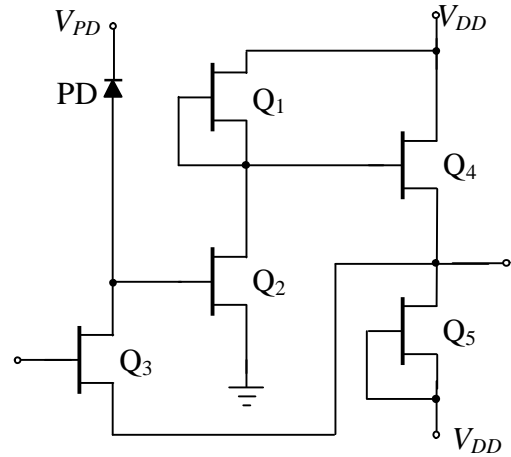
6. References

- [1] C. H. Chen and M. J. Deen, Aug. 2002, "Channel Noise Modeling of Deep Submicron MOSFETs," IEEE Trans. Electron Devices, vol. 49, pp. 1484–1487.
- [2] H. Shin, J. Jeon and S. Kim, September, 2006 "Analytical Thermal Noise Model of Deep Submicron MOSFETs," Journal of Semiconductors Technology and Science, vol. 6, No. 3.
- [3] B. Claflin, E. R. Heller, and B. Wenningham, May 18th-21st, 2009, "Accurate Channel Temperature Measurement in GaN-based HEMT Devices and its Impact on Accelerated Lifetime Predictive Models," CS MANTECH Conference, Tampa, Florida, USA.
- [4] Claudiu AMZA, Ovidiu-George PROFIRESCU, Ioan CIMPIAN, Marcel D. PROFIRESCU, 2008, "Monti Carlo Simulation of a HEMT Structures," Proceedings of The Romanian Academy of The Romanian Academy, Volume 9, Number 2.
- [5] Mustafa EROL, "Effect of Carrier Concentration Dependant Mobility on the Performance of High Electron Mobility Transistors," Turk J Phy, 25 (2001), 137 - 142.

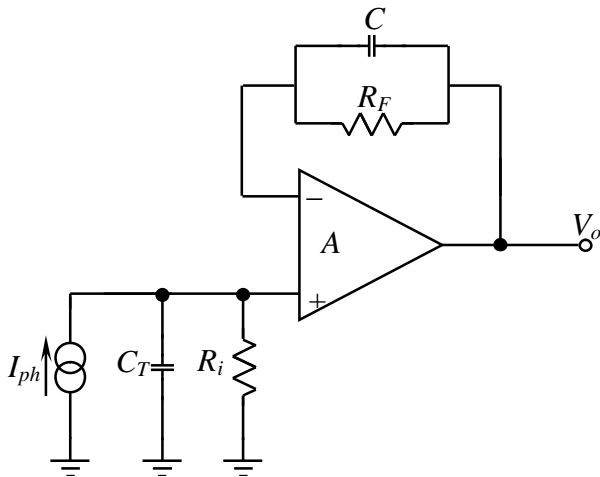
- [6] Wen-Chau Liu, Wen-Lung Chan, Wen-Shiung Lour, Kuo-Hui Yu, Chin-Chuan Cheng, and Shiou-Yinh Cheng, 2001 , “Temperature-dependence investigation of a high performance inverted delta-doped V-shaped GaInP/In_xGa_{1-x}As/GaAs pseudomorphic high electron mobility transistor,” IEEE Trans. Electron Devices, vol. 38, no. 7, pp. 1290-1296,.
- [7] D. C. W. Lo, and S. R. Forrest ,June 1989, “Performance of In_{0.53}Ga_{0.47}As and InP junction field effect transistors for optoelectronic integrated circuits. II. Optical receiver Analysis,” Journal of Lightwave Technology, Vol. 7, No. 6, pp. 966-971.
- [8] Alok Kushwaha, Manoj Kumar Pandey, Sujata Pandey, and A. K. Gupta, September 2005 , “Analysis of 1/f Noise in Fully Depleted n-channel Double Gate SOI MOSFET,” Journal of Semiconductor Technology and Science, Vol.5, No.3.
- [9] R. S. Fyath, and H. N. Wazeer, 2002, "Performance Analysis of High Electron-Mobility Transistor for Optical Receiver," M. Sc. Thesis, University of Basrah, College of Engineering, Basrah, Iraq.



Figure(1). Receiver sensitivities versus bit-rate for PIN/FET (solid line) and APD/FET (dotted line) direct-detection receivers.



Figure(2). Circuit diagram of a transimpedance optoelectronic integrated circuit (OEIC) optical receiver.



Figure(3). Equivalent circuit of the Amplifier of Figure(2).

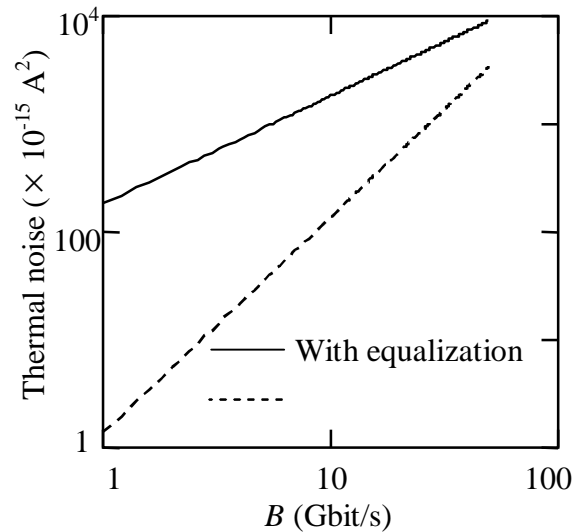


Figure (4a). Variation of thermal noise as a function of B for BER of 10^{-9} .

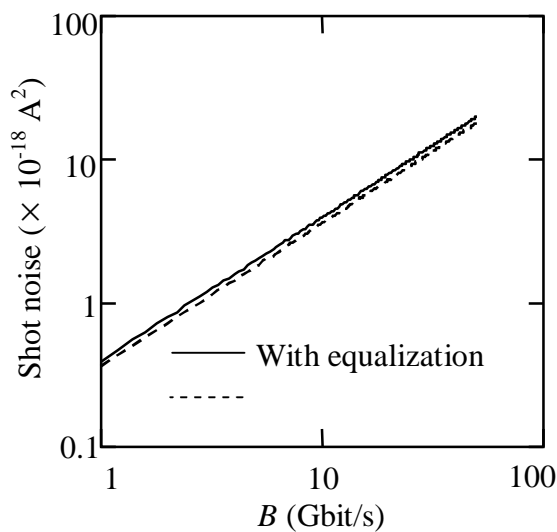


Figure (4b). Variation of Shot noise as a function of B for BER of 10^{-9} .

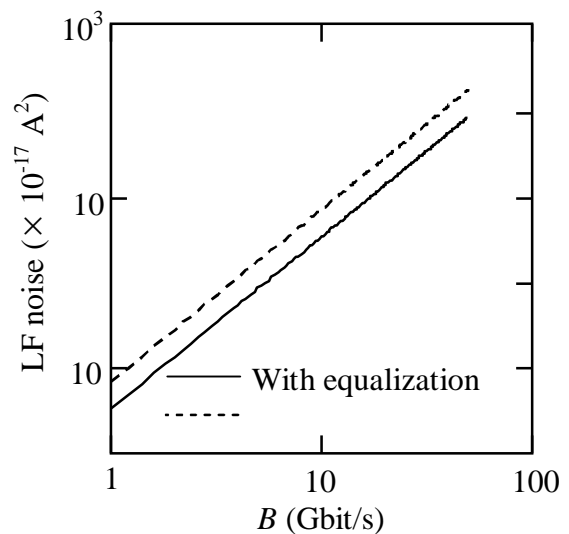


Figure (4c). Variation of LF noise as a function of B for BER of 10^{-9} .

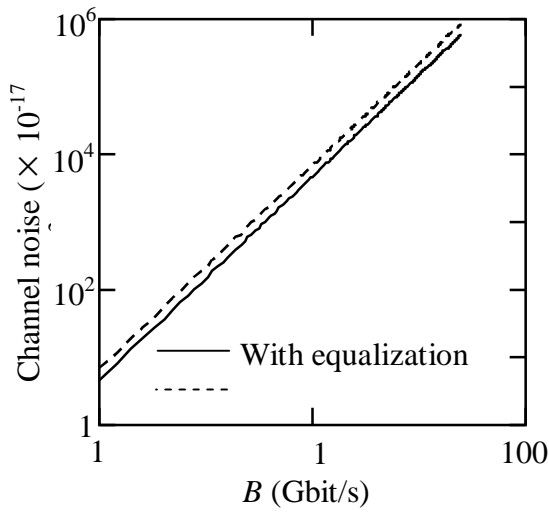


Figure (4d). Variation of Channel noise as a function of B for BER of 10^{-9} .

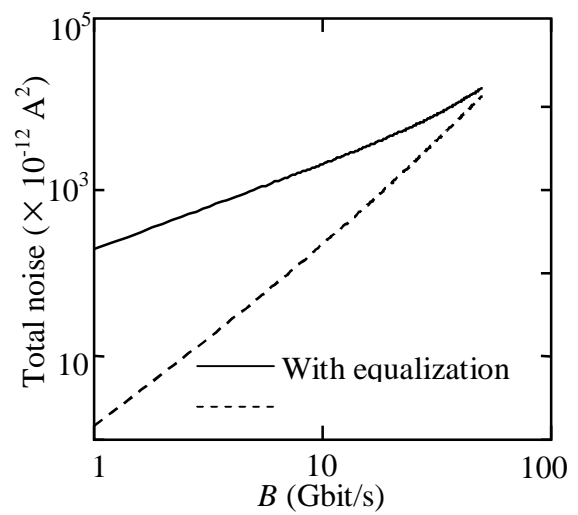


Figure (5). Total noise as a function of bit-rate for BER of 10^{-9} .

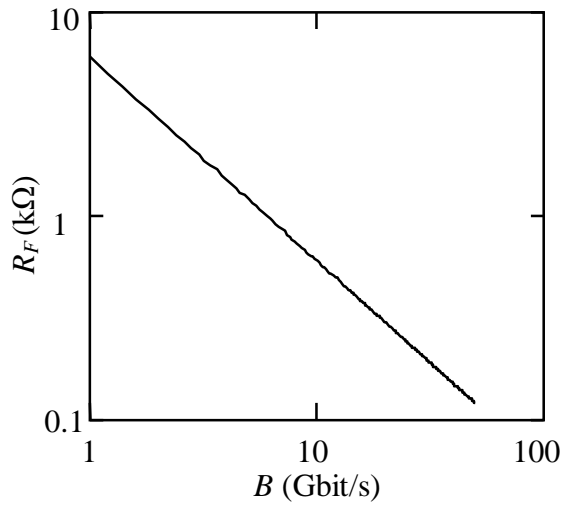


Figure (6). Feedback resistance satisfying the condition of negligible ISI noise as a function of the bit rate.

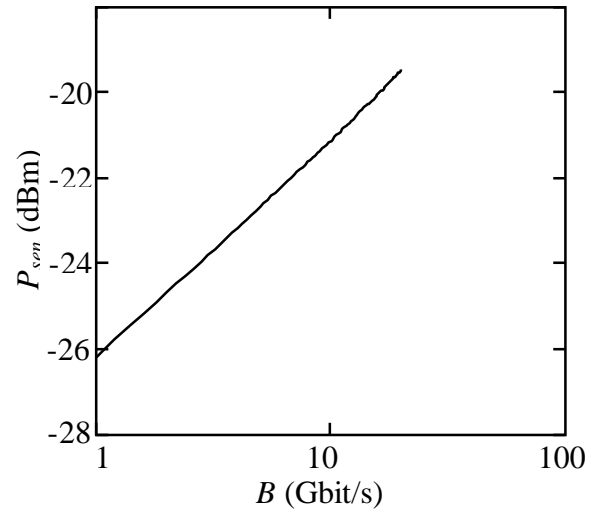
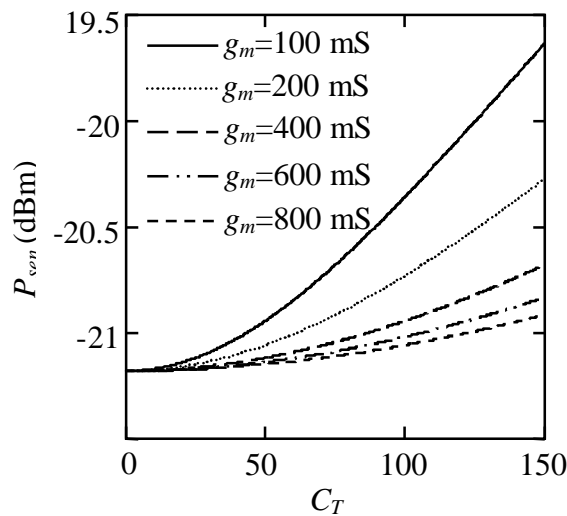


Figure (7). Receiver sensitivity as a function of data bit-rate.



Figure(8). Receiver sensitivity as a function of the total front-end capacitance (C_T) for different values of extrinsic transconductance (g_m).

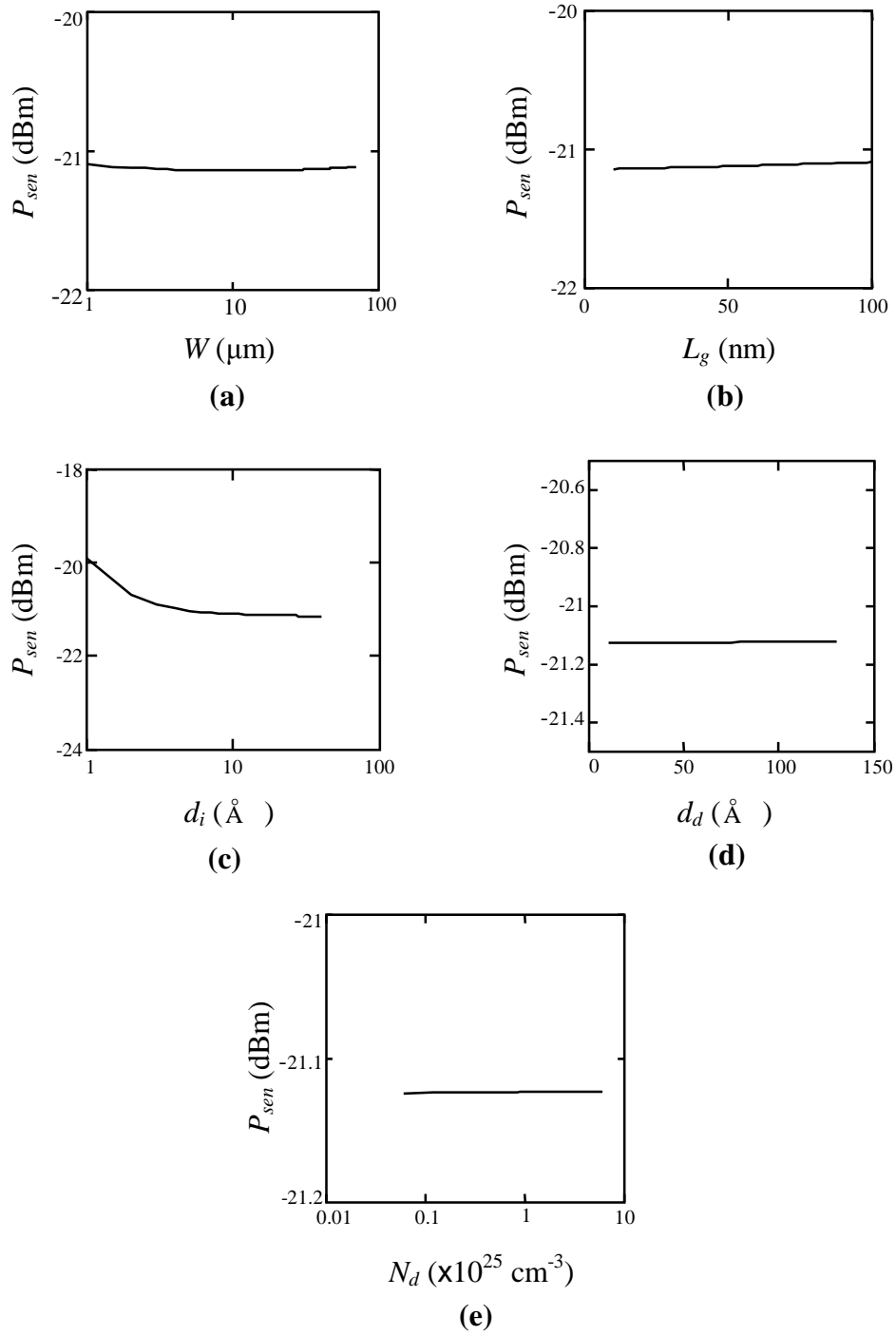


Figure (9). Effect of (a) gate width, (b) gate length, (c) undoped layer thickness, (d) doped layer thickness, and (e) doping concentration on receiver sensitivity.

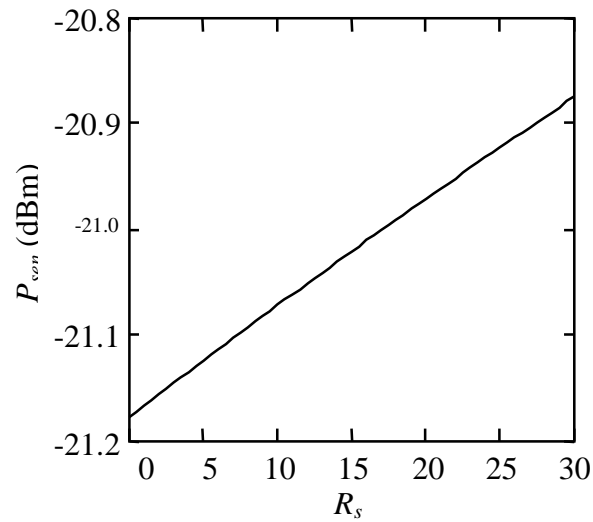


Figure (10). Receiver sensitivity as a function of source resistance.

Table (1). Receiver parameters values used in the simulation.

| Parameter | Value | Unit |
|------------|-------|--------------------|
| Q | 6 | - |
| I_2 | 0.55 | - |
| I_3 | 0.085 | - |
| I_f | 0.12 | - |
| I_{dark} | 2 | nA |
| J_{leak} | 10 | mA/cm ² |
| f_c | 25 | MHz |
| λ | 1.55 | μm |
| Γ | 1.6 | - |
| η | 0.85 | - |
| C_{PD} | 125 | fF |
| C_{st} | 125 | fF |
| B | 10 | Gbit/s |

Table (2). MOSFET parameters used in the simulation.

| Parameter | Value | Unit |
|--------------|--------------------|-------------------------|
| L_g | 50 | nm |
| W | 50 | μm |
| d_i | 20 | \AA |
| d_d | 80 | \AA |
| μ | 12800 | cm^2/Vs |
| v_{sat} | 280×10^7 | Cm/s |
| ϵ_r | 12.1 | — |
| N_d | 6×10^{18} | cm^{-3} |
| V_{off} | -0.017 | V |
| R_s | 1.0 | Ω |
| R_d | 1.0 | Ω |

Table (3). Receiver sensitivity (dBm) as a function of V_{DS} and V_{GS} .

| | $V_{GS}=0.2 \text{ V}$ | $V_{GS}=0.3 \text{ V}$ | $V_{GS}=0.5 \text{ V}$ |
|------------------------|------------------------|------------------------|------------------------|
| $V_{DS}=0.5 \text{ V}$ | -19.1218 | -19.1225 | -19.1231 |
| $V_{DS}=1.0 \text{ V}$ | -19.1219 | -19.1226 | -19.1232 |
| $V_{DS}=1.5 \text{ V}$ | -19.1220 | -19.1227 | -19.1233 |
| $V_{DS}=2.0 \text{ V}$ | -19.1220 | -19.1228 | -19.1234 |

Development of Computer Controlled Oxy Estelline Cutting Machine

Sadiq Muhsin

College of Engineering
Thi Qar University

Salah Mahdi

College of Engineering
Thi Qar University

Haider Jabar

College of Engineering
Thi Qar University

Abstract

Occasionally, the state organizations and many private companies in Thi Qar Governorate request some spare parts that must be manufactured locally because they are unavailable in Iraq .Since these parts have complex shapes, and the Engineering College Workshop's machines are unable to cut them, thus it was necessary to develop the existing Oxy Estelline cutting machine to control its motion by computer.

The main idea of this research is to make the machine cutter movement in two dimensions according to a path drawn by (Autodesk Land Desktop) program which necessitates addition of an electric circuit (Interface) between the machine and the computer to convert the path into two dimensional motions .This requires replacement of some unnecessary parts from the machine by others. The major added parts are:

1. Servo Motors.
2. Controller.
3. Drive.
4. Power Supply.
5. Power Cables.
6. Data Cables.
7. Lead Screws.
8. Brackets.
9. Bases to fix the motors and brackets.

After welding processes of the bases and mounting the motors, brackets, and electric circuits, the machine was tested by fixing a pen instead of the cutter and drawing many graphs such as circle, rose, gear, and gasket on a paper .The drawings are completed successfully and accurately, then the machine was used to cut rose and gasket by the flame .Satisfactory results are obtained .Now, the user can use the machine easily to cut any complex shape.

Keywords: CNC machine tool accuracy; Geometric error; Machining error; Error compensation.

المستخلص

في الكثير من الأحيان تقوم الشركات الحكومية وبعض الشركات الأهلية في محافظة ذي قار بطلب تصنيع بعض قطع الغيار غير المتوفرة في الأسواق المحلية. ولما كانت هذه القطع ذات أشكال معقدة يصعب قطعها داخل ورش الكلية لذا دعت الحاجة إلى تطوير ماكينة قطع بالشعلة الأوكسي إستيلينية الموجودة في داخل الورش وجعل حركتها آلية ومن ثم السيطرة عليها بواسطة الحاسوب.

إن الفكرة الرئيسة للبحث هي جعل أداة القطع في الماكينة تتحرك في بعدين وفقاً لشكل مرسوم بالحاسبة بواسطة برنامج الرسم (Autodesk Land Desktop) وهذا يستلزم وضع مجموعة دوائر الكترونية (Interface) بين الحاسبة وماكينة القطع لتحويل الرسم الموجود في الحاسبة إلى حركات في بعدين. هذا الأمر يتطلب رفع بعض القطع غير الضرورية من الماكينة وإضافة قطع أخرى. ومن أهم القطع التي تمت إضافتها إلى الماكينة هي:

1. ماطورات (Servo Motors)
2. مسيطر (Controller)
3. قائد (Drive)
4. مجهز قدرة (Power Supply)
5. كيبلات قدرة (Power Cables)
6. كيبلات نقل البيانات (Data Cables)
7. براغي (Lead Screws)
8. محامل (Brackets)
9. قواعد تثبيت للماطورات والمحامل

بعد إجراء عمليات اللحام لقواعد التثبيت وتركيب الماطورات والدوائر الالكترونية تم اختبار الماكينة عن طريق تثبيت قلم بدل أداة القطع والرسم على ورق سميك وقد تم بنجاح رسم دائرة ووردة رباعية الاوراق ومسنن وكازكت وكانت الرسوم دقيقة جداً ومطابقة للواقع. بعد ذلك تم استخدام أداة القطع لقطع وردة خماسية الاوراق وكازكت وكانت النتائج مرضية جداً.

1. Introduction

CNC machines are used extensively in industries to reduce costs, improve productivity, obtain better product quality, and avoid humans faults and working in hazardous environments.

Chana Raksiri et al [1] proposes a new off line error compensation model by taking into account the geometric and cutting force induced errors in a 3-axis CNC milling machine . Geometric error estimation determined by back-propagation neural network is proposed and used separately in the geometric error compensation model .Likewise, cutting force induced error estimation by back-propagation neural network determined based on a flat end mill behavior observation is proposed and used separately in the cutting force induced error compensation model .Various experiments over a wide range of cutting conditions are carried out to investigate cutting force and machine error relation .Finally, the combination of

geometric and cutting force induced errors is modeled by the combined back-propagation neural network. This unique model is used to compensate both geometric and cutting force induced errors simultaneously by a single model. Experimental tests have been carried out in order to validate the performance of geometric and cutting force induced errors compensation model.

Tae-Yong Kim et al[2] present the indirect cutting force measurement method in contour NC milling processes by using current signals of servomotors. A Kalman filter disturbance observer and an artificial neural network (ANN) system are suggested. A Kalman filter disturbance observer is implemented by using the dynamic model of the feed drive servo system, and each of the external load torques to the x and y -axis servo motors of a horizontal machining center is estimated. An ANN system is also implemented with a training set of experimental cutting data to measure cutting force indirectly. The input variables of the ANN system are the motor currents and the feed rates of x and y -axis servo motors, and output variable is the cutting force of each axis. A series of experimental works on the circular interpolated contour milling process with the path of a complete circle have been performed. It is concluded that by comparing the Kalman filter disturbance observer and the ANN system with a dynamometer measuring cutting force directly, the ANN system has a better performance.

Mahbubur Rahman[3] presents a theoretical and practical relations which have been established between static and dynamic measuring systems. These relations are important when we are measuring machine tools with different measuring devices to validate the measurement results. The traces obtained by one measuring system have been compared and simulated with the traces obtained by other methods. Several methods for improving the positioning accuracy of machine tools which have been studied. One of the methods is NC code modification. This method has been applied to develop an NC program processor based on the error found by the measurements.

Hui Wang and Qiang Huang[4] use the concept of an Equivalent Fixture Error (EFE) embedded into a modeling methodology to obtain insights into this fundamental phenomenon and to achieve an improved process control. They developed a sequential root-cause identification procedure and EFE compensation methodology. A case study was presented to demonstrate the proposed diagnostic procedure. A simulation study was also performed to illustrate the error compensation procedure.

Abdul –Baki Khalaf [5] performed a 3-axes CNC plasma-cutting machine designed, manufactured and controlled. Mechanical design included material selection, frame design,

guideways design, driving mechanism and bearings mounting .Hardware elimination of errors such as backlash, clearance and squareness are strongly considered in each step of the procedure of mechanical design .Also he develop a new motion controller model called Error Model Reference Adaptive Control(EMRAC) .The model was built in the form of (C++) language .The model has been validated through several tests and proved to have advantages over other standard control techniques.

2. Design and analysis

The cutting machine before development is shown in Figure (1) .From this machine some of the unimportant parts are removed, then all remaining parts are maintained and lubricated.



Figure (1). Cutting machine before development.

Two servo motors with the following specifications are used :

- Stall current continuous 7.2 A

- Voltage 230 V
- Rated speed 5000 RPM
- Rated output power 1.6 kW
- Continuous stall torque 4 N.m
- Peak torque 12.8 N.m

The dimensions of the motors are illustrated in Figure (2).

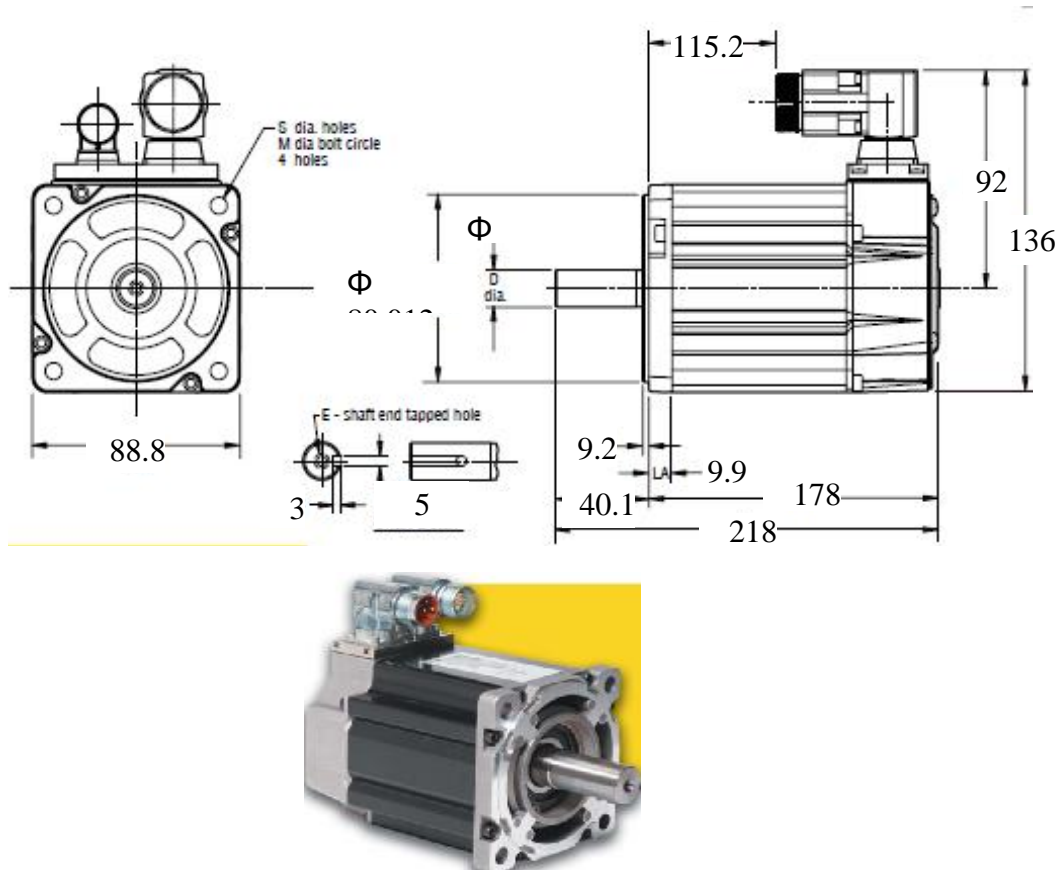


Figure (2) .Dimensions in (mm) of the servo motors.

Two Aries drives are used to control the torque, velocity, and position of servo motors . The drive dimensions are shown in Figure (3).

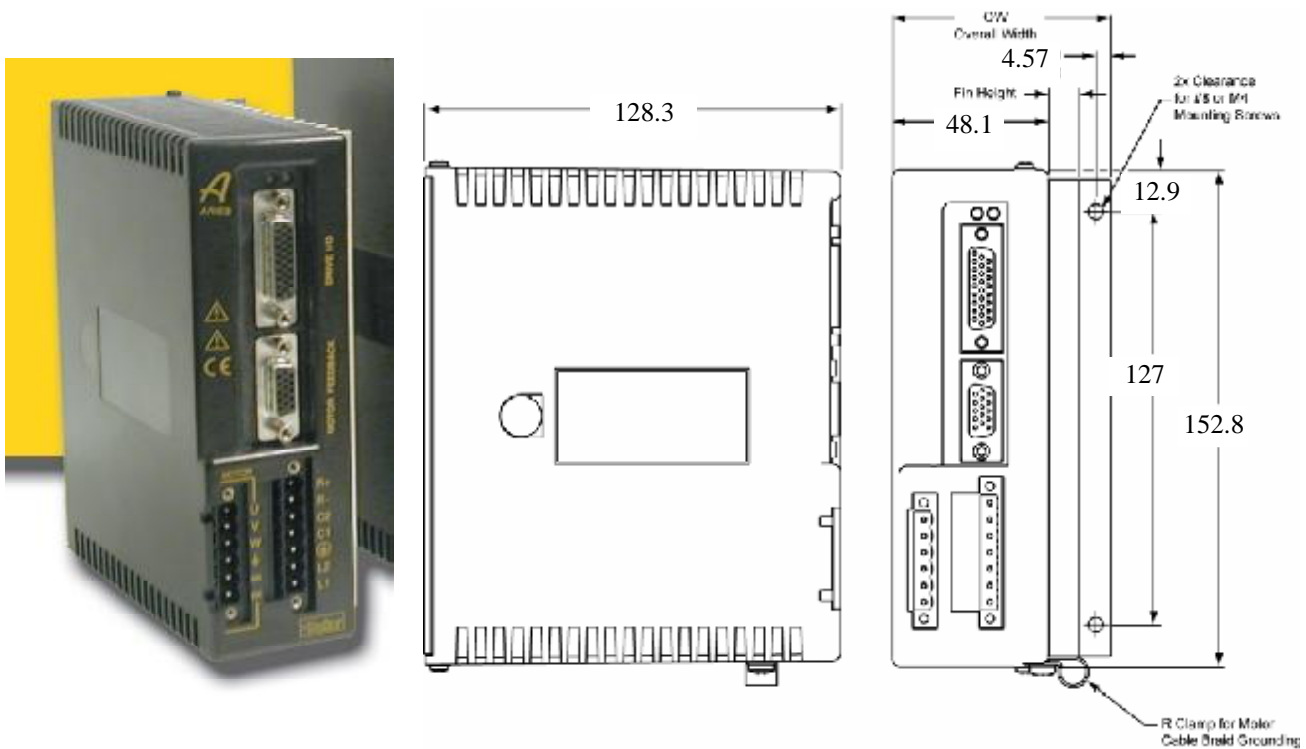


Figure (3).Drive dimensions in (mm).

Among the most important elements of automated manufacturing machines is the controller . The controller provides the facility of proper placement of the cutting tool relative to work piece. The most common controller in industry is the PID (Proportional-Integral-Derivative) controller. Such controllers are widely used in NC and CNC machines. This because of their general applicability to most control systems, and they can be implemented easily either in analog form or in digital form. ACR9000 controller is used to controlling servo drives. There are eight axis connectors on the front panel .They are labeled AXIS0 through AXIS7, the dimensions of the controller are illustrated in Figure (4).

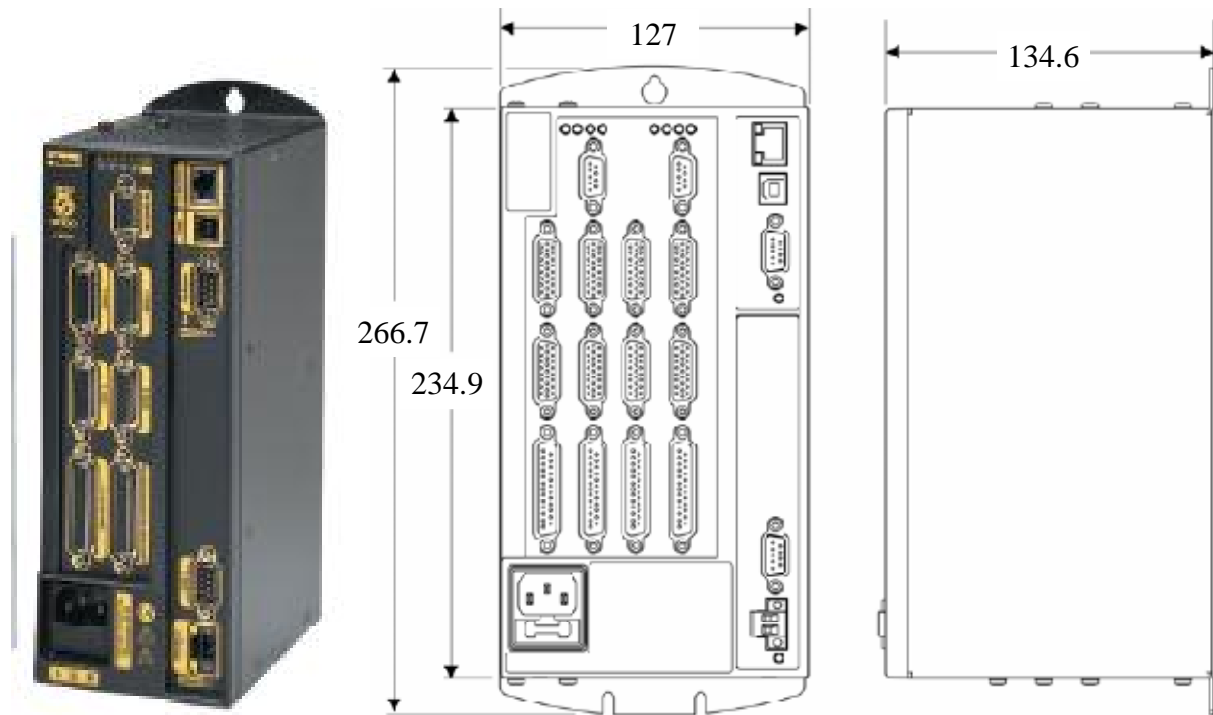


Figure (4). Controller dimensions in(mm).

The motion in two dimensions is transmitted by two lead screws each of them have diameter of (22 mm), pitch of (2.5 mm), and length of (2 m) .Each of the lead screw mounted by two brackets, the brackets and motors are mounted on bases made from cast iron material of dimensions (330×130×10 mm) for motors and (60 ×130 ×10 mm) for brackets as shown in Figure (5).

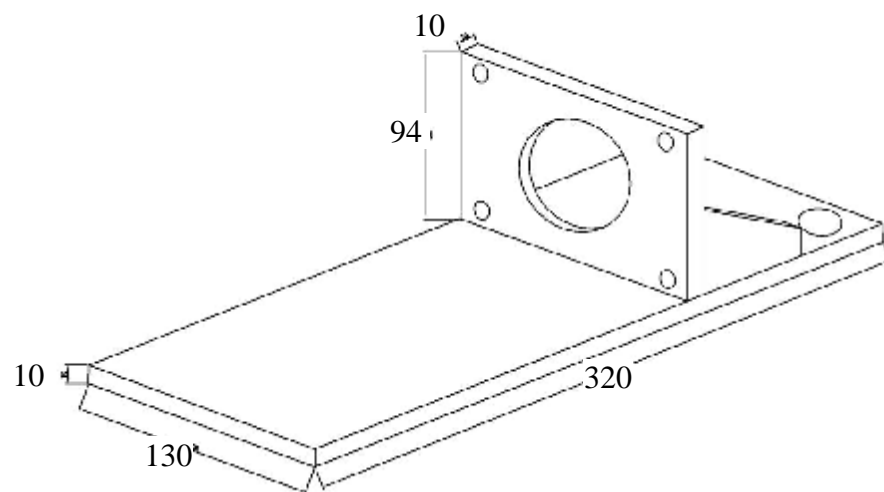


Figure (5) .The base used to support the servo motors.

The motors are connected to the lead screw by a muff coupling as illustrated in Figure (6).



Figure (6). The connection between the motor and the lead screw.

The x-axis guide way consists of lead screw and nut , two brackets are mounted on the lead screw .Each bracket consists of ball bearing assembled inside a cap bracket .All brackets are mounted on bases are welded to the machine body .

The above procedure for installing guide way for x-axis is repeated for y-axis .The cutting machine with all added parts is shown in Figure (7) and Figure (8).

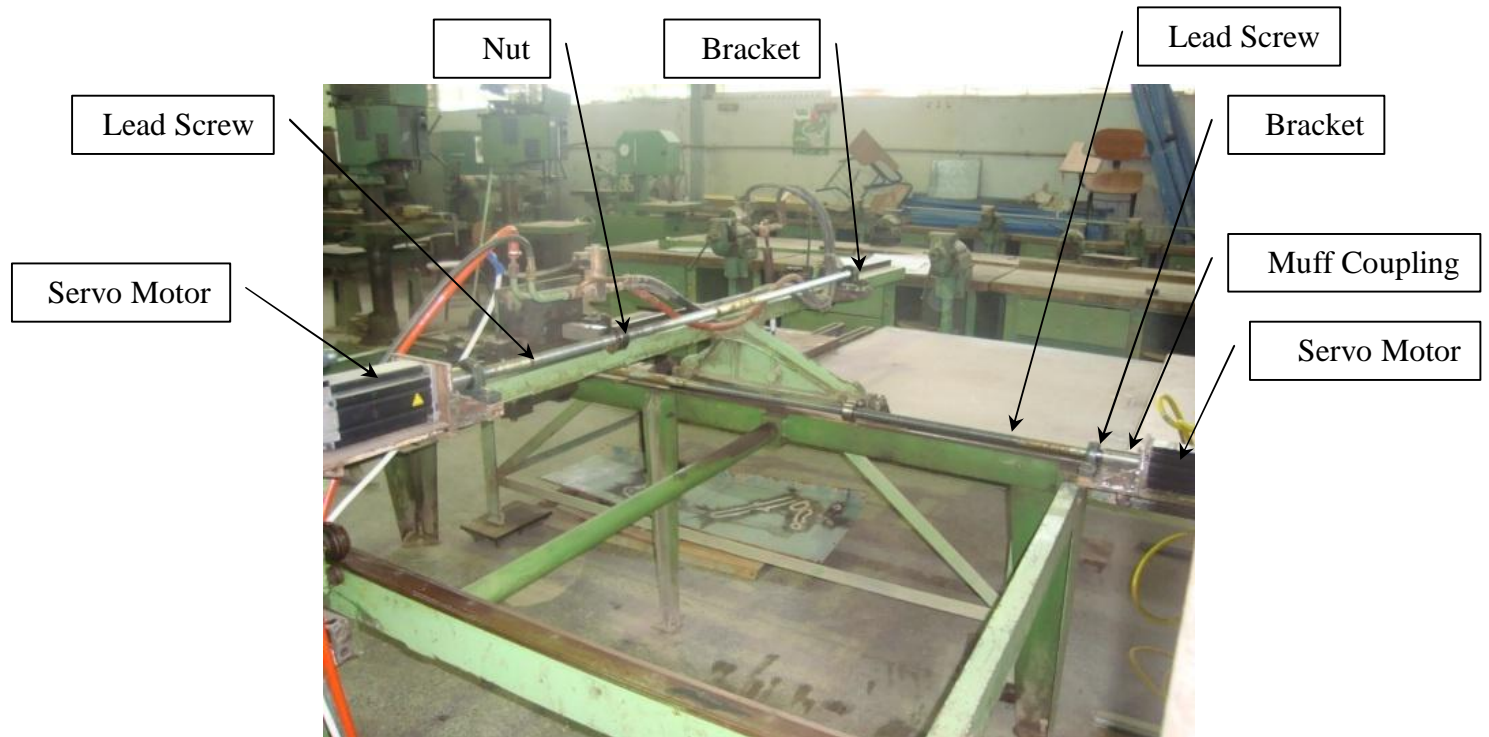


Figure (7). Cutting machine with mechanical added parts.



Figure (8) . Interface circuit for cutting machine.

3. Graphical User Interface (GUI)

A Graphical User Interface (GUI) is a graphical display that contains devices or components, that enable a user to perform interactive tasks. To perform these tasks, the user of the GUI does not have to create a script or type commands at the command line. Often, the user does not have to know the details of the task at hand.

The GUI components can be menus, toolbars, push buttons, radio buttons, list boxes, and sliders—just to name a few. In MATLAB software, a GUI can also display data in a tabular form or as plots, and can group related components.

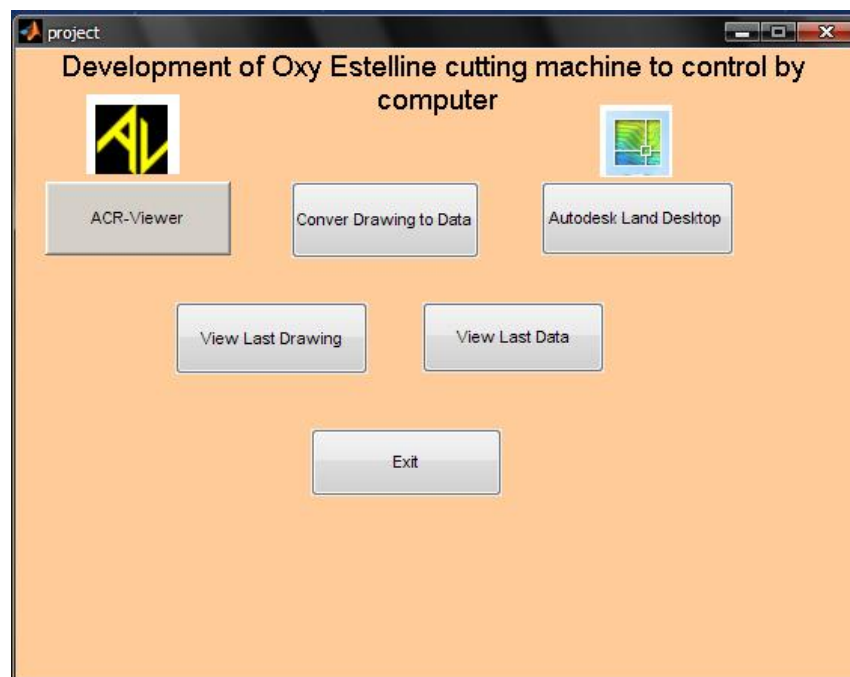


Figure (9) . Graphical User Interface (GUI) menu.

Each component, and the GUI itself, is associated with one or more user-written routines known as callbacks. The execution of each callback is triggered by a particular user action such as a button push, mouse click, selection of a menu item, or the cursor passing over a component.

Using MATLAB 7.6.0(R2008a) creates GUI to connect two programs, namely, Autodesk Land Desktop and ACR -Viewer to easy control the path drawn in Autodesk Land Desktop program and convert this path to data to be exported to ACR -Viewer program to make the motion in two dimensions.

4. Results and discussion

After welding processes of the bases and mounting the motors, brackets, and electric circuits, the machine was tested by fixing a pen instead of the cutter and drawing many graphs such as circle, rose, gear, and gasket on a paper.

- By using Autodesk Land Desktop program the planned tool path shown in Figure (10) for the cutting experiment is drawn.

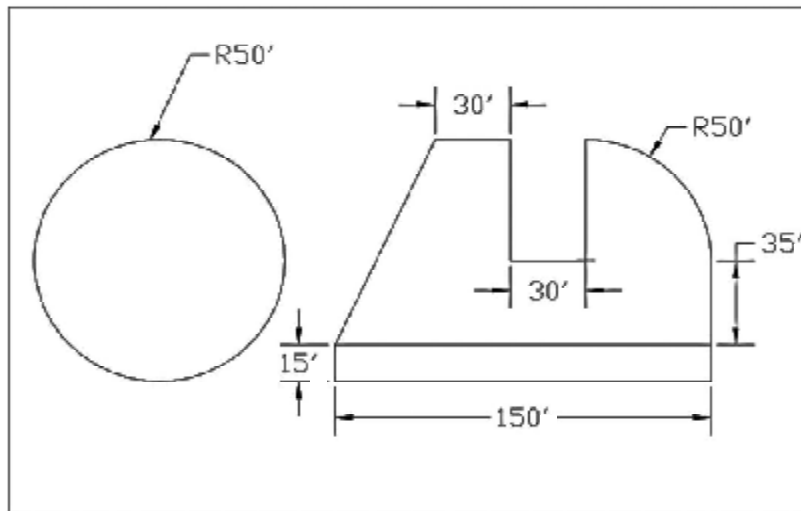


Figure (10) .Planned tool path for the cutting test all dimensions in (mm).

Then by using GUI menu this drawing is converted into data then exported to ACR-Viewer to make the cutter of the machine to move according to this data .The true scale of the drawing by the machine is shown in Figure (16).

- By using the same procedure as above the planned tool path shown in Figure (11) for the cutting experiment is drawn.

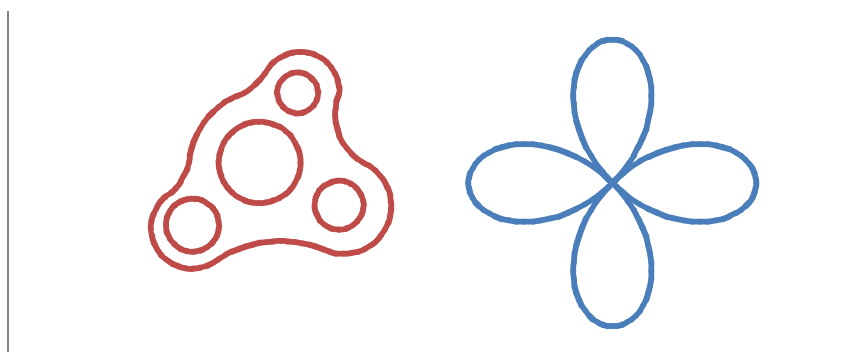


Figure (11). Planned tool path for the cutting test .

Figure (17) shows the true scale drawn by the machine, the dimensions of the true scale are measured. The result was accurate and acceptable. Then the machine was used to cut circle and gasket by the flame as shown in Figures (12) and (13).



Figure (12). Cutting a circle.



Figure (13). Cutting a gasket .

Figure (18) show the true scale for gear drawn by the machine. Figure (14) and figure (15) represents the final shape of the gasket and rose cut by the machine. Now, the user can use the machine easily to cut any complex shape.



Figure (14) . Final shape of gasket that was cut by the machine.



Figure (15). Final shape of rose that was cut by the machine.

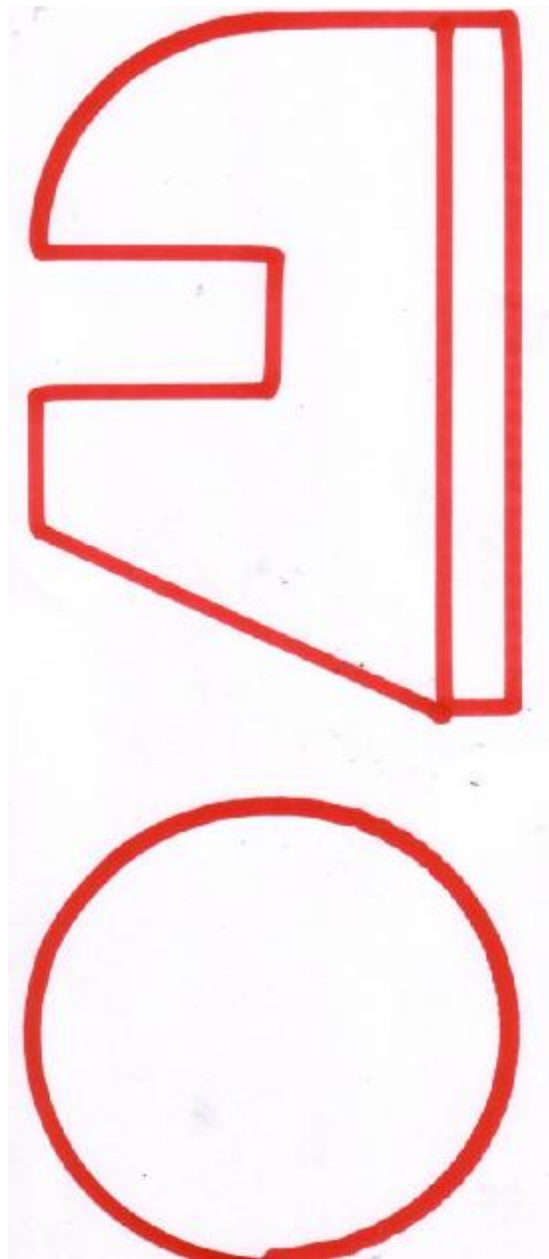


Figure (16). The true scale drawing by the machine.

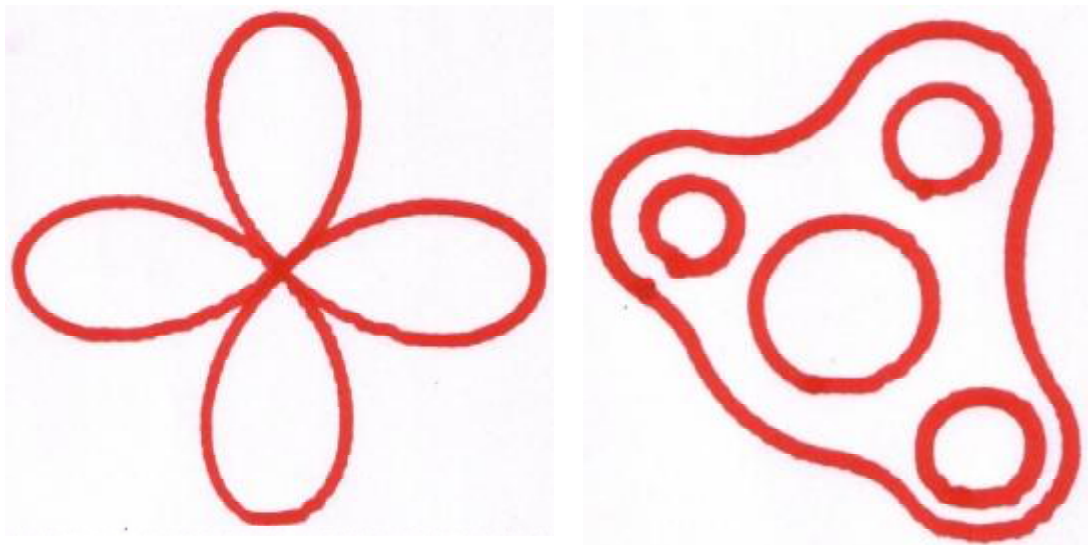


Figure (17) . The true scale of rose and gasket drawn by the machine.

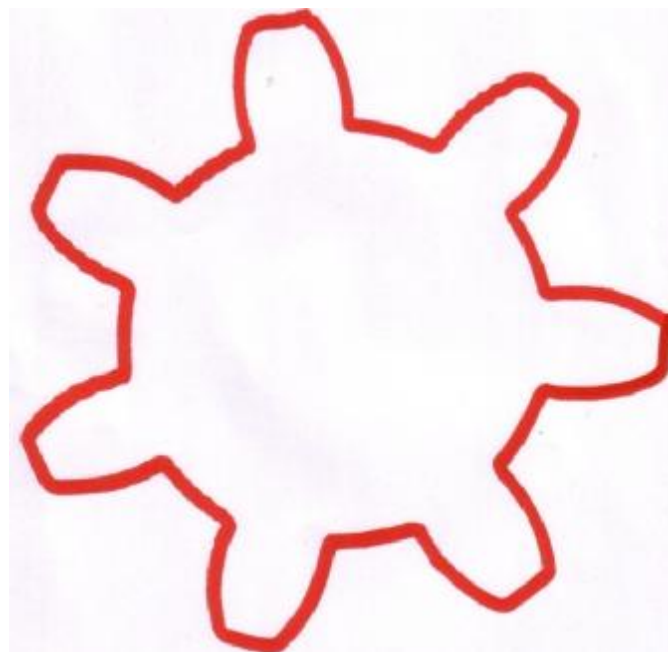


Figure (18) . The true scale of gear drawn by the machine.

5. Conclusions

- PC interface provides powerful control tool for CNC machines. The address and data buses allow for high rate of data transfer between the PC and the machine.
- Servo motors are good motion drives for CNC machines. This is because of their wide range of control of speed.
- User can use the machine easily to cut any complex shape.

ACKNOWLEDGMENTS

This study is supported by the Ministry of Higher Education & Scientific Research\ Research and Development office. Their assistance is highly appreciated.

6. References

- [1] Chana Raksiri, Manukid Parnichkun," Geometric and Force Errors Compensation in A 3-Axis CNC Milling Machine", International Journal of Machine Tools & Manufacture 44 (2004) 1283–1291.
- [2] Tae-Yong Kim, Joongwon Woo, Dongwon Shin, Jongwon Kim," Indirect Cutting Force Measurement in Multi-Axis Simultaneous NC Milling Processes", International Journal of Machine Tools & Manufacture 39 (1999) 1717–1731.
- [3] Mahbubur Rahman," Modeling and Measurement of Multi-Axis Machine Tools to Improve Positioning Accuracy in a Software Way", Ph.D. thesis, University of Oulu, 2004.
- [4] Hui Wang , Qiang Huang, " Error Cancellation Modeling and Its Application to Machining Process Control", IIE Transactions (2006) 38, 379–388.
- [5] Abdul - Baki Khalaf Ali," Design and Construction of a 3-Axes CNC Plasma Cutting Machine with Neural Network Error Compensation", Ph.D. thesis, University of Basrah, 2006.